Theoretical Investigations of High Energy Density Plasmas in Support of KALIF Experiments

J.J. MacFarlane, P. Wang, R.R. Peterson

January 1995

UWFDM-974

FUSION TECHNOLOGY INSTITUTE

UNIVERSITY OF WISCONSIN

MADISON WISCONSIN

Theoretical Investigations of High Energy Density Plasmas in Support of KALIF Experiments

J.J. MacFarlane, P. Wang, R.R. Peterson

Fusion Technology Institute
University of Wisconsin
1500 Engineering Drive
Madison, WI 53706

http://fti.neep.wisc.edu

January 1995

UWFDM-974

Theoretical Investigations of High Energy Density Plasmas in Support of KALIF Experiments

J. J. MacFarlane, P. Wang, and R. R. Peterson

Fusion Technology Institute
University of Wisconsin
1500 Johnson Drive
Madison, WI 53706

January 1995

UWFDM-974

Contents

1. Introduction 1

2. K_α Spectroscopy for Sodium Tracers 4

2.1. Introduction 4

2.2. Models 6

2.3. Proton-Impact Ionization Cross Sections 10

2.4. Na K_α Satellite Emission and Absorption Spectra 10

2.5. Determination of Plasma Conditions From K_α Emission Line Intensity Ratios 20

2.6. Dielectronic Recombination Effects on K_α Satellite Emission Spectra . . . 24

3. Radiation-Hydrodynamics Simulations of KALIF Beam-Plasma Interaction Experiments 32

3.1. Radiation-Hydrodynamics Models 32

3.2. Simulation of B_θ Diode Experiments 34

3.3. Simulation of Applied-B Diode Experiments 44

3.4. Predicted Na K_α Spectra From Radiation-Hydrodynamics Simulations . . . 48

4. Upgrading and Benchmarking of Equation of State and Opacity Calculations 52

4.1. Introduction 52

4.2. Equations of State Modeling and Comparisons 52

4.2.1. Equations of State for Low Density Plasmas 52

4.2.2. Equation of State for High Density Plasmas 56

4.2.3. Hybrid Equation of State Model 59

4.2.4. SESAME Equations of State: Evaluation and Comparison 62

4.3. Opacity Modeling and Comparisons 73

4.3.1. Opacity Calculations for Low-Z Plasmas 76

4.3.2. Opacity Calculations for High-Z Plasmas 95

Appendix A. B_FIT User's Manual A-1

A.1. Introduction A-1

A.2. Defining the Problem A-1

A.3. Input/Output Descriptions A-1

A.3.1. Input A-2

A.3.2. Output A-4

A.4. Subroutines A-4

A.5. Sample Calculation A-6

1. Introduction

The purpose of this report is to provide a detailed description of work performed during the 1994 calendar year in support of KALIF beam-plasma interaction experiments. Our efforts have been concentrated primarily in the areas of spectral diagnostics analyses, atomic physics and radiation transport model development, and radiation-hydrodynamics simulations. This work has been supported by Kernforschungszentrum Karlsruhe (KfK) to develop and apply theoretical and computational models for the study of high energy density plasmas created by KALIF (the Karlsruhe Light Ion Facility). To date, we have developed, tested, and/or upgraded a series of codes which can be used in the analysis of intense ion beam-plasma interaction experiments. These include:

NLTERT – Non-LTE radiative transfer code [1] for spectral analysis of laboratory plasmas. Utilizes a collisional-radiative equilibrium (CRE) model which includes ion beam-impact ionization effects for analyzing K_α spectra.

ATBASE – Suite of atomic structure and collisional cross section codes [2]. Atomic structure calculations utilize a configuration interaction (CI) model with Hartree-Fock wavefunctions. Supplies data for NLTERT and EOSOPA.

EOSOPA – Equation of state and opacity code [3] used to set up tables for radiation-hydrodynamics codes. Utilizes a detailed configuration accounting (DCA) model at low densities and a muffin tin model at high densities. An unresolved transition array (UTA) model is used for high-Z opacities.

BUCKY-1 – Radiation-hydrodynamics code [4] to simulate ICF-related plasmas. It represents an integration of the PHD-IV target physics code [5], the CONRAD target chamber code [6], and the NLTERT CRE line radiation transport code.

SCFMT – Self-consistent field muffin tin model for calculating ion beam stopping powers [7] and high-density equations of state [8].

BFIT – Zeeman line-splitting code [9] for the analysis of spectral line shapes in the presence of strong magnetic fields.

In addition, we have coupled our non-LTE radiative transfer model [10] into KATACO [11] (the Karlsruhe target radiation-hydrodynamics code) in order to provide a more comprehensive treatment of line radiation transport effects in simulations of high energy density plasma experiments.

Table 1.1 shows the list of tasks for our 1994 contract with KfK. The first task was to perform CRE and atomic physics calculations in support of upcoming KALIF beam-plasma interaction experiments. Both emission and absorption K_α satellite spectra were computed for Na tracers to complement previous results for Al, O, and F tracers [12-16]. In addition, we investigated the sensitivity of the intensity ratios of various He-like and Li-like K_α emission lines to the target plasma temperature and density. Also, we have briefly examined the effect of dielectronic recombination on K_α emission spectra. Results for the K_α spectral calculations are discussed in Section 2.

We have also performed radiation-hydrodynamic simulations for KALIF beam-target interaction experiments. This was done using the Wisconsin BUCKY-1 code, which is currently being upgraded with partial support from the U.S. Department of Energy. By comparing results with those of KATACO, we can assess the sensitivity of the predicted target plasma conditions to various physics models. This work is described in Section 3.

The second task was to benchmark our equation of state (EOS) and opacity codes against experimental data and other codes. Comparisons with other codes were made while attending the Third International Opacity Workshop at Garching, FRG in March 1994. Our efforts in this area led to a number of improvements in modeling high-Z opacities and high-density equations of state. Additional comparisons were made with opacities calculated by scientists from Minsk. In addition, our calculated EOS and opacity data were tested in radiation-hydrodynamic simulations of radiation-driven target experiments at Lawrence Livermore National Laboratory. The opacity and EOS work is discussed in Section 4.

Finally, a user's guide for the BFIT Zeeman line-splitting analysis code is supplied in Appendix A.

Table 1.1. Tasks for 1994

1. Perform collisional-radiative equilibrium (CRE) and atomic physics calculations in support of KALIF beam-plasma interaction experiments:

   (a) Predict K_α emission and absorption spectral characteristics for tracer (diagnostic) materials to be used in KALIF experiments.

   (b) Perform calculations to set up atomic physics data bases and identify K_α lines observed in KALIF experiments.

   (c) Using temperature and density distributions obtained from KfK radiation-hydrodynamics simulations, compute synthetic time-dependent and time-integrated spectra for KALIF experiments.

   (d) Perform line ratio analysis to provide additional constraints for temperature and density determinations in KALIF experiments.

   (e) Assess effects of dielectronic recombination on K_α satellite emission spectra.

2. Benchmark equation of state and opacity codes for plasma conditions relevant to KALIF experiments:

   (a) Benchmark opacity calculations against other available codes and experimental data.

   (b) Compare calculated equations of state with other calculated and experimental data.

3. Document results in final report to KfK. Supply KfK with updated CRE and ATBASE codes.

2. K_α Spectroscopy for Sodium Tracers

2.1. Introduction

The present plan for KALIF beam-plasma interaction experiments calls for targets of the type shown in Fig. 2.1. Here, an intense proton beam — generated using either the B_θ diode or applied-B diode — irradiates a "plastic sandwich" target in which thin plastic layers with thicknesses $\sim 0.1 - 0.2\,\mu$m surround a "tracer" mixture of sodium (Na), fluorine (F), and aluminum (Al). The tracer layer provides diagnostic information about the target plasma conditions. This region is roughly uniform (spatially) in density and temperature as the target is heated and expands because: (1) the largest density gradients tend to be restricted to the outer regions of the target (i.e., the CH tampers), and (2) the heating by the beam ions should be approximately uniform because the tracer thicknesses ($\sim 0.1 - 1\,\mu$m) are typically less than the stopping ranges of the ions ($R \sim 15\,\mu$m for 1 MeV protons in Al [17]). Thus, the temperature and density indicated from the K_α spectra of each of the tracer components (F, Na, Al) should be the same if they are well-mixed.

An alternative target concept is to separate the tracer materials into distinct regions, as shown in Fig. 2.2. The use of multiple tracer species of similar atomic number again allows the K_α spectra to be simultaneously measured by the same spectrograph, but in this case the Na and Al tracer regions may actually be at different temperatures. This is because the stopping powers of the materials are somewhat different, as are their equations of state and radiative properties. Thus, one cannot expect in this case that the temperatures deduced from the K_α spectra of each tracer species to be exactly the same. There may be advantages to using targets with separate tracers in future experiments, however, if one were interested in measuring the temperature at different locations within a more complex target, or perhaps in experiments to measure basic physics processes such as radiation energy flow in planar targets [18].

In previous investigations, we have reported on calculations for the K_α satellite spectra of Al [12-14], O [15], and F [16]. It was shown that measuring the K_α satellite spectra — either in emission or absorption — can provide a good determination of the target plasma conditions. Here, we focus in particular on the K_α emission and absorption spectra of Na, which will be one of the tracers in the initial series of KALIF beam-plasma interaction experiments for target heating. In this section we present results for the proton-impact ionization cross sections for Na, list the strongest He-like and Li-like K_α lines which can be expected to be observed, and show several examples of the temperature and density sensitivity of the Na K_α satellite spectra for both emission and absorption. We also present

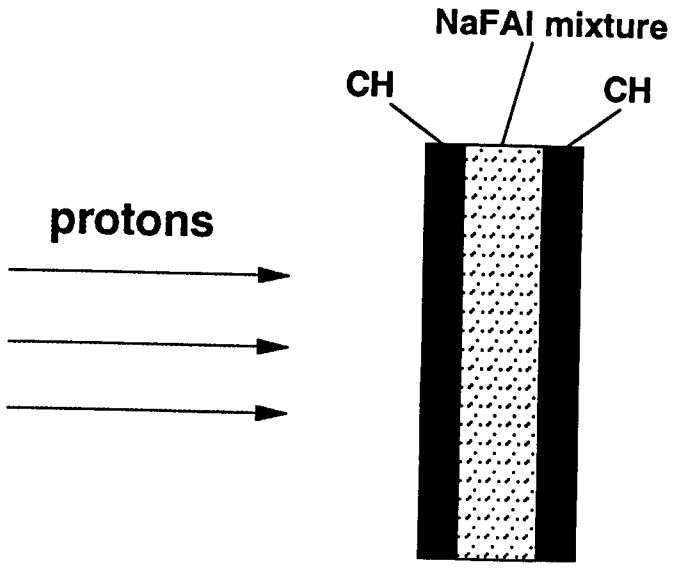

Figure 2.1. Plastic sandwich target with mixed F/Na/Al tracer.

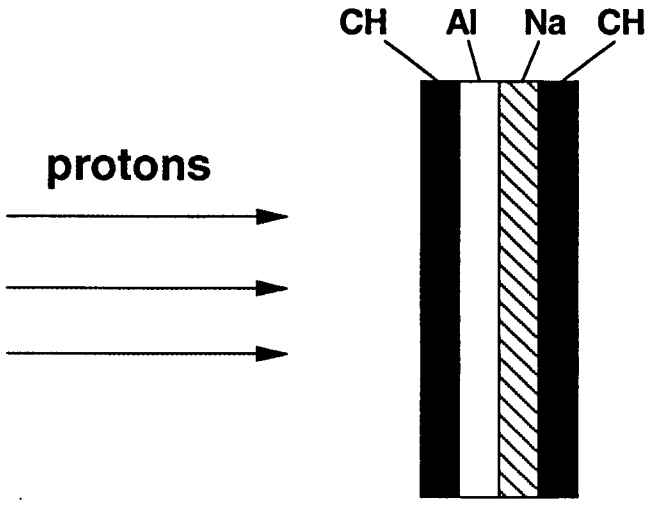

Figure 2.2. Plastic sandwich target with separate Na and Al tracers.

some results describing how the intensity ratios of He-like and Li-like K_α emission lines of Na and Al can be used to diagnose the target plasma temperature and density.

2.2. Models

The models used in the calculations have been documented in detail elsewhere [12-16, 19, 20]. Here, we provide only a brief summary.

Emission and absorption spectra are computed using a collisional-radiative equilibrium (CRE) code whose major features are listed in Table 2.1. Because we are interested in analyzing inner-shell (specifically K_α) spectra, autoionizing states — i.e., atomic levels with K-shell vacancies — are included explicitly in our CRE calculations. The states are populated by ion beam-impact ionization. K_α line radiation is emitted as 2p electrons drop down to fill 1s vacancies created by the beam. Because the K_α lines can be optically thick, even for tracers of thickness $\Delta L \sim 0.1 - 1\,\mu$m, radiation transport effects are included in the computed spectra.

Atomic data for the CRE calculations are computed using the ATBASE [2] suite of codes. The major features of this package are listed in Table 2.2. Ion impact ionization cross sections are computed using a modified plane-wave Born approximation model, with corrections for Coulomb deflection, relativistic effects, and the change in electron binding energy due to the interaction of the target ion and projectile ion [21]. Calculated cross sections using this model have been found to be in good agreement with experimental data (see also Section 2.3). Atomic level energies, oscillator strengths, fluorescence yields, and photoionization cross sections are all based on atomic structure calculations with Hartree-Fock wavefunctions.

In our K_α spectral calculations for Na, a total of more than 500 fine structure levels distributed over all ionization stages were considered. Just over half of these are autoionizing levels. Collisional coupling is complete for He-like through B-like Na; i.e., collisional excitation and deexcitation for both allowed and forbidden transitions is considered. This includes transitions between autoionizing levels as well.

A list of the strongest K_α lines for He-like and Li-like Na are listed in Table 2.3. Also shown are the experimental values and identification symbols of Boiko et al. [22]. Note that the calculated wavelengths are typically within several mÅ of the experimental values. Experimental measurements of intensity ratios of He-like to Li-like lines provide good diagnostic information for targets irradiated by intense light ion beams (see Section 2.5).

Table 2.1. Major Features of Collisional-Radiative Equilibrium Code

- Multilevel, steady-state atomic rate equations are solved self-consistently with the radiation field and ion beam properties.
- Any state in the atomic model can be coupled to any other state; thus, transitions between excited states of differing ions can be considered, as can transitions between non-adjacent ions.
- Ion beam-induced multiple ionization effects are included as direct transitions in the statistical equilibrium matrix equations.
- Emission and absorption spectra include contributions from bound-bound (lines), bound-free (recombinations), and free-free transitions (Bremsstrahlung).
- Inner-shell line emission induced by intense ion beams is calculated by tracking the populating and depopulating rates of autoionizing levels which are explicitly included in the model.
- Line shapes include effects of natural, Doppler, Auger, and Stark broadening.
- Radiation transport is modeled using either:

  (i) an angle- and frequency-averaged escape probability method, or

  (ii) a multiangle, multifrequency model based on the second-order form of the transfer equation.

Table 2.2. Major Features of Atomic Physics Models

- Atomic structure and radiative data are computed using a configuration interaction (CI) model with Hartree-Fock wavefunctions.
- Multiconfiguration Hartree-Fock and Dirac-Fock calculations provide accurate transition energies and oscillator strengths for lines of interest.
- Atomic collisional data are computed using a combination of distorted wave, Coulomb-Born, and semiclassical impact parameter models.
- Ion-impact ionization cross sections are computed using a plane-wave Born approximation model with Hartree-Fock wavefunctions, and with the inclusion of binding energy, Coulomb-deflection, and relativistic corrections.
- Multiple ionization cross sections are computed using an independent event model with a binomial distribution probability.
- Term-dependent Auger rates and fluorescence yields are calculated using an LS coupling formalism with Hartree-Fock wavefunctions.

Table 2.3. Strongest He- and Li-like K_α Transitions for Sodium

		This calculation	Exp. Data	
Lower Level	Upper Level	Wavelength (Å)	Wavelength (Å)	Identification
$1s^2$ $^1S)$ $^1S_{0.0}$	$1s^1\ 2p^1$ $^2S)$ $^3P_{1.0}$	11.084	11.088	He[IC]
$1s^2$ $^1S)$ $^1S_{0.0}$	$1s^1\ 2p^1$ $^2S)$ $1P_{1.0}$	11.004	11.004	He_α
$1s^2\ 2p^1$ $^1S)$ $^2P_{0.5}$	$1s^1\ 2p^2$ $^2S)$ $^2S_{0.5}$	11.068	—	n
$1s^2\ 2p^1$ $^1S)$ $^2P_{1.5}$	$1s^1\ 2p^2$ $^2S)$ $^2S_{0.5}$	11.071		m
$1s^2\ 2s^1$ $^1S)$ $^2S_{0.5}$	$1s^1\ 2s^1\ 2p^1$ $^3S)$ $^2P_{0.5}$	11.088	11.088	t
$1s^2\ 2s^1$ $^1S)$ $^2S_{0.5}$	$1s^1\ 2s^1\ 2p^1$ $^3S)$ $^2P_{1.5}$	11.087		s
$1s^2\ 2s^1$ $^1S)$ $^2S_{0.5}$	$1s^1\ 2s^1\ 2p^1$ $^1S)$ $^2P_{0.5}$	11.157	11.155	r
$1s^2\ 2s^1$ $^1S)$ $^2S_{0.5}$	$1s^1\ 2s^1\ 2p^1$ $^1S)$ $^2P_{1.5}$	11.155		q
$1s^2\ 2p^1$ $^1S)$ $^2P_{0.5}$	$1s^1\ 2p^2$ $^2S)$ $^2P_{0.5}$	11.170	—	d
$1s^2\ 2p^1$ $^1S)$ $^2P_{0.5}$	$1s^1\ 2p^2$ $^2S)$ $^2P_{1.5}$	11.167		b
$1s^2\ 2p^1$ $^1S)$ $^2P_{1.5}$	$1s^1\ 2p^2$ $^2S)$ $^2P_{0.5}$	11.173		c
$1s^2\ 2p^1$ $^1S)$ $^2P_{1.5}$	$1s^1\ 2p^2$ $^2S)$ $^2P_{1.5}$	11.170		a
$1s^2\ 2p^1$ $^1S)$ $^2P_{0.5}$	$1s^1\ 2p^2$ $^2S)$ $^2D_{1.5}$	11.189		k
$1s^2\ 2p^1$ $^1S)$ $^2P_{1.5}$	$1s^1\ 2p^2$ $^2S)$ $^2D_{2.5}$	11.192	11.202	j

2.3. Proton-Impact Ionization Cross Sections

The ion-impact ionization cross sections are calculated using a CPSSR [23] method, which is a modified approach to the plane-wave Born approximation (PWBA). The conventional plane-wave Born approximation model can provide good results for ion-impact ionization cross sections if the velocity of the incident particle v_1 is larger than the orbital velocity v_i of ionizing electron. However, for slow collisions, i.e., $v_1 \lesssim v_i$, the PWBA method usually overestimates cross sections significantly because it neglects the effects of the charged projectile on the target's atomic states, and the influence of internuclear repulsion. The CPSSR method incorporates the binding and Coulomb-deflection effects in the PWBA model and produces much better results for ion-impact ionization cross sections over a wide range of projectile energy. A comparison of the calculated cross sections of PWBA and CPSSR with the experimental data [24] for Al K-shell ionization by α particles is shown in Fig. 2.3. Hartree-Fock wavefunctions were used in our calculations. It is clear that including binding and Coulomb deflection effects at low projectile energies leads to a significant improvement in the calculated cross sections.

Figures 2.4 and 2.5 show ion impact ionization cross sections for protons on aluminum and sodium. Also shown are the experimental data of aluminum K-shell ionization cross sections [25]. We believe that calculated cross sections for other subshells of aluminum and sodium should be of similar accuracy. Note that the outer shell ionization cross sections are several orders of magnitude larger than that of the K-shell. In proton beam-target interaction experiments, the outer shell ionizations have the major contribution to the target heating, while K-shell ionization provides diagnostic information.

2.4. Na K_α Satellite Emission and Absorption Spectra

K_α satellite emission and absorption spectra were computed for Na over a range of temperatures and densities relevant to the upcoming KALIF beam-plasma interaction experiments with the B_θ diode. The purpose of the calculations is to provide some general insight as to which satellites can be expected to be observed, and their relative strengths. In each case the plasma temperature and density were assumed to be spatially uniform. The plasma thickness corresponded to a Na tracer with a solid density thickness of 5000 Å. The beam was taken to be a monoenergetic proton beam of $E_B = 1.0$ MeV with a power density of 0.3 TW/cm^2. (Note that the power density in the standalone CRE calculations affects the absolute intensities of the K_α emission lines, but not their relative strengths.) In each case, we assumed an instrumental spectral resolution of $E/\Delta E = 1500$.

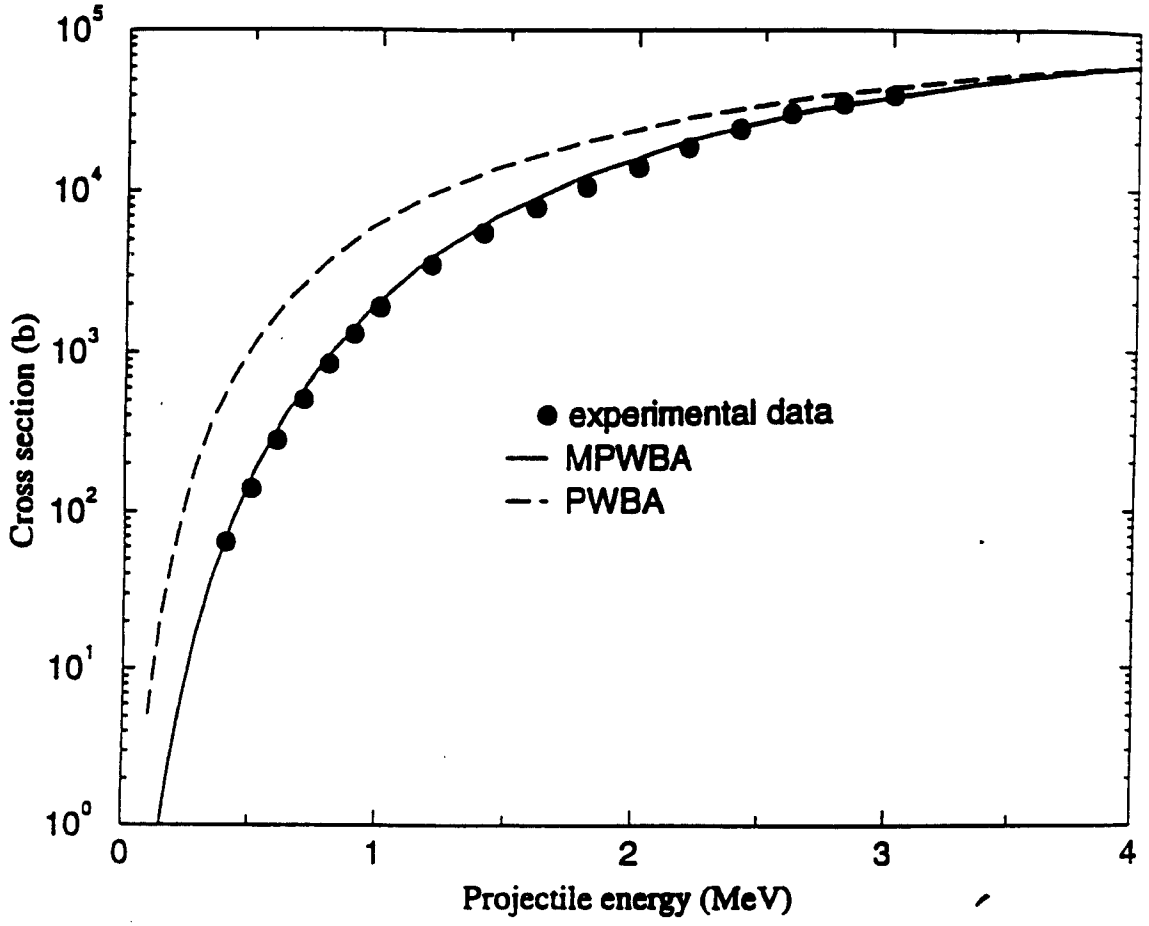

Figure 2.3. Al K-shell ionization cross sections by He^{+2} bombardment. A comparison of PWBA and CPSSR results with experimental data.

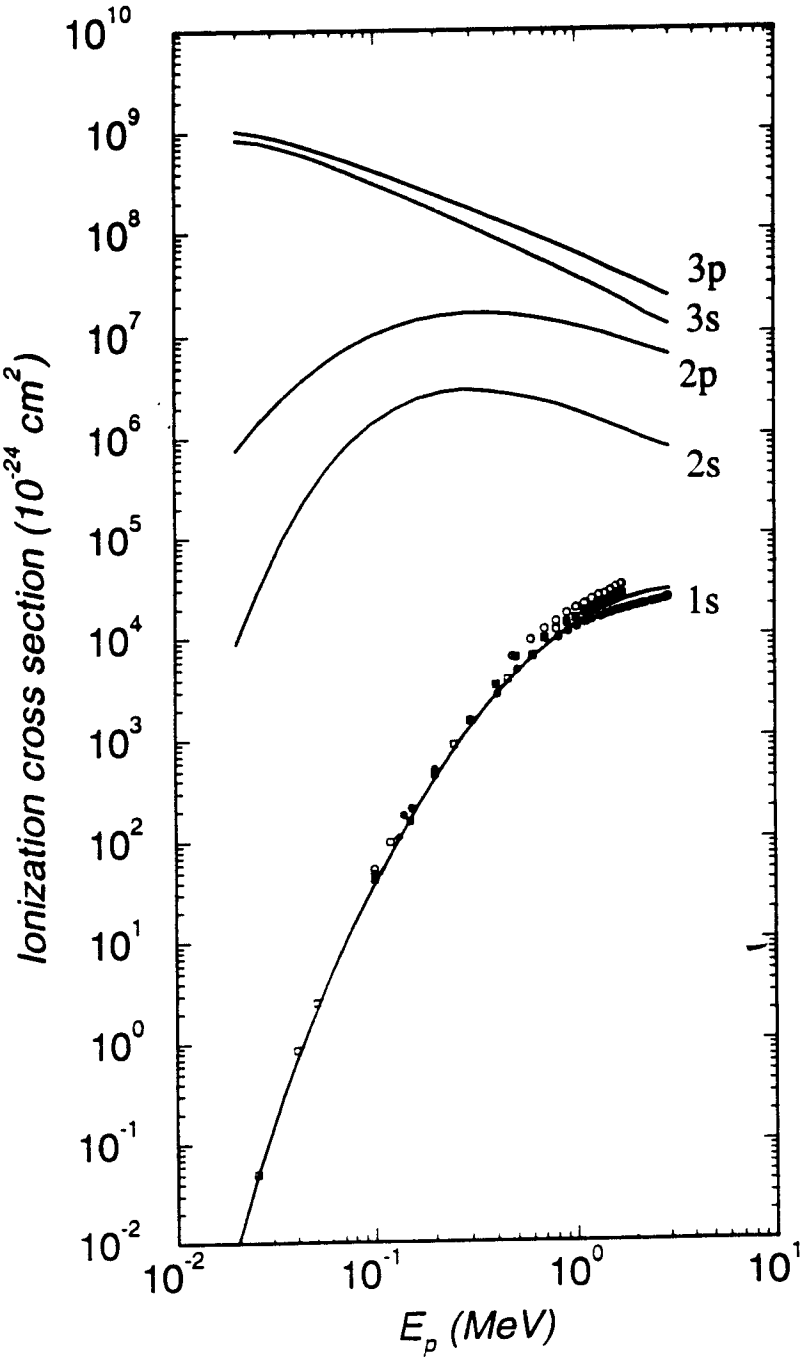

Figure 2.4. Al subshell ionization cross sections by proton bombardment.

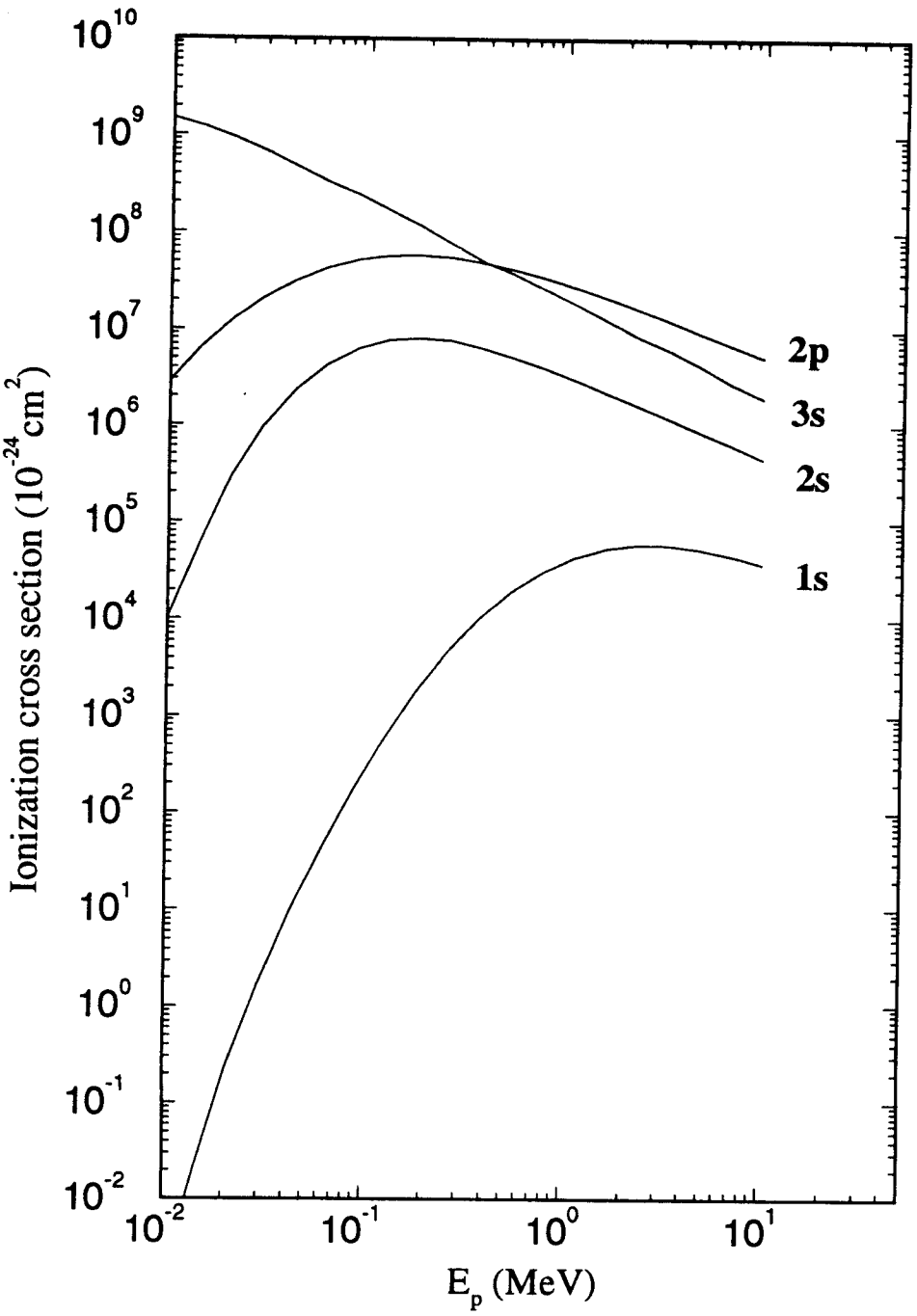

Figure 2.5. Na subshell ionization cross sections by proton bombardment.

Table 2.4. Na K_α and K_β Wavelengths

Ion	K_α Wavelength (Å)	K_β Wavelength (Å)
He-like	11.00	9.43
Li-like	11.10-11.25	9.6-9.8
Be-like	11.25-11.35	9.8-10.1
B-like	11.40-11.50	10.1-10.3
C-like	11.50-11.65	10.4-10.6
N-like	11.65-11.75	10.7-10.9
O-like	11.75-11.85	11.0-11.1
F-like	11.9	11.2-11.3
Ne-like	11.9	11.5

Figures 2.6 through 2.9 show Na K_α satellite emission and absorption spectra for densities ranging from 10^{19} to 10^{21} ions/cm^3 and temperature ranging from 15 to 35 eV. Table 2.4 lists the wavelengths of the various K_α and K_β lines for each ion. It is worth mentioning several points which were noted in our earlier studies of Al, O, and F tracers. First, K_β lines can be readily observed in absorption but are very weak in emission. This is easily understood by the following example. K_β absorption for a Be-like ion can result from a $1s^22s^2 \rightarrow 1s^12s^23p^1$ transition, and the absorption is proportional to the population of the $1s^22s^2$ state (which is the ground state configuration). On the other hand, K_β emission for a Be-like satellite is produced by reactions of the type $1s^22s^23p^1 \stackrel{\text{p-impact}}{\rightarrow} 1s^12s^23p^1 \stackrel{h\nu}{\rightarrow} 1s^22s^2$, where the first transition is due to proton-impact ionization, and the second emits the K_β photon. Thus, K_β emission is proportional to the population of excited states that have partially-filled 3p subshells, which for Na lie about 160 eV above the ground state.

Secondly, both the emission and absorption spectra are seen to exhibit very good temperature sensitivity. This can be seen more clearly in Fig. 2.10, which shows the K_α emission spectrum for Na at temperatures of 15, 20, 25, and 30 eV. Note the distinct shift in ionization over each temperature increment. A time-resolved emission measurement should be able to allow for a temperature determination to an accuracy of just a few eV.

Third, note the significant increase in intensity of the He_α line ($\lambda = 11.004$ Å) relative to the colder satellites. This occurs because the $1s^12p^1$ states are unable to Auger decay to lower ionization states. By comparison, autoionization states of the lower ionization stages typically depopulate via radiationless Auger transitions more than 95% of the time.

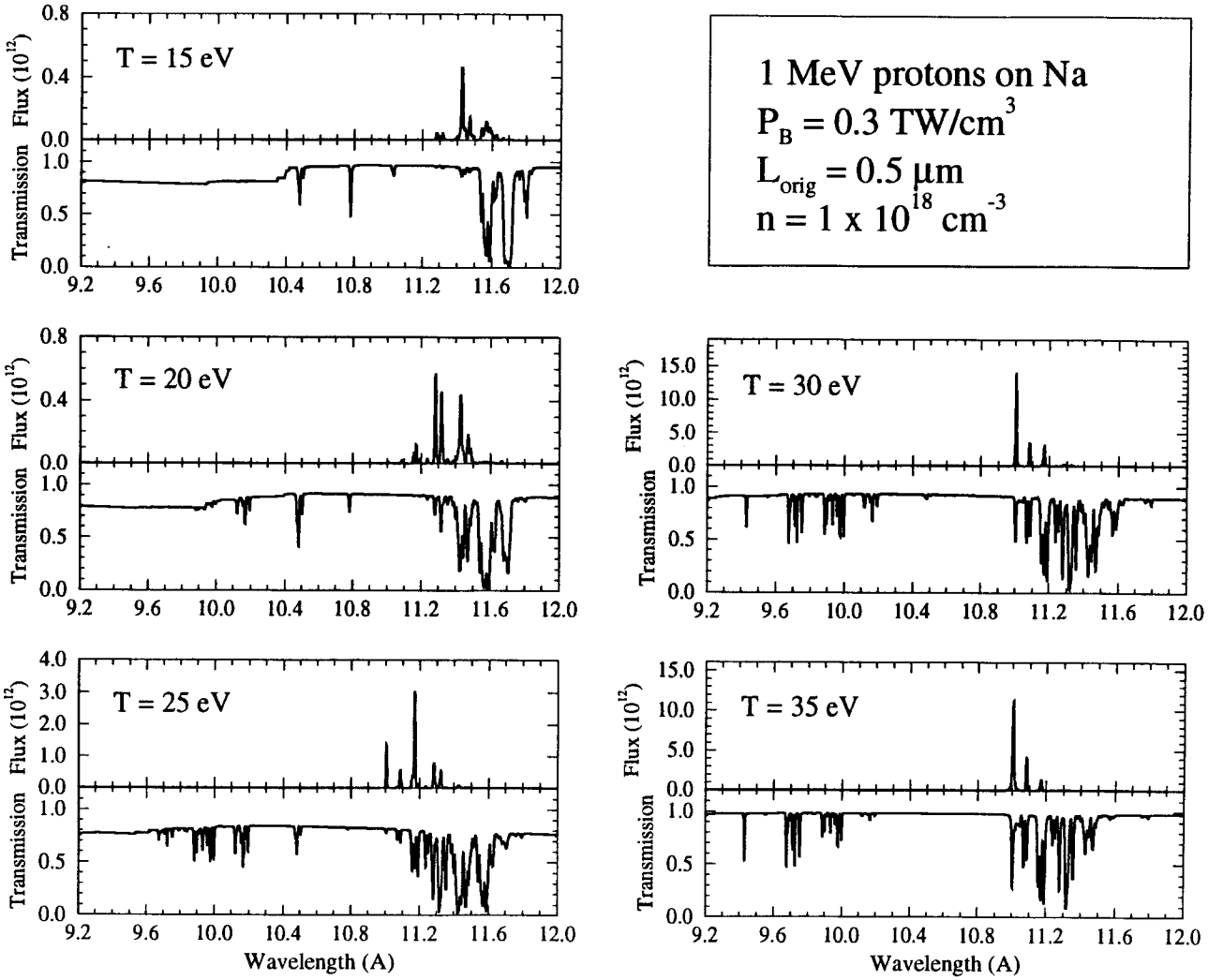

Figure 2.6. Temperature-dependence of K_α emission and absorption spectra for Na tracer with a density of $n = 10^{18}$ ions/cm^3 and an original thickness of 5000 Å.

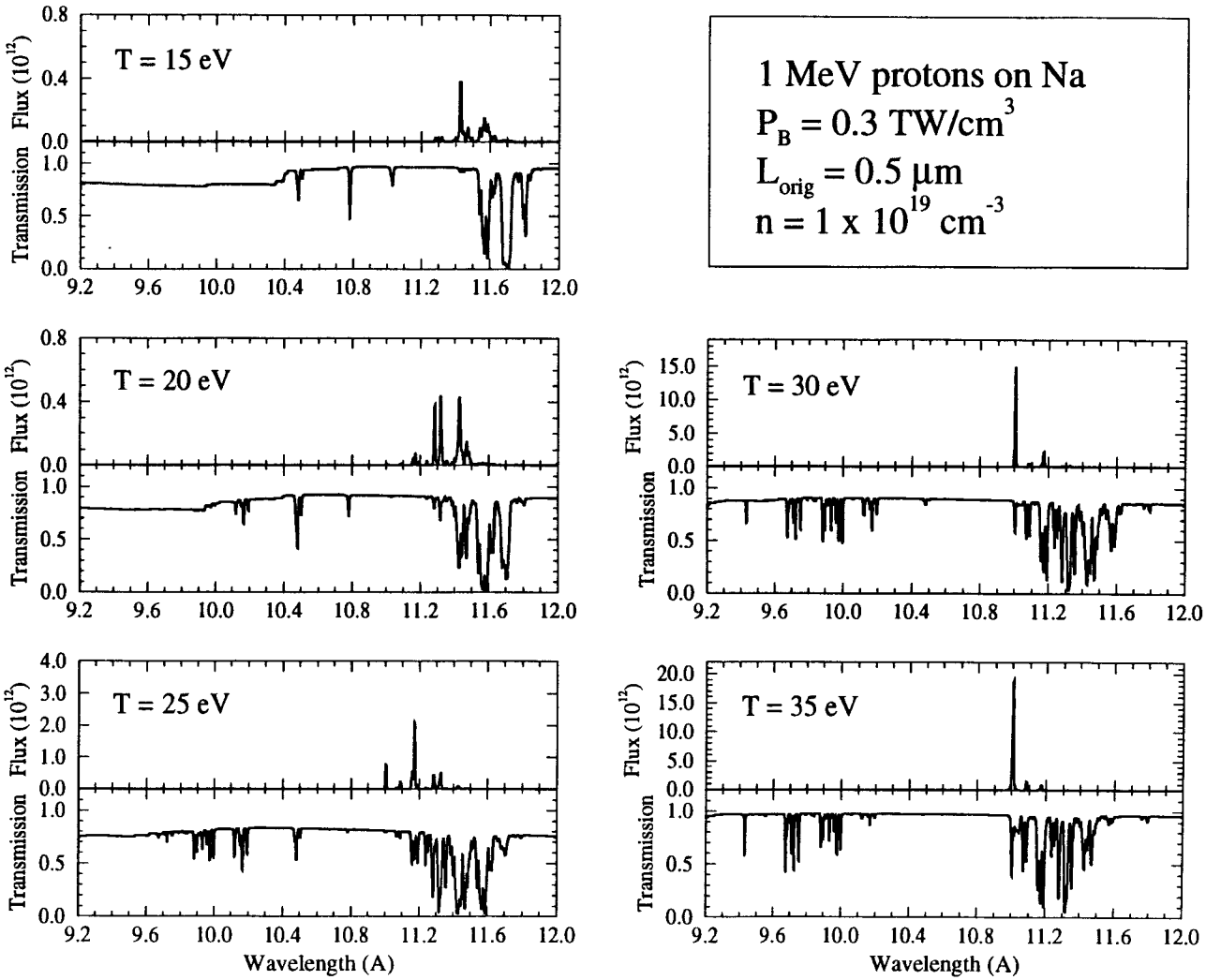

Figure 2.7. Temperature-dependence of K_α emission and absorption spectra for Na tracer with a density of $n = 10^{19}$ ions/cm^3 and an original thickness of 5000 Å.

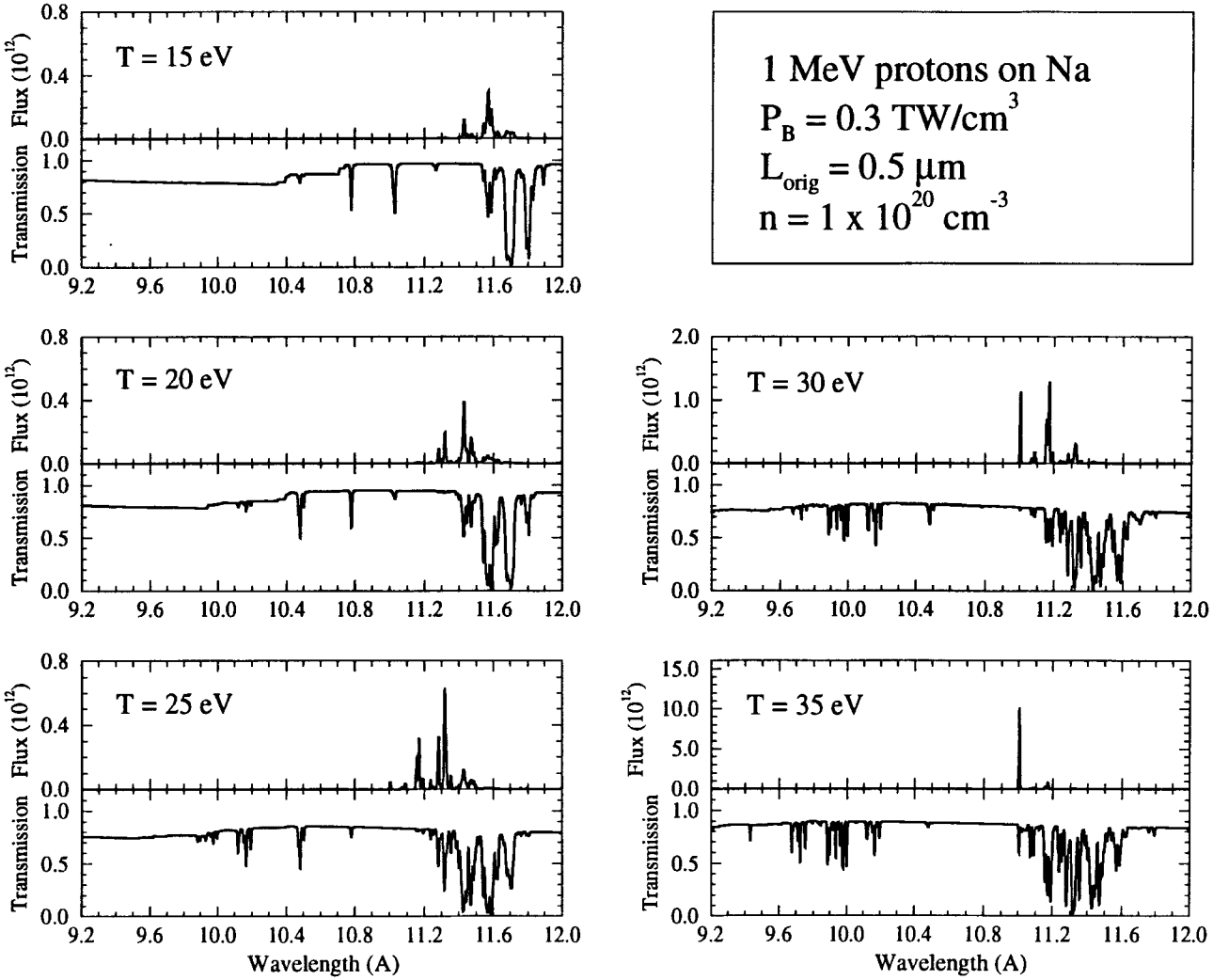

Figure 2.8. Temperature-dependence of K_α emission and absorption spectra for Na tracer with a density of $n = 10^{20}$ ions/cm^3 and an original thickness of 5000 Å.

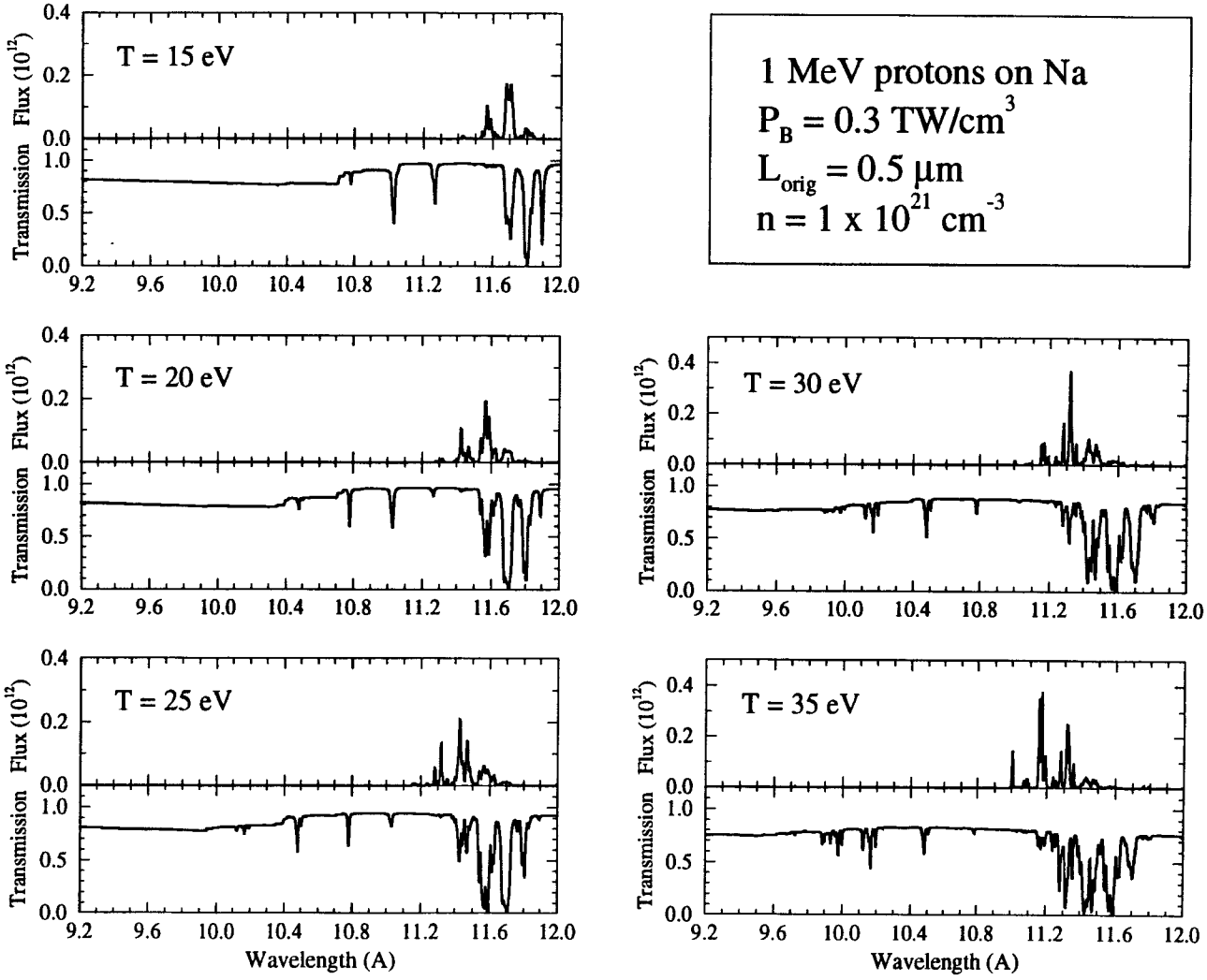

Figure 2.9. Temperature-dependence of K_α emission and absorption spectra for Na tracer with a density of $n = 10^{21}$ ions/cm^3 and an original thickness of 5000 Å.

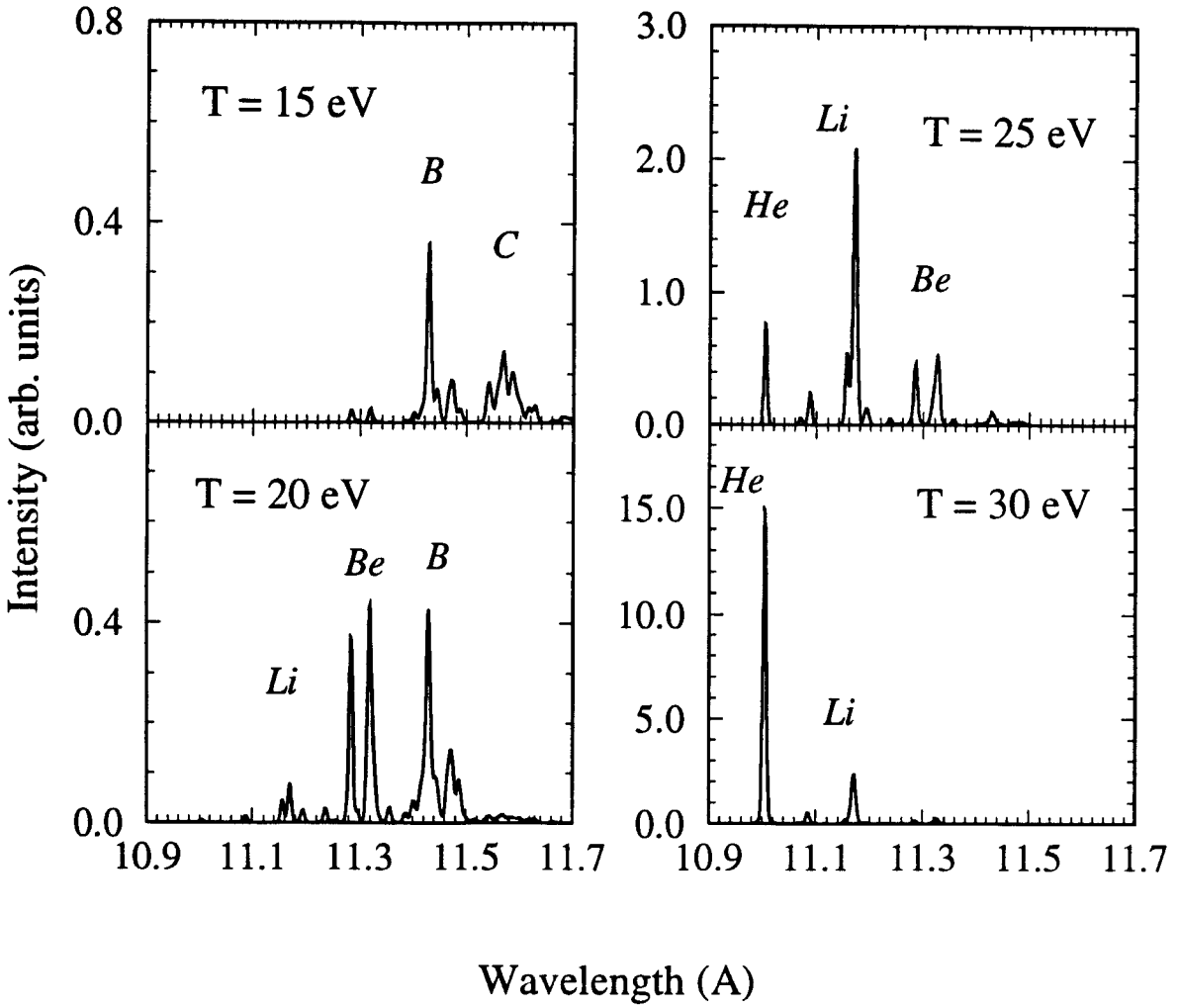

Figure 2.10. Na K_α emission spectra calculated for $n = 10^{19}$ ions/cm^3 and an original tracer thickness of 5000 Å. Note the strong dependence on temperature and the significantly higher line intensities for the He- and Li-like satellites at $T \gtrsim 25$ eV.

2.5. Determination of Plasma Conditions From K_α Emission Line Intensity Ratios

With sufficiently good spectral resolution ($\lambda/\Delta\lambda \gtrsim 1000$) one should be able to experimentally measure the intensities of individual lines or small groups of lines. This is particularly true for relatively high ionization stages (e.g., He-like to Be-like) because there are fewer K-shell lines with which to overlap. Thus, if tracers can be chosen such that one gets significant emission from the He_α and Li-like satellite lines, the measured intensity ratios of various pairs of lines can be used to determine the plasma temperature and density.

Figure 2.11 shows examples of good line ratio diagnostics for Na. The top 2 plots indicate that the Li(st)/He_α and Li(abcd)/He_α ratios should be good temperature diagnostics in the $T \approx$ 20-35 eV range (see Table 2.3 for a definition of transitions). For instance, a measured intensity ratio of 1.0 for Li(st)/He_α would indicate a plasma temperature of about 23-25 eV. Note that this prediction depends only very weakly on the density in the $10^{18} - 10^{20}$ ions/cm^3 range. An example of a potentially good density diagnostic is shown at the bottom of Fig. 2.11. In this case the intensity of the Be-like ($\lambda_2 - \lambda_4 \equiv 11.300\,\mathring{A} < \lambda < 11.340\,\mathring{A}$) wavelength region relative to the Be-like ($\lambda_1 \equiv 11.264 < \lambda < 11.300$) wavelength region is plotted as a function of ion density for isotherms of 20, 25, 30, and 35 eV. A "perfect" density diagnostic is one in which the intensity ratio depended sensitively on the density, but was independent of the temperature. Although some temperature-dependence is apparent in this plot, it is felt that a measurement of this wavelength regime could provide a useful independent check on the density.

Similar intensity ratio plots for Al are shown in Figs. 2.12 and 2.13. Several potential temperature indicators can be found from the intensities of several of Li-like Al satellites to the He_α line (Fig. 2.12). Good density diagnostics tend to be found to be using the intensity ratios of lines of the same ionization stage (Fig. 2.13). Note that the He/Li ratios for Al provide good temperature diagnostic information in the $T \approx$ 40-60 eV range, whereas the same ratios for Na work best in the $T \approx$ 20-35 eV range. Thus, it may be that the Na tracer will provide the best diagnostic information in the B_θ diode experiments, while the Al tracer could provide the best constraints for the applied-B diode experiments.

To summarize, it is felt that spectral measurements of emission and/or absorption K_α satellite spectra can be used effectively to determine target plasma conditions in intense light ion beam experiments. We also note that good spectral resolution ($\lambda/\Delta\lambda \gtrsim 1000$) is important for diagnosing target plasma conditions, and generally speaking, even greater

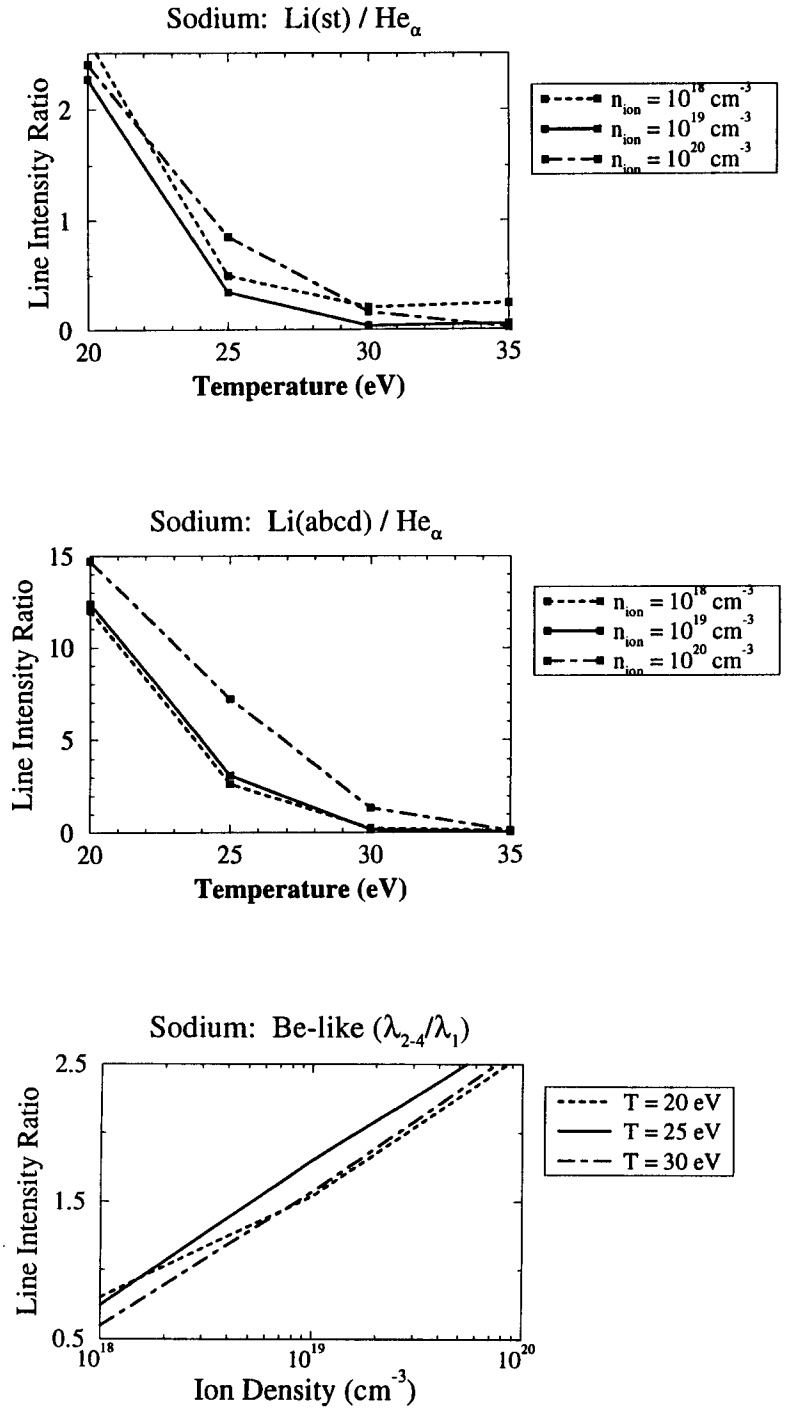

Figure 2.11. Temperature- and density-sensitive K_α emission line intensity ratios for Na.

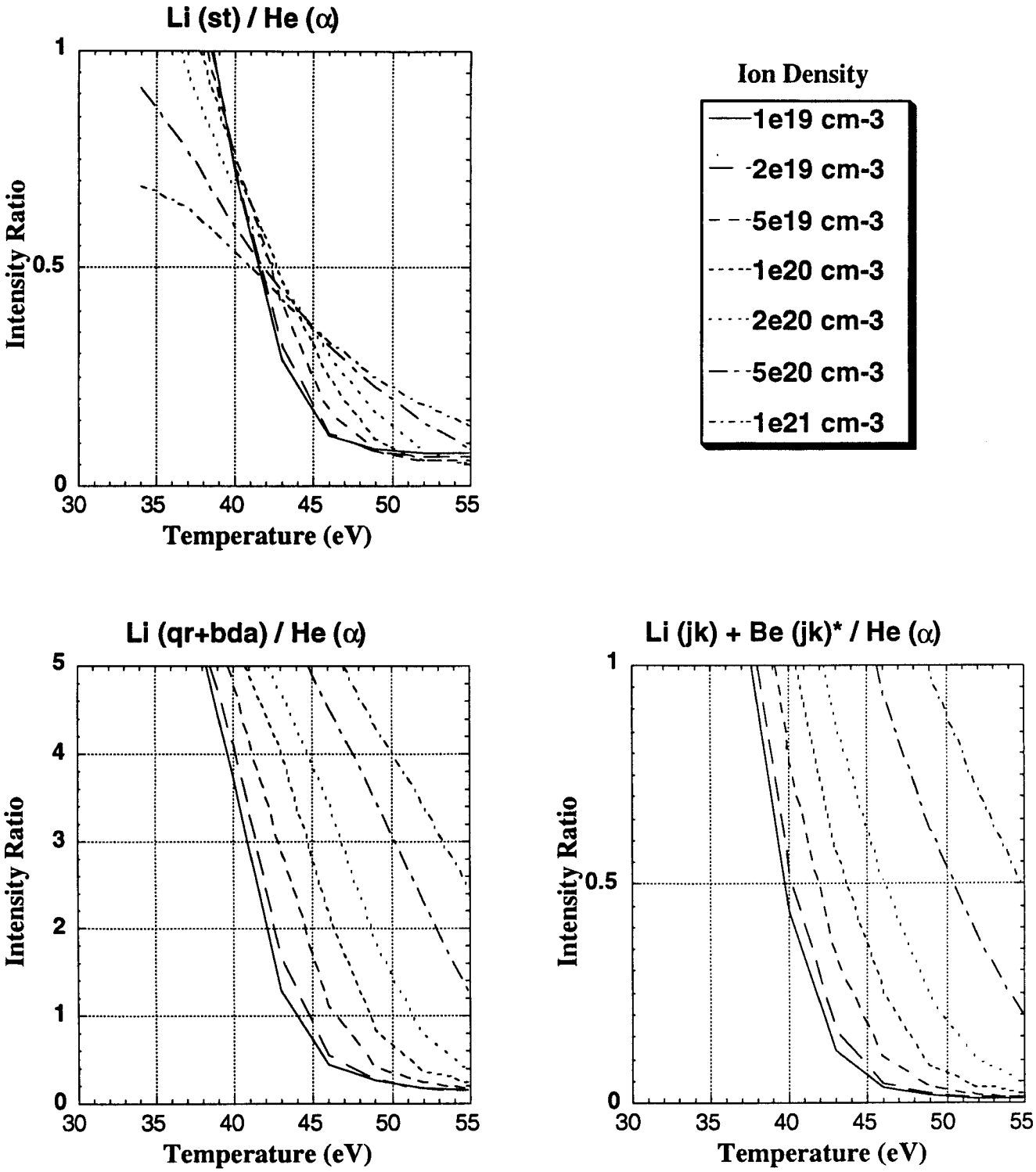

Figure 2.12. Temperature-sensitive K_α emission line intensity ratios for Al.

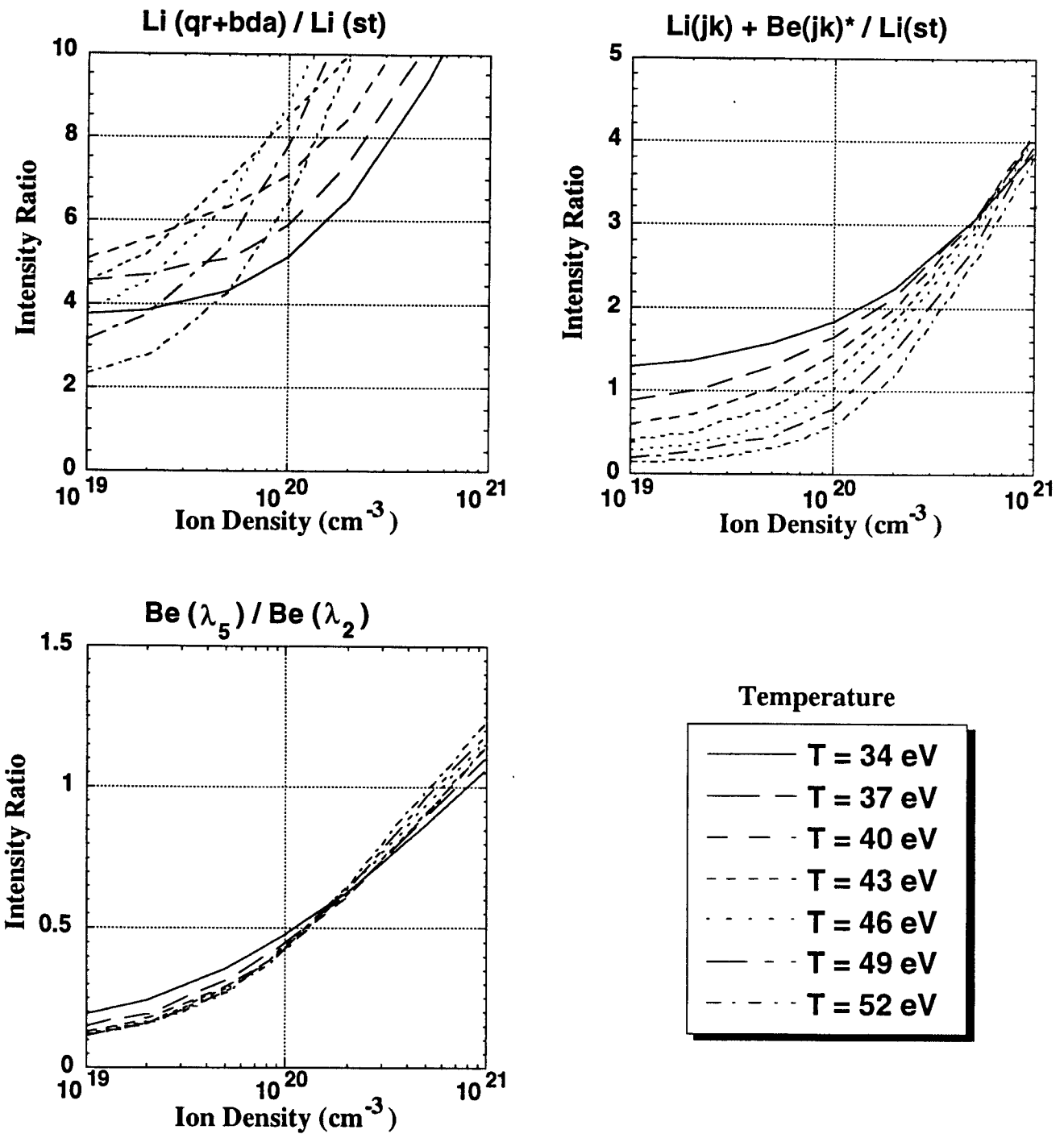

Figure 2.13. Density-sensitive K_α emission line intensity ratios for Al.

spectral resolution provides better constraints for spectral analysis modeling. Good time resolution is of course also important for the analysis of experimental spectra.

2.6. Dielectronic Recombination Effects on K_α Satellite Emission Spectra

In light-ion beam heated plasmas, in addition to inner-shell ion-impact ionization, K_α x-ray line emission can also be produced by dielectronic recombination involving excitation of an electron out of the $1s$ shell; for example:

$$1s^2 2s^2 2p^2 + \varepsilon(l \pm 1) \rightarrow 1s^1 2s^2 2p^3 nl \rightarrow 1s^2 2s^2 2p^2 nl. \tag{2.1}$$

Dielectronic recombination may be thought of as a resonance in a (radiationless) inelastic scattering process in which the incident free electron loses 100% of its kinetic energy, and thereby becomes captured. For sodium ions, to induce dielectronic recombination processes of the type indicated in Eq. (2.1), there must be free electrons with kinetic energies $\varepsilon > 1000$ eV in the plasma. For the plasma conditions of current interest ($N_e \sim 10^{20}$ cm^{-3}, $T_e \lesssim 50$ eV), the fraction of electrons with these high energies is very small. In our previous numerical analyses of K_α satellite line emission spectra, ion-impact ionization by beam ions was assumed to be the dominant populating mechanism for the autoionization levels. Dielectronic recombination was assumed to have a negligible effect. However, the question arises: at what temperature does dielectronic recombination begin to influence the K_α emission spectrum?

To check the effects of dielectronic recombination on K_α satellite emission spectra, we compare the populating rates of autoionizing levels with K-shell vacancies due to the two different processes: ion-impact ionization and dielectronic recombination. These processes are illustrated in Fig. 2.14 for the fluorescing transition:

$$1s^1 2s^2 2p^3 \rightarrow 1s^2 2s^2 2p^2\,. \tag{2.2}$$

The rate at which the $1s^1 2s^2 2p^3$ level is populated by inner-shell ion beam impact ionization can be written as:

$$I_i(1/s) = N_1 \times 6.242 \times \frac{P_{\rm beam}({\rm TW/cm^2})}{E_{\rm beam}({\rm MeV})} \times \sigma({\rm barn})\,, \tag{2.3}$$

where N_1 is the particle density of target ions in level 1 (in cm^{-3}), $P_{\rm beam}$ is the power density of the incident ion beam, $E_{\rm beam}$ is the energy of the ion beam, and σ is the inner-shell ion-impact ionization cross section. The rate for dielectronic recombination is:

$$\alpha_d(1/{\rm s}) = N_3 N_e \times 1.656 \times 10^{-22} \frac{A_a^{4-3}}{T_e({\rm eV})} \times \frac{g_4}{g_3} \exp(-\Delta E_{43}/Te)\,, \tag{2.4}$$

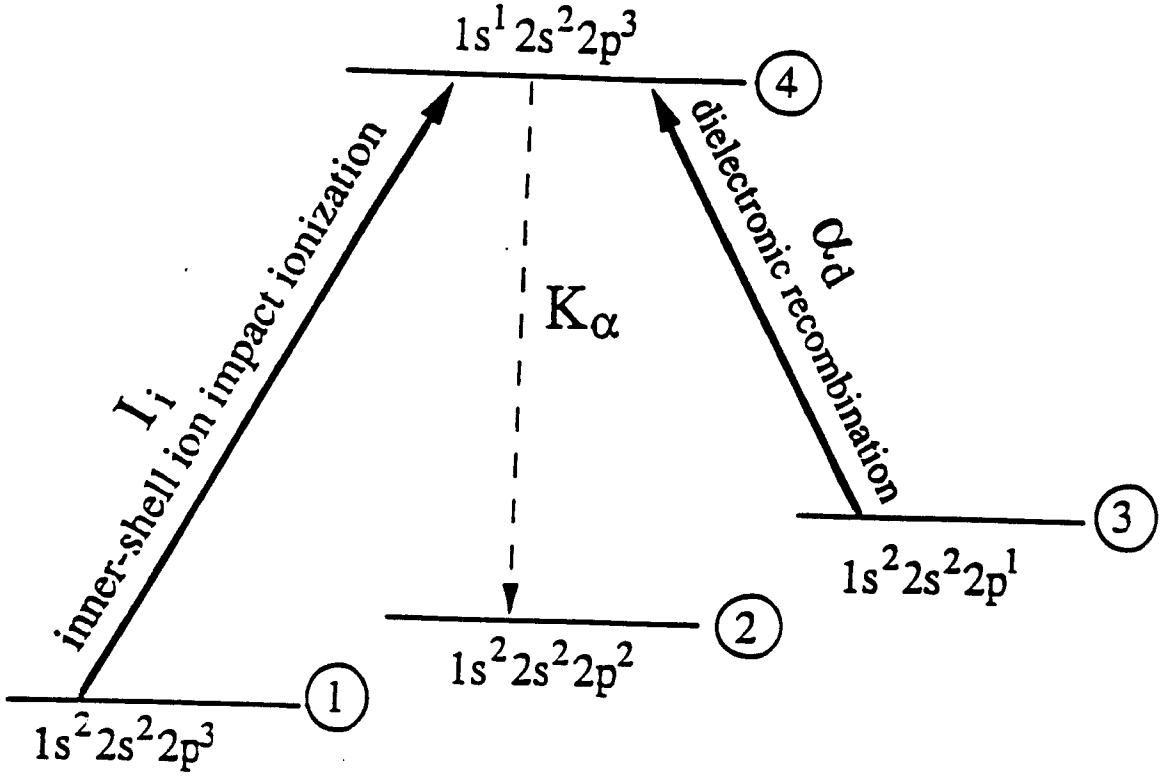

Figure 2.14. Simplified energy level diagram showing competing processes of dielectronic recombination and ion-impact ionization in populating the $1s^1 2s^2 2p^3$ autoionization level.

where N_3 is particle density of ions in level 3 (in cm^{-3}), N_e is electron density, T_e is electron temperature, A_a^{4-3} is the autoionization rate of level 4, and g_3 and g_4 are the statistical weights of level 3 and 4, respectively. Eq. (2.4) is obtained from the inverse (autoionization) process by means of the principle of detailed balance. This expression holds whether or not the ion populations correspond to equilibrium conditions, provided that the free electrons have a Maxwell-Boltzmann velocity distribution.

If $\alpha_d \ll I_i$, the populations of autoionizing levels are determined by inner-shell ion-impact ionization processes, and the effects of dielectronic recombination on K_α emission line spectra can be ignored. At sufficiently high temperatures, however, dielectronic recombination will become important. Below we considered the following dielectronic recombination transitions which result in K-shell vacancies:

- For Li-like Na ions

$$1s^2 + e^- \rightarrow 1s^1 2s^1 2p^1,$$
$$1s^2 + e^- \rightarrow 1s^1 2p^2,$$
$$1s^2 + e^- \rightarrow 1s^1 2p^1 3l^1 (l = s, p, d)\,.$$

- For Be-like Na ions

$$1s^2 2s^1 + e^- \rightarrow 1s^1 2s^2 2p^1,$$
$$1s^2 2s^1 + e^- \rightarrow 1s^1 2s^1 2p^2,$$
$$1s^2 2p^1 + e^- \rightarrow 1s^1 2p^3,$$
$$1s^2 2s^1 + e^- \rightarrow 1s^1 2s^1 2p^1 3l^1 (l = s, p, d).$$

- For B-like Na ions

$$1s^2 2s^2 + e^- \rightarrow 1s^1 2s^2 2p^2,$$
$$1s^2 2s^1 2p^1 + e^- \rightarrow 1s^1 2s^1 2p^3,$$
$$1s^2 2p^2 + e^- \rightarrow 1s^1 2p^4,$$
$$1s^2 2s^2 + e^- \rightarrow 1s^1 2s^2 2p^1 3l^1 (l = s, p, d).$$

To compute dielectronic recombination rates, one must first calculate the related autoionization transition probability A_a. We have calculated autoionization probabilities from the first-order perturbation theory expression [26]:

$$A_a(\gamma_i, 1s, \epsilon l_4, L'S'J' \rightarrow \gamma_f, n_1 l_1, n_2 l_2, LSJ) = 2\pi \sum | < i|1/r_{12}|f > |^2 \qquad (2.5)$$

and

$$< i|1/r_{12}|f >= \sum_k x_k R^k(1s, \epsilon l_4; n_1 l_1, n_2 l_2|r), \tag{2.6}$$

where A_a is the autoionization rate in atomic units, the transition $(1s, \epsilon l) \rightarrow (n_1 l_1, n_2 l_2)$ refers to the exchange of holes between the initial and final states, x_k is a coefficient related to the angular momentum coupling and can be expressed with $3j$ and $6j$ symbols, and the $R^k(r)$ are radial integrals defined as follows:

$$R^k(l_1 l_2 l_3 l_4) = \int_0^\infty \int_0^\infty \frac{r_<^k}{r_>^{k+1}} P^*_{n_1 l_1}(r_i)\, P^*_{n_2 l_2}(r_j)\, P_{n_3 l_3}(r_i)\, P_{\epsilon l_4}(r_j)\, dr_i\, dr_j\,. \tag{2.7}$$

The radial wavefunctions $P_{nl}(r)$ are calculated by solving the Hartree-Fock equations. The continuum wavefunction $P_{\epsilon l}(r)$ for a free electron of kinetic energy $\epsilon = \Delta E_{34}$ is normalized to $\delta(\epsilon - \epsilon')$. This continuum function is obtained from solving a radial Schrödinger equation by using the HX method [27].

In our calculations, atomic structure data and autoionization rates are calculated using an intermediate coupling scheme with all fine-structure components of the $2p - 1s$ transitions taken into account. Free electrons are assumed to have a Maxwellian distribution with density $N_e = 5 \times 10^{20}$ cm^{-3}.

Figure 2.15 shows the populating rates of various autoionizing levels due to dielectronic recombination for Li-like Na ions. Also shown in the figure are the corresponding ion-impact ionization rates by a 0.2 TW/cm^2, 1 MeV proton beam. In the figure, the ion-impact ionization rates are marked with two horizontal lines, which indicate the variation of ionization cross sections with the different target states. It can be seen from the figure that dielectronic recombination rates are sensitive to the final autoionization states. For example, the dielectronic recombination rate for $1s^2 + e^- \rightarrow 1s^1 2p^1 3d^1$ is about two orders of magnitude smaller than that for the $1s^2 + e^- \rightarrow 1s^1 2s^1 2p^1$ transition at $T = 100$ eV. This is because higher velocity electrons are required to induce dielectronic recombination for $1s^2 + e^- \rightarrow 1s^1 2p^1 3d^1$, and the number of high velocity electrons decreases very rapidly for low temperature plasmas. For the same target state, dielectronic recombination rates are smaller for higher energy recombined autoionizing states. In other words, for K_α emissions produced by the dielectronic recombination process, the intensity of emissions from excited states with M-shell spectator electrons will be weaker than those from lower states such as $1s^1 2s^1 2p^1$. Similarly, for K_α emissions induced by ion-impact ionization, the K_α lines from transitions involving excited configuration states with M-shell spectator electrons are usually weaker than those from ground configuration states because of the lower populations of excited configuration states.

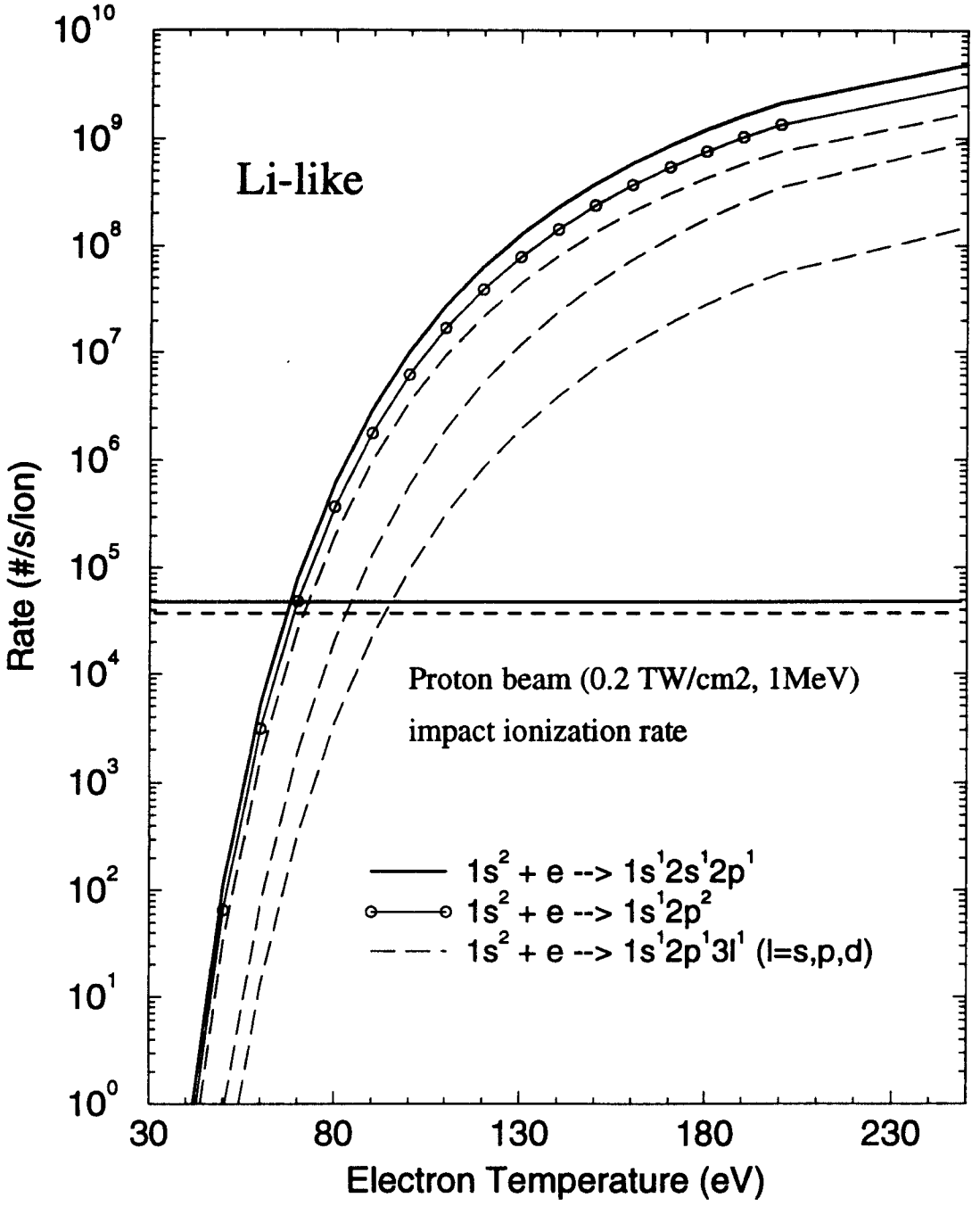

Figure 2.15. Temperature dependence of dielectronic recombination rate coefficients for various transitions resulting in Li-like Na with a K-shell vacancy. The horizontal lines represent ion-impact ionization rate coefficients for transitions populating the same autoionizing levels. Note that ion-impact ionization dominates for plasma temperatures $\lesssim 50$ eV.

Note that for relatively low temperature sodium plasmas ($T_e \lesssim 50$ eV), the dielectronic recombination rate coefficients are much smaller than the ion impact ionization rate coefficients. Thus the effects of dielectronic recombination on the K_α satellite emission spectra will be unimportant for these conditions. (Note the rates are *per ion*, so that N_1 and N_3 in Eqs. (2.3) and (2.4) are not actually computed.) The dielectronic recombination rate increases very rapidly as the plasma temperature increases. Figure 2.15 shows that dielectronic recombination rates become competitive with ion-impact ionization rates when $T_e \gtrsim 60$ eV. In fact, at $T_e \gtrsim 100$ eV dielectronic recombination becomes the dominant process in producing K-shell vacancies. Similar results are obtained for Be- and B-like ions, which are shown in Figs. 2.16 and 2.17.

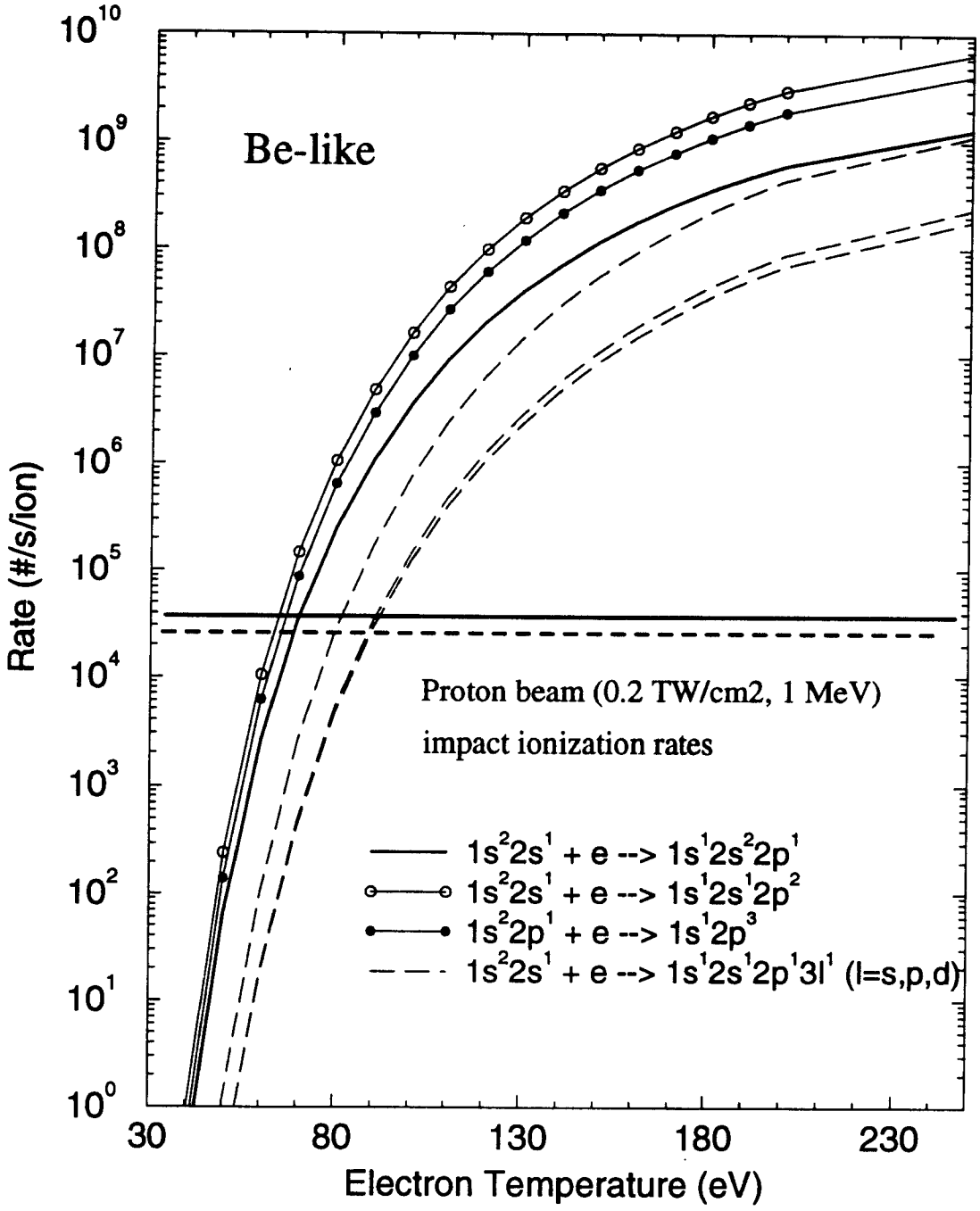

Figure 2.16. Temperature dependence of dielectronic recombination rate coefficients for various transitions resulting in Be-like Na with a K-shell vacancy. The horizontal lines represent ion-impact ionization rate coefficients for transitions populating the same autoionizing levels. Note that ion-impact ionization dominates for plasma temperatures $\lesssim 50$ eV.

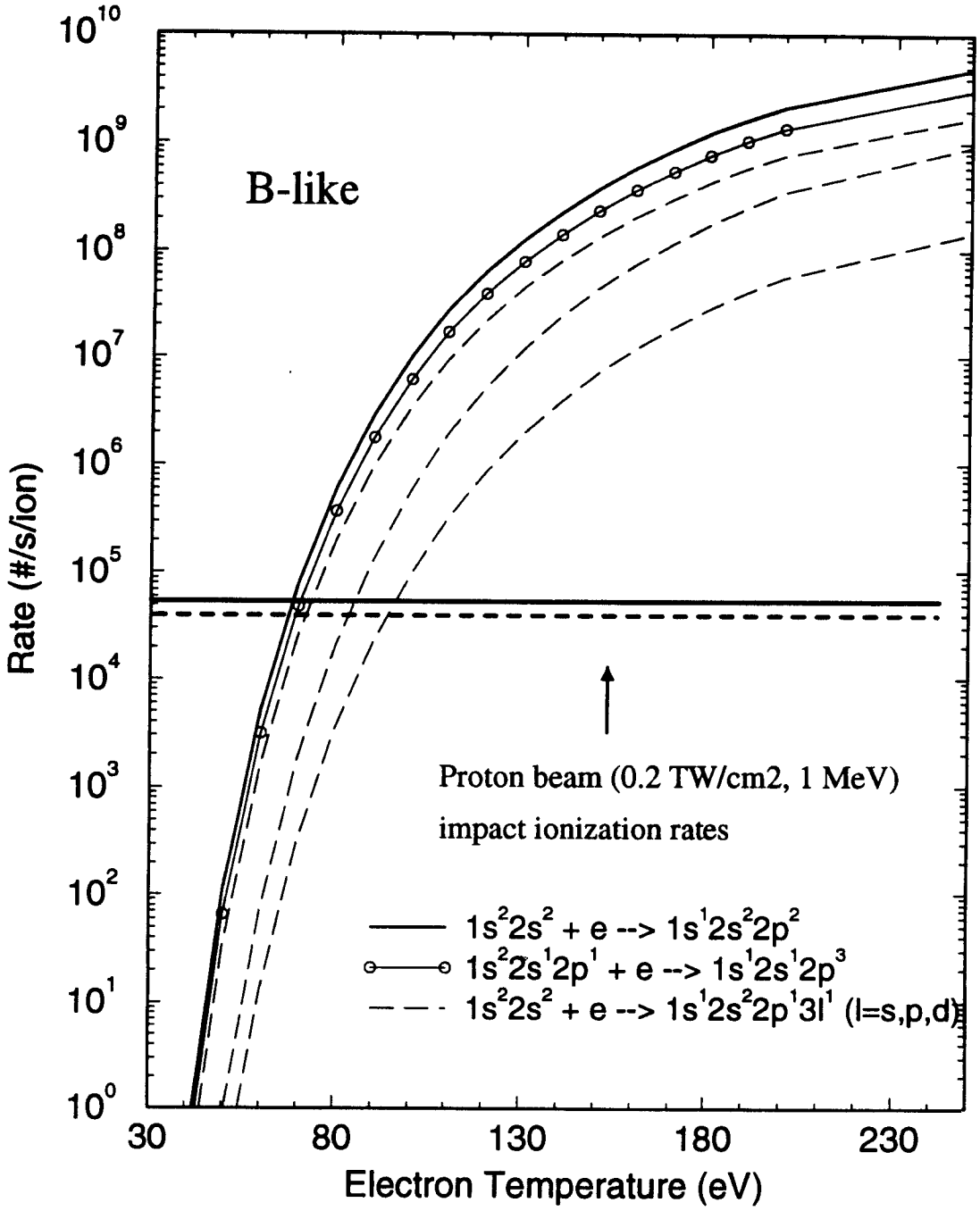

Figure 2.17. Temperature dependence of dielectronic recombination rate coefficients for various transitions resulting in B-like Na with a K-shell vacancy. The horizontal lines represent ion-impact ionization rate coefficients for transitions populating the same autoionizing levels. Note that ion-impact ionization dominates for plasma temperatures $\lesssim 50$ eV.

3. Radiation-Hydrodynamics Simulations of KALIF Beam-Plasma Interaction Experiments

We performed radiation-hydrodynamics simulations for upcoming KALIF beam-plasma interaction using the Wisconsin BUCKY-1 code [4]. The purpose of the simulations is to gain a better insight into the sensitivity of the predictions to uncertainties in various models (e.g., stopping power, radiation physics), and also to allow for a comparison with KfK KATACO simulations. Simulations for both B_θ diode and applied-B diode experiments were performed. In addition, results of B_θ diode simulations were post-processed with our CRE spectral analysis code to predict time-dependent and time-integrated K_α satellite spectra for the Na tracer layer. A discussion of the physics models in our radiation-hydrodynamics code is presented in Section 3.1. Results from B_θ and applied-B diode simulations are presented in Sections 3.2 and 3.3, respectively. K_α satellite spectra for the B_θ diode simulation are shown in Section 3.4.

3.1. Radiation-Hydrodynamics Models

Calculations were performed using the BUCKY-1 radiation-hydrodynamics code. As is illustrated in Fig. 3.1, this code integrates physics models from several codes: PHD-IV, CONRAD, NLTERT, and EOSOPA. PHD-IV [5] is an ICF target physics code which simulates implosions, explosions, ion beam energy deposition, fusion burn, charged particle transport, and target breakup. It is a 1-D Lagrangian code which solves the single-fluid equation of motion with pressure contributions from electrons, ions, radiation, and fast charged particle reaction products. Energy transport in the plasma is treated with a two-temperature model — i.e., separate ion and electron temperatures. Radiation emission and absorption terms couple the electron temperature equation to the radiation transport equations. Radiation is transported using either a multigroup Eddington factor model or a multigroup diffusion model.

CONRAD [6] is a 1-D radiation-hydrodynamics code which descended from PHD-IV and MF-FIRE [28]. It is used to study the radiative and hydrodynamic processes within ICF target chambers following the explosion of a high-gain target. It includes models to simulate the stopping of target x-rays and fast debris ions in a buffer gas and the target chamber first wall. Time-dependent vaporization of the first wall is also simulated.

NLTERT [1] is a non-LTE radiative transfer code which has been used to analyze spectra obtained in laboratory plasma experiments. Selected parts of this code were recently incorporated into KATACO and BUCKY-1 [10]. When this model is invoked, atomic level populations are calculated using a collsional-radiative equilibrium (CRE) model at

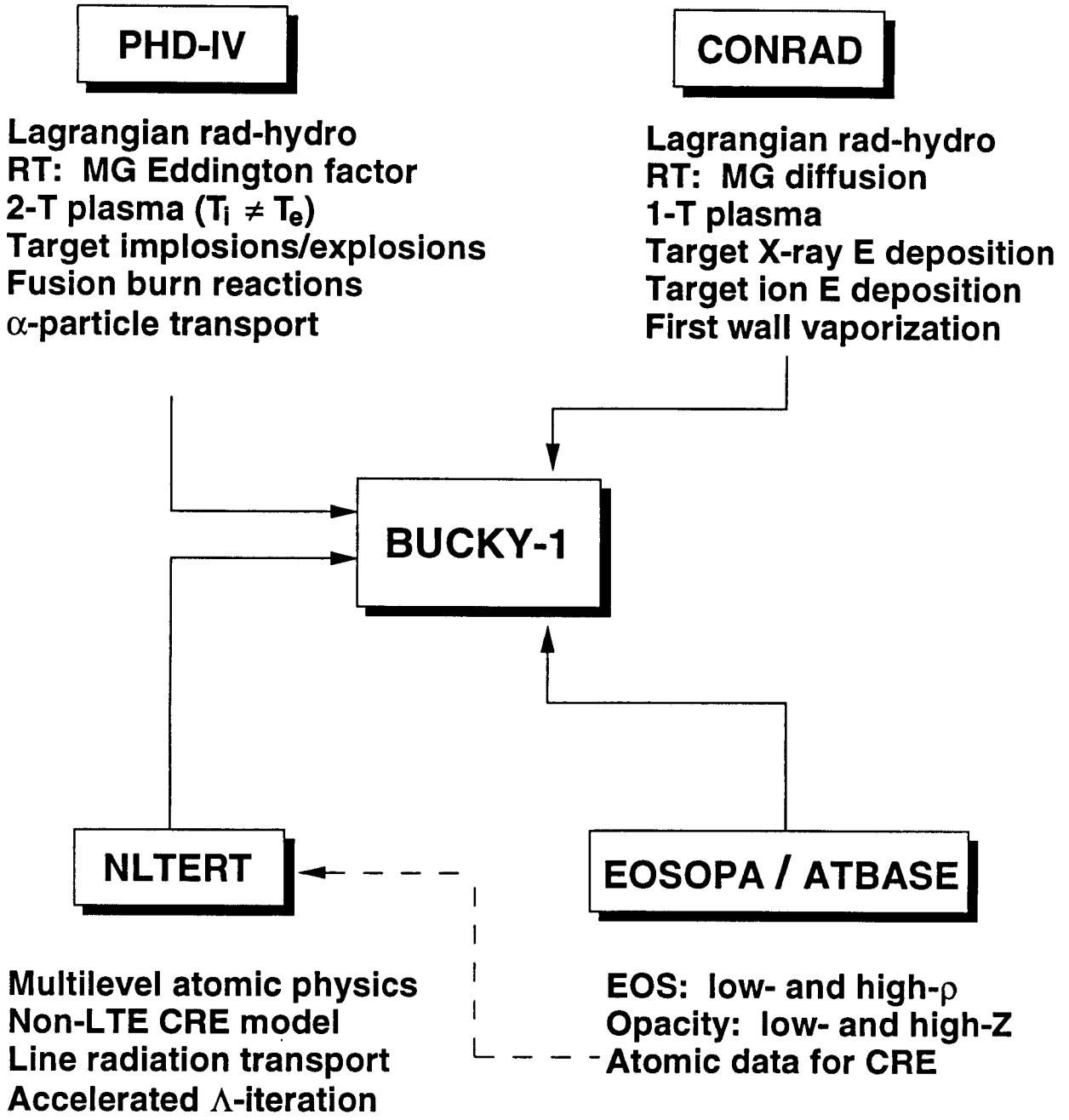

Figure 3.1. Schematic illustration of codes used to build the BUCKY-1 radiation-hydrodynamics code.

each hydrodynamic time step. By default, the atomic populations are computed self-consistently with the radiation field; however, options also exist where the user can specify that LTE (local thermodynamic equilibrium) populations or optically thin populations (i.e., where photoexcitation and photoionization are neglected) be used. After the atomic level populations are computed, radiation losses due to line emission are computed using an escape probability radiation transport model [29,30]. This model was recently used to study radiation transport effects in ICF target chambers with a single-species buffer gas [31]. Modifications are currently underway to simulate ion beam-heated multilayer targets, such as the plastic sandwich target illustrated in Fig. 2.2.

EOSOPA [3] and ATBASE [2] are a suite of atomic physics codes which generate atomic data for equations of state, multigroup opacities, and spectral analyses. Equation of state tables are generated using a hybrid model in which high-density thermodynamic properties are calculated using a muffin-tin model, while lower density properties are computed using a detailed configuration accounting (DCA) model. EOSOPA also computes high quality opacities for both low-Z and high-Z materials. Detailed descriptions of the equation of state and opacity models are provided in Section 4.

In the simulations described below the following models and options were used. Ion stopping powers were computed using a model based on the work of Mehlhorn [32]. In some cases, the stopping power was multiplied by a factor of 2 to assess the sensitivity of the peak target temperature to possible uncertainties in the (dE/dx) model and the measured proton beam parameters. Radiation was transported using a multigroup diffusion model with 20 frequency groups. Line emission and absorption were included in the multigroup opacities. Because it is believed that this model tends to overestimate radiation losses, some calculations were performed with no radiation absorption or emission. Simulations with detailed line radiation transport were not performed because the model is currently being modified to simulate *multilayer* targets (these modifications are nearly complete at the time of this writing). Also in this calculation, the 1-T plasma model was used (i.e., $T_{ion} = T_{electron}$) as the 2-T model in BUCKY-1 is still being tested. For the KALIF experiments, it is expected that the ion and electron temperatures should be closely coupled.

3.2. Simulation of B_θ Diode Experiments

The initial conditions for the target are illustrated in Fig. 3.2. The Al and Na tracer thicknesses are 5000 Å each, while the CH tamper thicknesses are 1400 Å. The beam enters the Al tracer before it enters the Na. The beam power and kinetic energy (voltage) entering the target for the B_θ diode simulations is shown in Fig. 3.3. These parameters are based

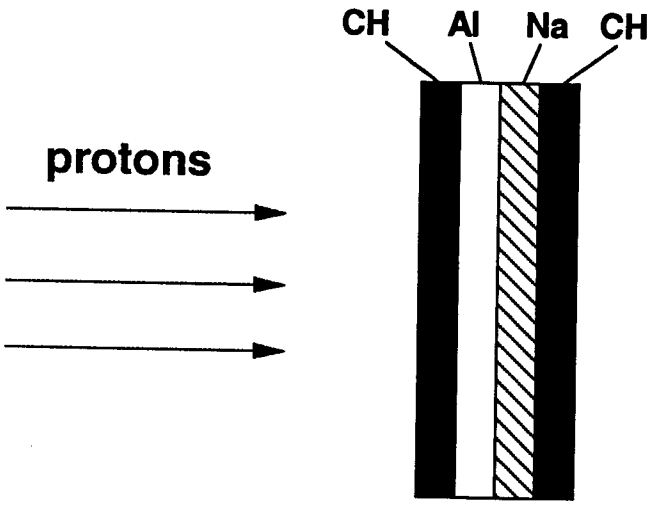

Material	Thickness (Å)	Density (g/cm^3)
CH	1400	1.1
Al	5000	2.7
Na	5000	1.0
CH	1400	1.1

Figure 3.2. Initial target conditions used in simulation of KALIF target heating experiments.

on KALIF measurements [33]. Here, it is seen that a peak power density of 0.15 TW/cm^2 is attained at 35 ns. The beam voltage is $E_B \approx$ 1.25-1.4 MeV at $t \lesssim 35$ ns. After this time both the beam power density and voltage are seen to decrease roughly linearly with time.

Figure 3.4 shows simulation results for the spatial dependence of the plasma temperature, pressure, fluid velocity, and mass density at simulation times of 20, 40, 60, and 80 ns. Note that the peak temperatures are reached at about 80 ns, which is well after the peak in the beam power density. This is due to the fact that significant heating occurs at late times when the beam energy decreases. This can be clearly seen in Fig. 3.5, where the specific beam energy deposition in Al is plotted as a function of proton energy. At later times in the simulation the proton beam energy decreases and the mean ionization state of the target increases. Both effects contribute to a higher specific energy deposition rate. For example, at $t = 40$ ns — when the beam energy is approximately 1.2 MeV and the Al is mainly in Al III and Al IV, the current density is about 0.12 MA/cm^2 and the specific energy deposition in the Al is about 25 TW/g. At $t = 80$ ns, the current density has risen slightly to 0.16 MA/cm^2, but because of the lower beam voltage the specific energy deposition has risen to approximatley 160 TW/g.

It is also seen at late times that the plastic tamper regions become hotter than the Al and Na layers. This appears to at least in part be due to the ionization structure of the CH at late times. (This is <u>not</u> simply due to radiation effects because a similar situation occurs in simulations where radiation is turned off.) By 65 ns, the H is fully ionized while the C approaches C V; i.e., He-like C. Continued ionization of carbon to higher stages becomes difficult because of the higher ionization threshold for C V. As energy is deposited in the CH region, most of it goes into translational energy (i.e., temperature) as opposed to ionization energy. Thus, the beam is able to more efficiently raise the temperature of the CH.

By the time of maximum temperature, the density in the Al and Na tracer regions has fallen to between 10^{-4} and 10^{-3} of solid density. The peak pressure attained in the target is about 300 GPa (= 3 Mbar). Expansion velocities within the Na and Al regions are $\lesssim$ 5 cm/μs.

The time-dependent average temperatures for each of the target layers is shown in Fig. 3.6. The curves shown represent mass-weighted temperatures from the Lagrangian hydrodynamic zones. It is seen that the peak temperature is approximately 20 eV for both the Al and Na tracer regions. The peak temperature in the near-side tamper (i.e., the region facing the incoming proton beam) is 32 eV, while the far-side tamper is predicted

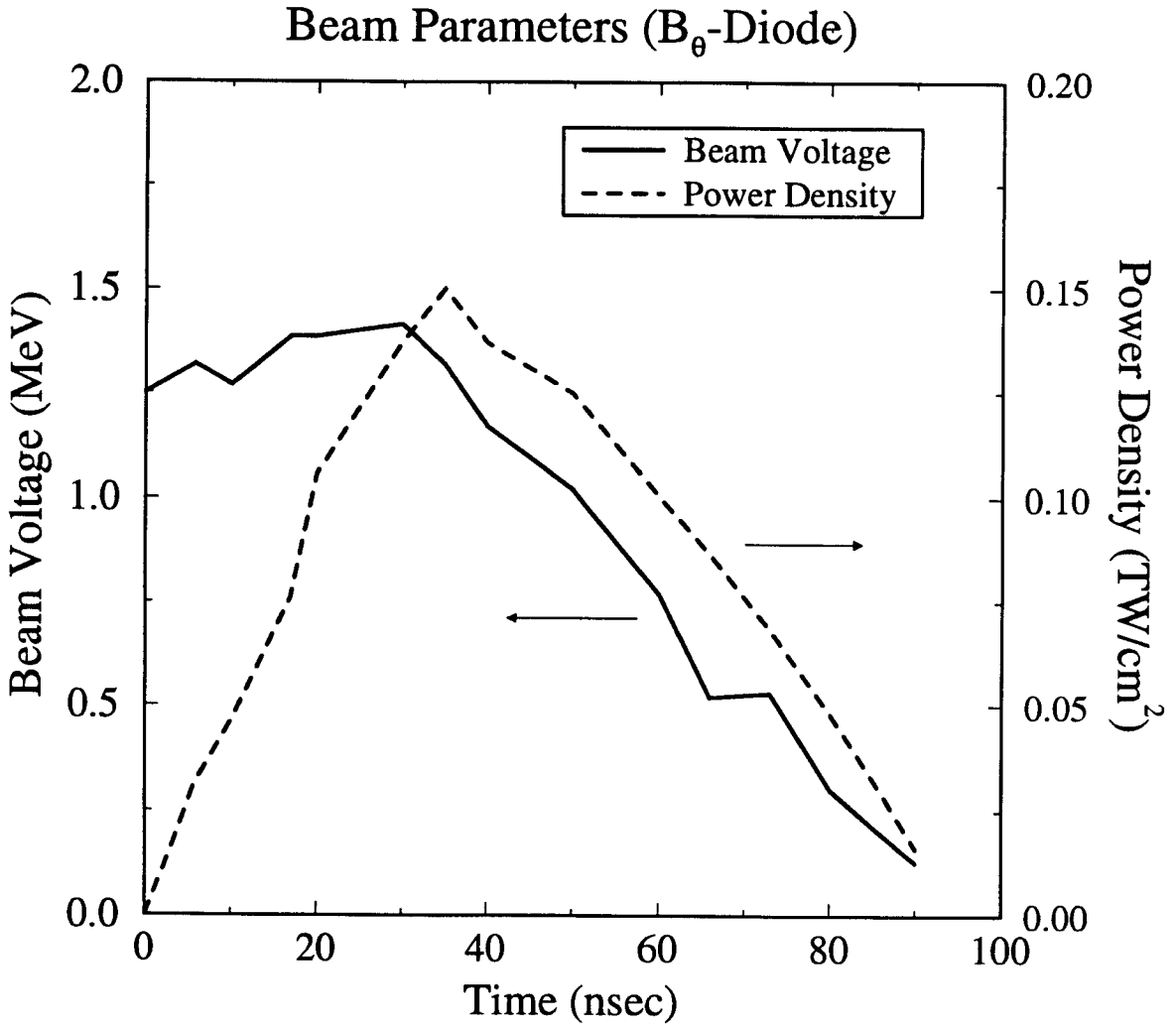

Figure 3.3. Time-dependent proton beam energy (voltage) and power density used in simulation of KALIF B_θ diode experiments.

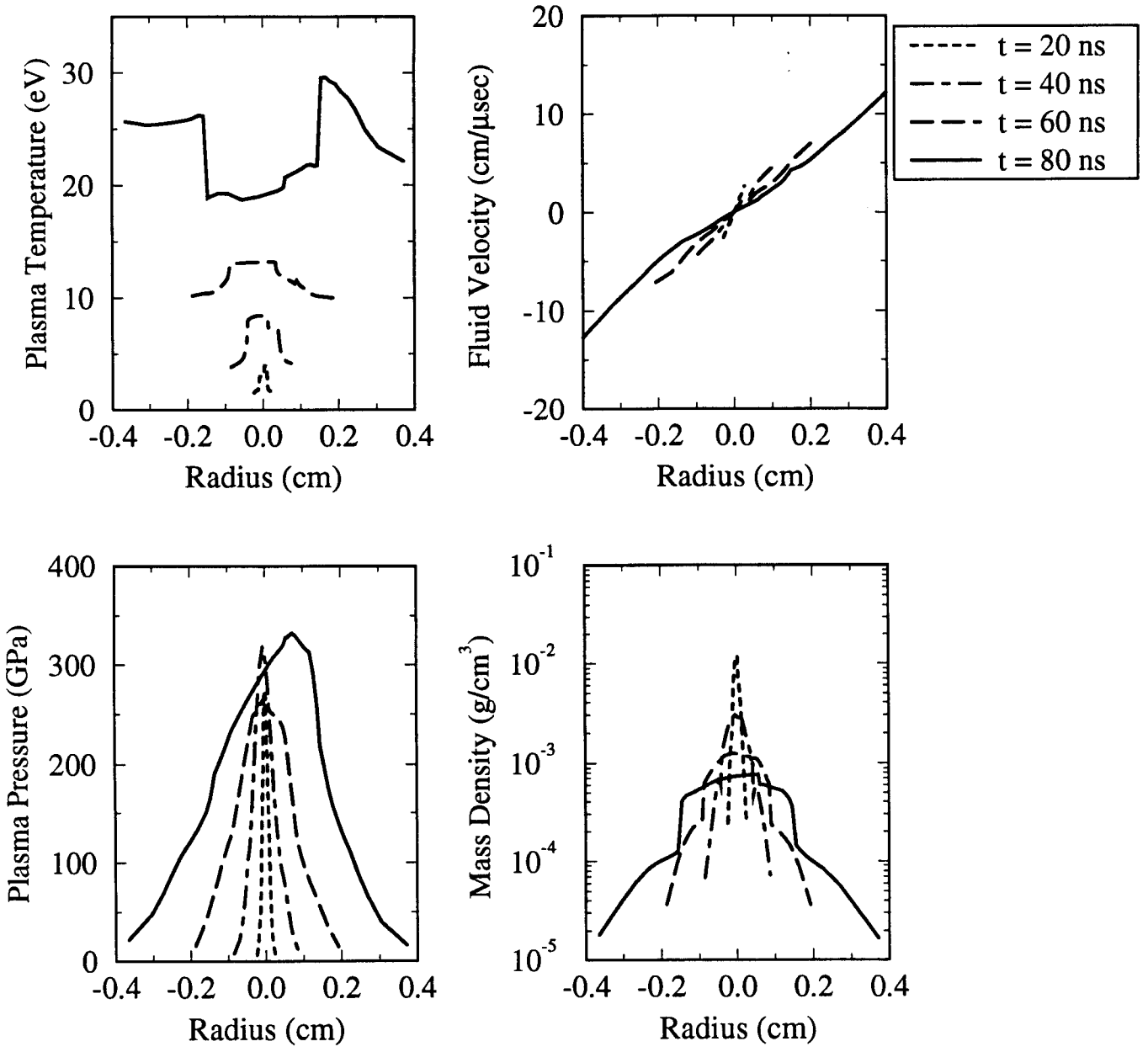

Figure 3.4. Spatial distribution of plasma temperature, pressure, fluid velocity, and mass density at times of 20, 40, 60, and 80 ns for the baseline B_θ diode simulation.

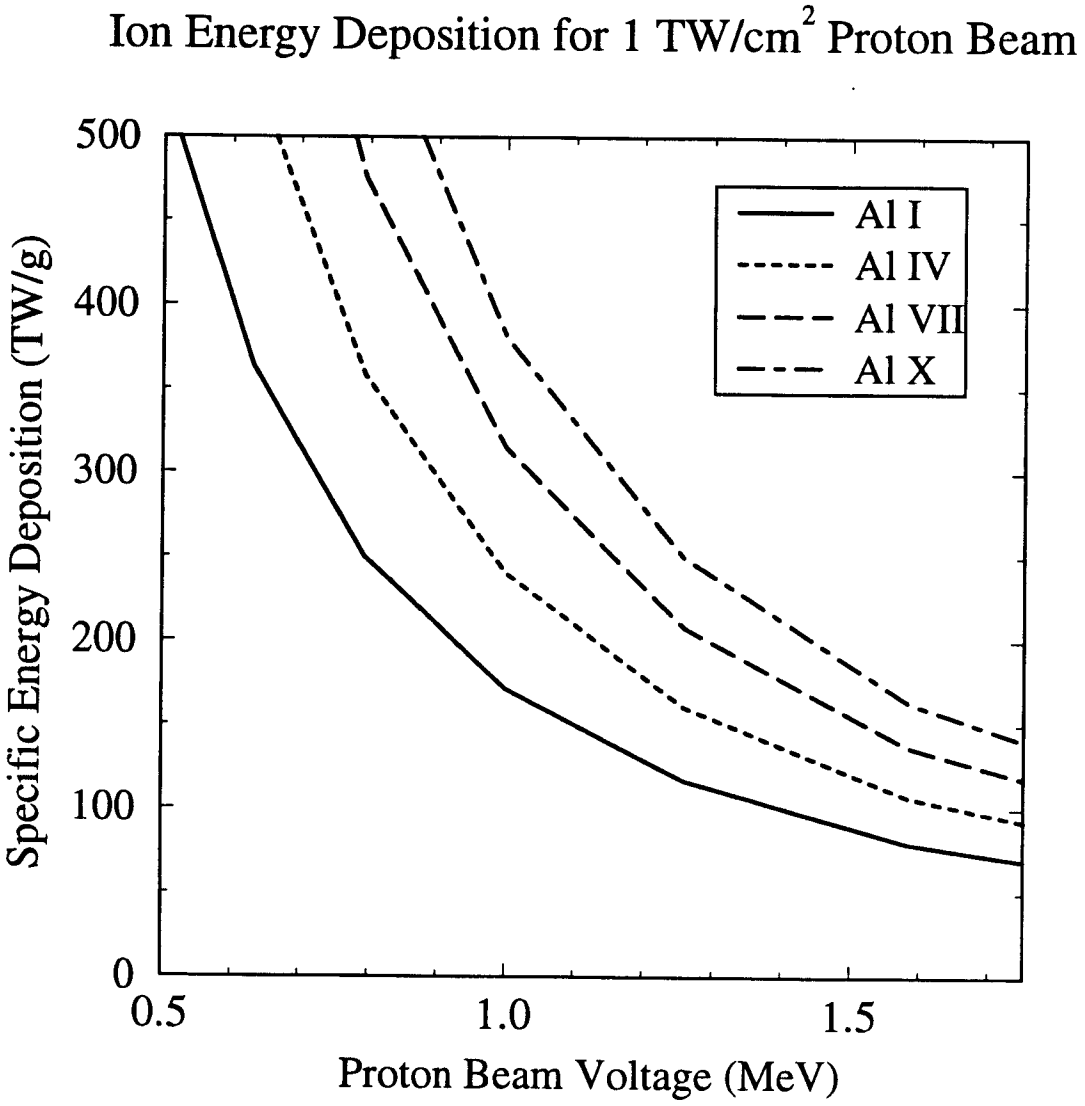

Figure 3.5. Specific energy deposition in Al as a function of proton beam energy. Note the strong sensitivity to both beam energy and ionization state of the Al target.

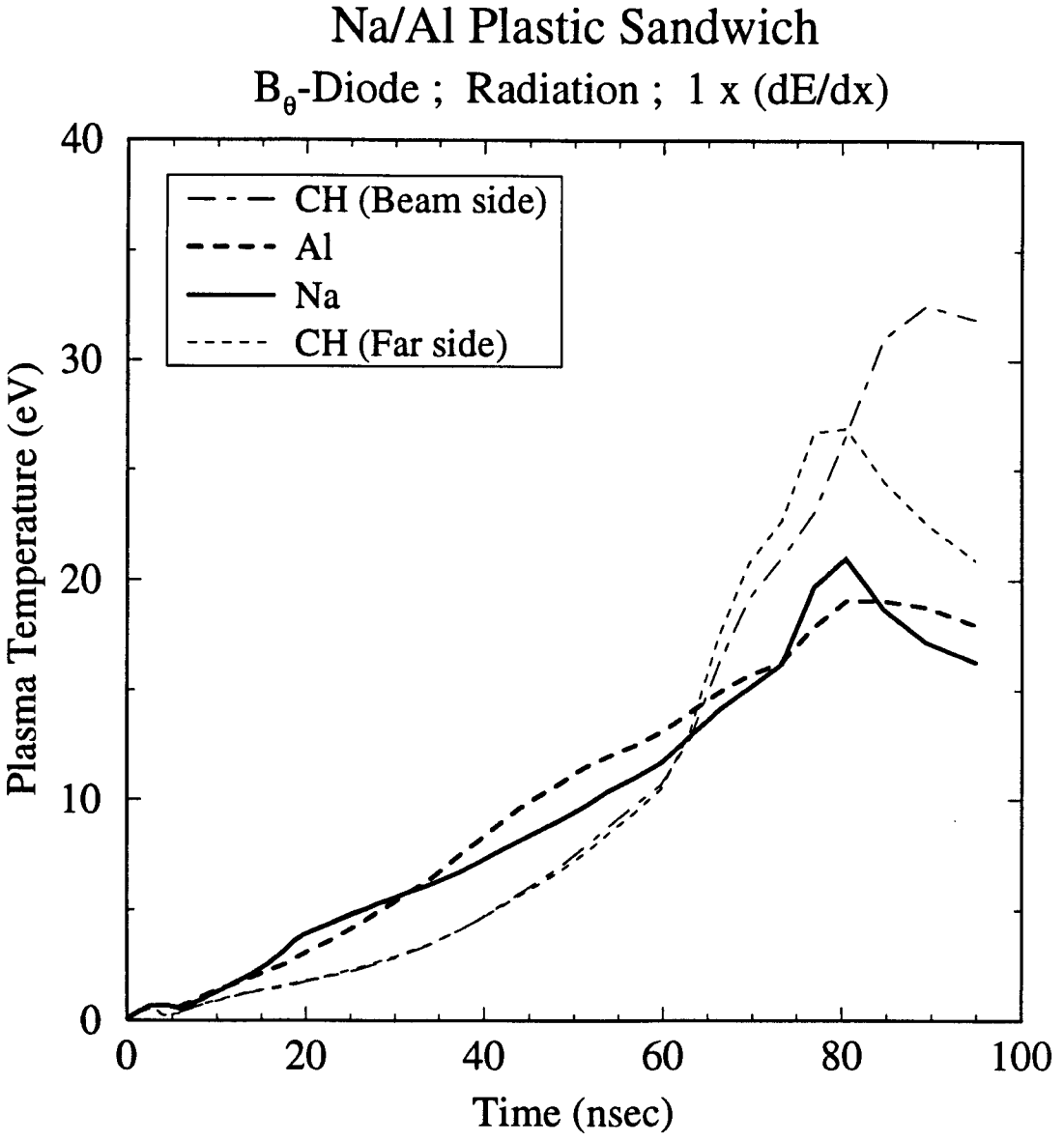

Figure 3.6. Time-dependence of spatially-averaged temperatures in each target region for the baseline B_θ diode simulation.

to reach a maximum of 27 eV. The near-side tamper reaches a higher temperature because the beam ions range out (i.e., are stopped) in the Al and Na at late times.

The conclusion from our baseline simulations is that the Al and Na tracers should attain temperatures of approximately 20 eV. One can then ask: what is the sensitivity of these predictions to the modeling? To address this we have performed additional simulations in which: (a) radiation losses were neglected, and (b) the stopping power was multiplied by a factor of 2. Results for these cases are shown in Figs. 3.7 and 3.8. For the results with no radiation and the nominal stopping power (Fig. 3.7) the peak temperature in the Al and Na tracers is 27 eV, while that in the far-side CH tamper is 24 eV. The near-side CH tamper reaches a maximum of 43 eV. Again, the near-side tamper continues to be heated at late times ($t \gtrsim 80$ ns), where the beam voltage is low ($E_B \lesssim 0.3$ MeV).

Figure 3.8 shows temperatures from a simulation with both (i) no radiation losses, and (ii) a $(\frac{dE}{dx})$ which is enhanced by a factor of 2. This factor of 2 could account for inaccuracies in either the stopping power value (which could be reflected in the model itself or in the target ionization state $\langle Z \rangle$ in the simulation), or the beam parameters (in particular, voltage and current density). In this simulation, the peak temperature in both the Al and Na tracers is 41 eV. Because neglecting radiation losses and artificially increasing the stopping power result in higher tracer temperatures, $T = 40$ eV for the tracers should be considered the maximum temperature attainable for the B_θ diode experiments (assuming, of course, the beam parameters used in the simulation are accurate).

Note that the peak temperature depends very much on the beam properties at late times ($t \gtrsim 60$ ns). At these times, the beam power density and voltage have each fallen to $\lesssim$ half of their peak values. Thus, the peak ionization states seen in the K_α satellite spectra should be sensitive to the beam parameters at $t \approx$ 60-100 ns. *This suggests that achieving a good understanding of some of the key physics processes in these experiments will require a good measurement of the beam properties* <u>*at late times*</u>.

Note also that measurements of the K_α satellite spectrum from the Na and Al tracers should provide valuable constraints for the simulations. For instance, the peak temperatures in the B_θ diode simulations just discussed were 20, 27, and 41 eV. Figure 2.10 ($n = 10^{19}$ cm^{-3}) shows that at $T = 20$ eV the strongest K_α emission is from Be- and B-like Na. At $T = 27$ eV, the He- and Li-like Na satellites should be strongest, while at $T = 40$ eV the He_α emission line should be significantly stronger than any of the other satellites. In fact, since peak tracer temperatures in the B_θ diode experiment may very well be in $T \approx$ 20-25 eV range, using intensity ratios from the Na He-like to Li-like satellites should provide for a good plasma diagnostics (see Section 2.5).

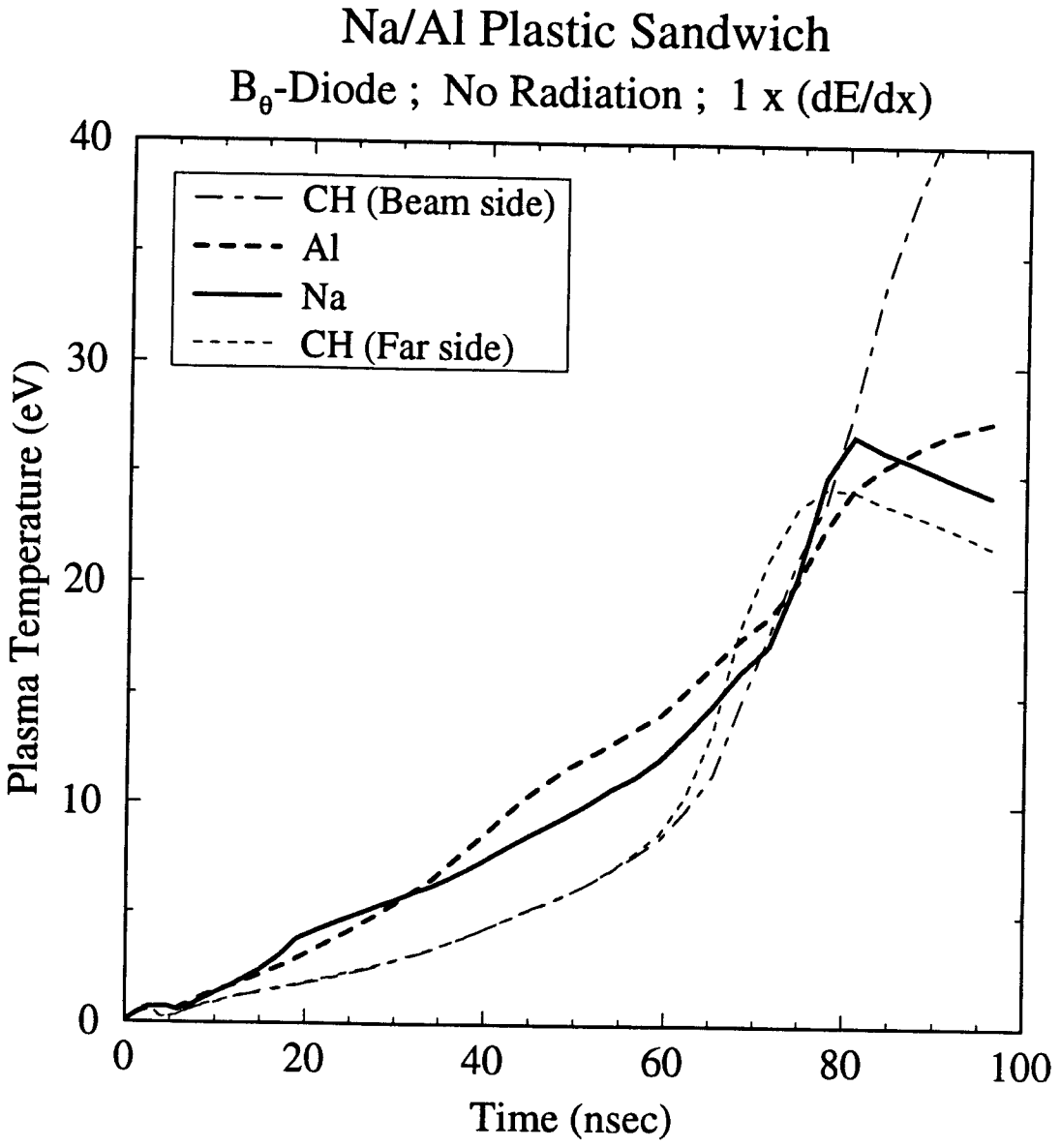

Figure 3.7. Time-dependence of spatially-averaged temperatures in each target region for the B_θ diode simulation with no radiation losses.

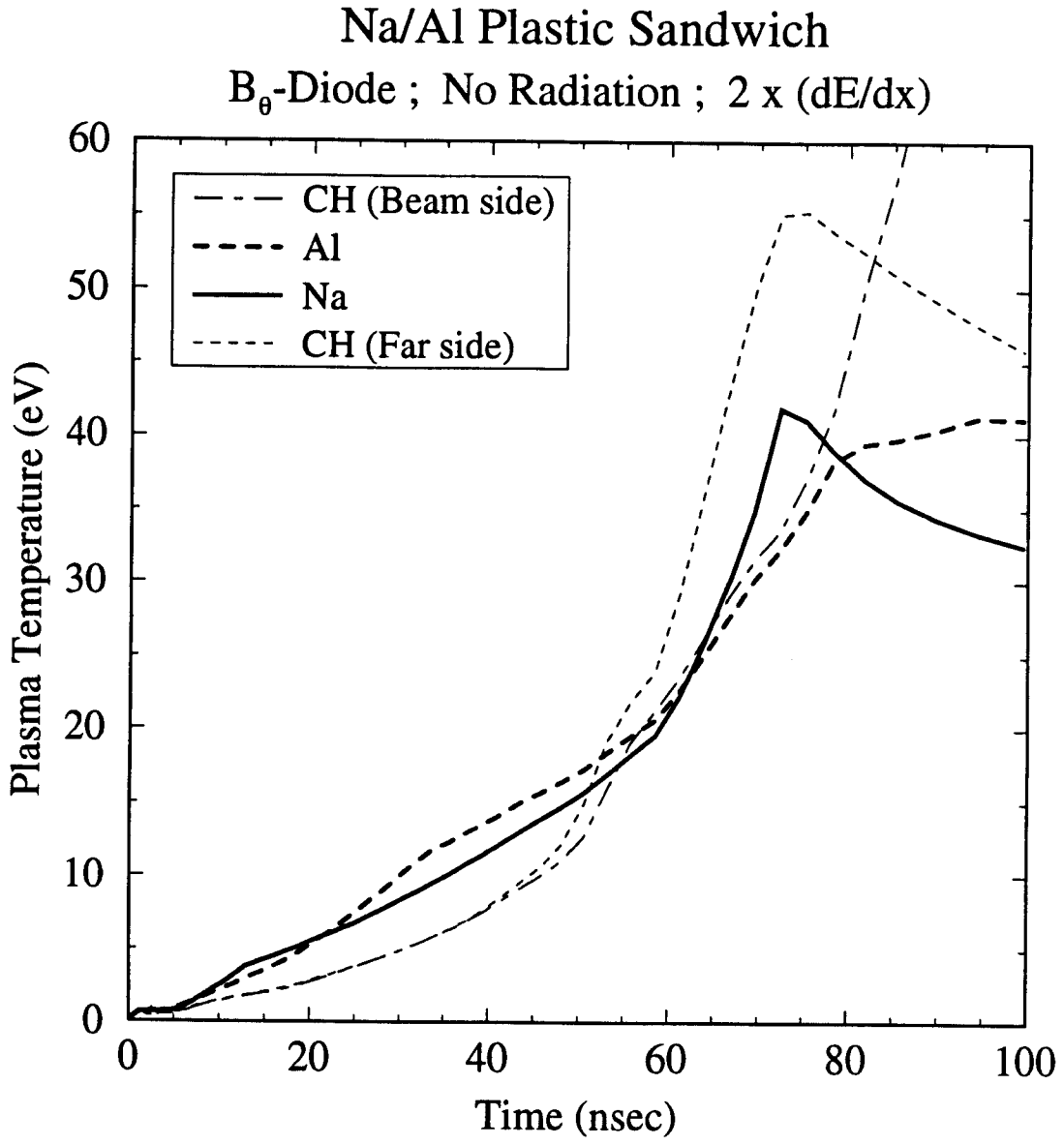

Figure 3.8. Time-dependence of spatially-averaged temperatures in each target region for the B_θ diode simulation with no radiation losses and with stopping powers enhanced by a factor of 2.

3.3. Simulation of Applied-B Diode Experiments

A similar series of simulations were performed for KALIF beam-plasma interaction experiments using the applied-B diode. In this case, the beam power density and voltage were modeled using a 60 ns square pulse, with $P_B = 1.0$ TW/cm^2 and $E_B = 1.5$ MeV. The purpose of the calculations was to predict very roughly the peak temperatures that might be attained in the applied-B diode experiments, and to determine the sensitivity of the predicted temperatures to the radiation and stopping power model. The target is the same as that for the B_θ diode simulations (see Fig. 3.2).

Results for the time-dependent (spatially-averaged) temperatures in each layer are shown in Figs. 3.9 – 3.11. Figure 3.9 represents results from the simulation with radiation losses included and nominal (no multiplier) stopping powers. The peak temperatures in the Na and Al tracers are 23-24 eV, while that for the CH tampers is 32 eV. These temperatures are not significntly higher than the B_θ diode baseline simulation (see Fig. 3.6). The reason is due to the fact that: (1) radiation losses are very significant in the applied-B diode simulation (notice how the temperature curves remain relatively flat at $t \gtrsim 30$ ns), and (2) the beam voltage is assumed to be constant with time, instead of dropping significantly as in the B_θ diode case.

The fact that radiation losses are important in the applied-B diode case can be seen by examining Fig. 3.10, which shows results from a simulation in which radiation losses were neglected. In this case the peak temperatures in the Na and Al tracers are 58 and 47 eV, which are a factor of 2 or more higher than in the radiation case. Our previous experience in studying radiation losses in thin, moderate density plasmas of this type (moderate-Z, optically thin to continuum but optically thick to lines) suggests that the radiation model used in the baseline calculation — i.e., a multigroup diffusion model with line radiation effects included in the multigroup opacities — can significantly overestimate radiation energy losses. Therefore, peak temperatures of ~ 40 eV in the applied-B diode experiments may be reasonable.

Figure 3.11 shows results from a simulation in which radiation losses are neglected and the stopping power was enhanced by a factor of 2. It is seen that peak temperatures for the Na and Al tracers are approximately 130 eV. It seems unlikely, however, that temperatures above 100 eV would be reached in KALIF experiments because radiation losses should become significant. The significance of the results is that they show the large sensitivity of the predicted temperature to the details of the modeling.

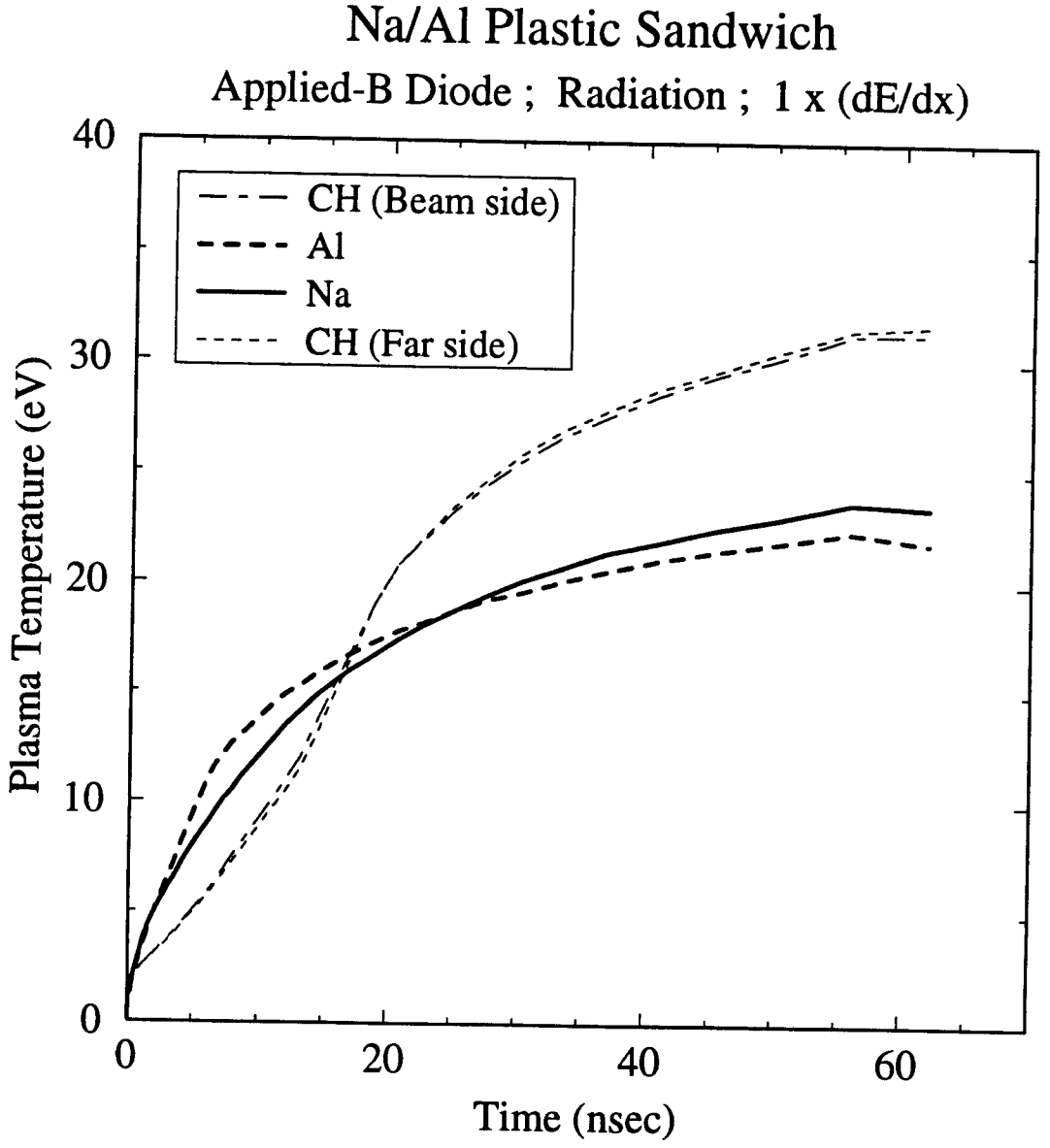

Figure 3.9. Time dependence of spatially-averaged temperatures in each target region for the baseline applied-B diode simulation.

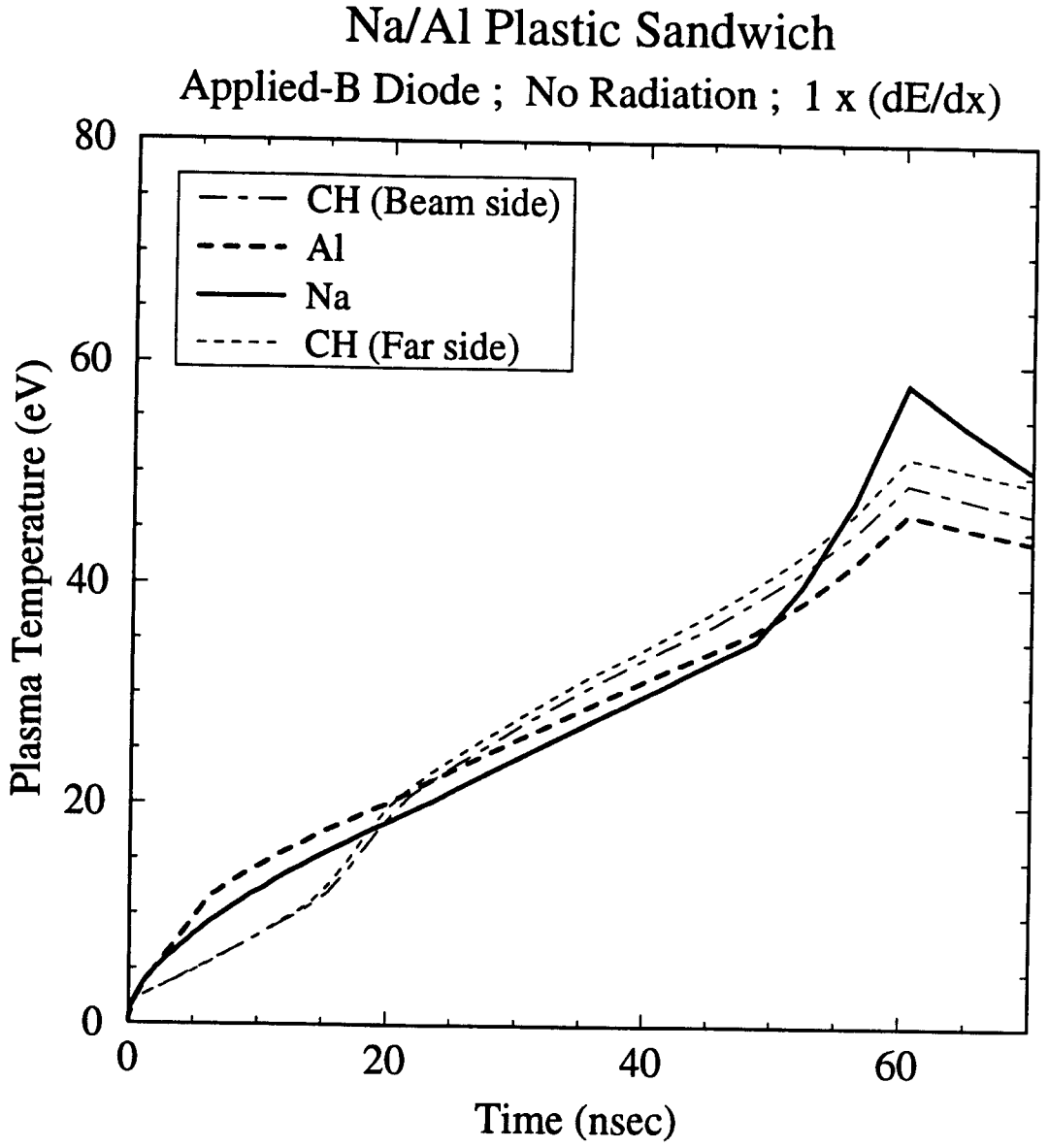

Figure 3.10. Time dependence of spatially-averaged temperatures in each target region for the applied-B diode simulation with no radiation losses.

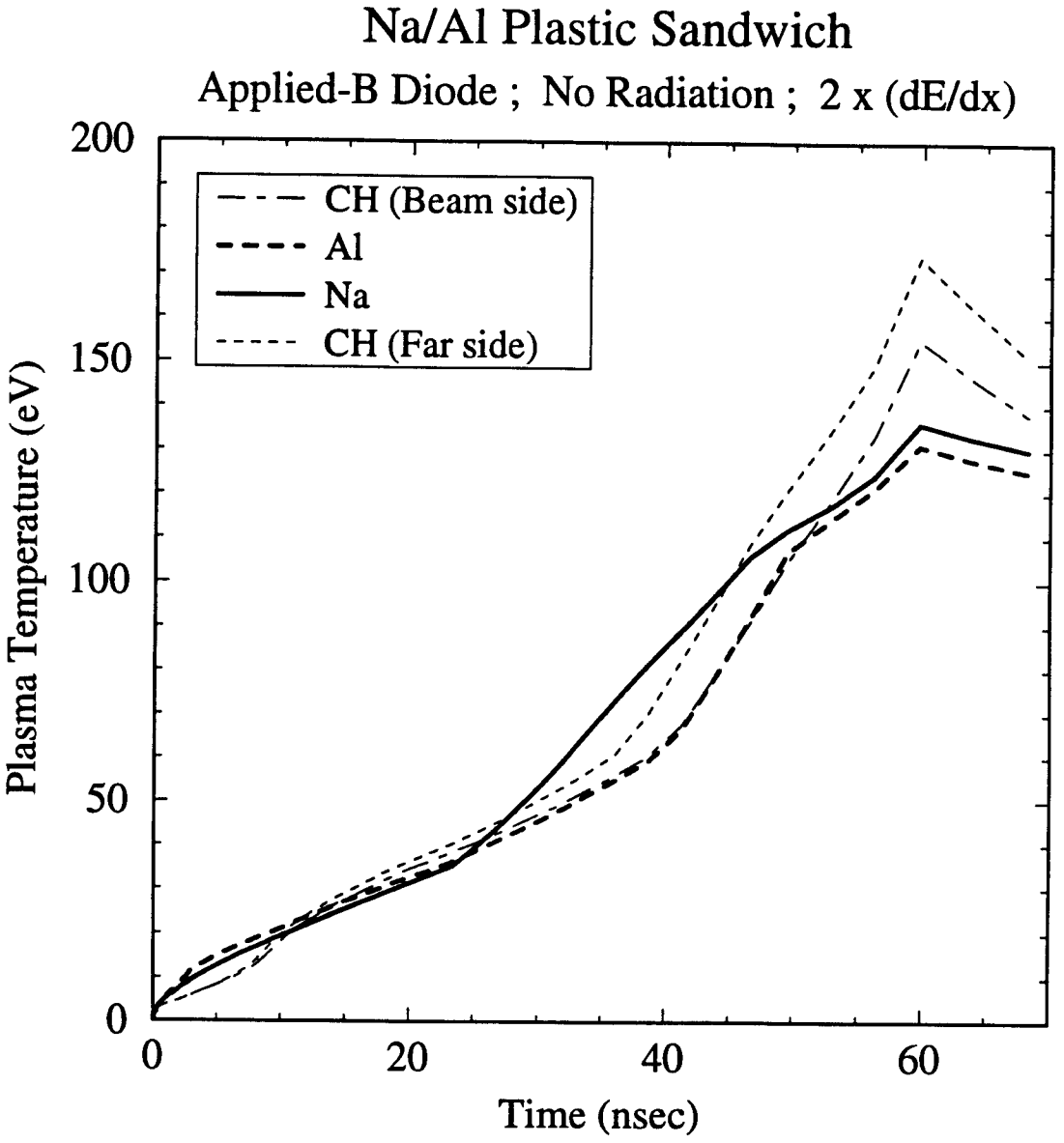

Figure 3.11. Time dependence of spatially-averaged temperatures in each target region for the applied-B diode simulation with no radiation losses and with stopping powers enhanced by a factor of 2.

3.4. Predicted Na K_α Spectra From Radiation-Hydrodynamics Simulations

Using temperature and density distributions from the radiation-hydrodynamics simulation for the upcoming B_θ diode experiment, we have computed time-dependent K_α emission and absorption spectra as well as the time-integrated emission spectrum. CRE K_α spectral calculations were performed using temperature and density distributions for Na tracer regions at 10 ns intervals. The Na plasma conditions are those from the radiation-hydrodynamics simulation shown in Figs. 3.4 and 3.6. Note that the peak spatially-averaged temperature for the Na was 21 eV, which occurred at a simulation time of 80 ns. The CRE calculations utilize the same models described in Section 2. To account for instrumental response, we assumed a spectral resolution of $E/\Delta E = 1500$.

Figures 3.12 and 3.13 show the Na K_α satellite emission and absorption spectra, respectively, at simulation times of 40, 60, and 80 ns. At 40 ns, the absorption spectrum clearly shows that F-like and O-like Na are predicted to be the dominant ionization stages. The peak K_α emission therefore comes from O-like and N-like Na — i.e., previously F-like and O-like Na, but with missing K-shell electrons. (Note that the F-like line at $\lambda = 11.9$ Å corresponds to the K_α line of "cold" Na.) At later times, the increase in temperature leads to the appearance of higher ionization stages in both the emission and absorption spectra. At the time of peak temperature (t = 80 ns), the Be-like and B-like satellites are seen strongest in emission. Figure 3.14 shows the time-integrated spectrum for the simulation. The baseline radiation-hydrodynamics simulation for the B_θ diode therefore predict Be-like satellites would be the highest ionization stage that are clearly observed.

As noted earlier, it is felt that radiation losses may be significantly overestimated in the baseline simulation. When radiation losses were neglected in the B_θ diode simulation the peak temperature rose to 27 eV. Examination of Fig. 2.10 suggests that at $n = 10^{19}$ ions/cm^3, a temperature of 27 eV should produce significant emission from the Li-like and He-like Na K_α satellites. This suggests that the shortest wavelength K_α satellites to be seen in emission in the B_θ diode experiments will be in the range of He-like to Be-like Na ($\lambda \approx 11.0$-11.3 Å).

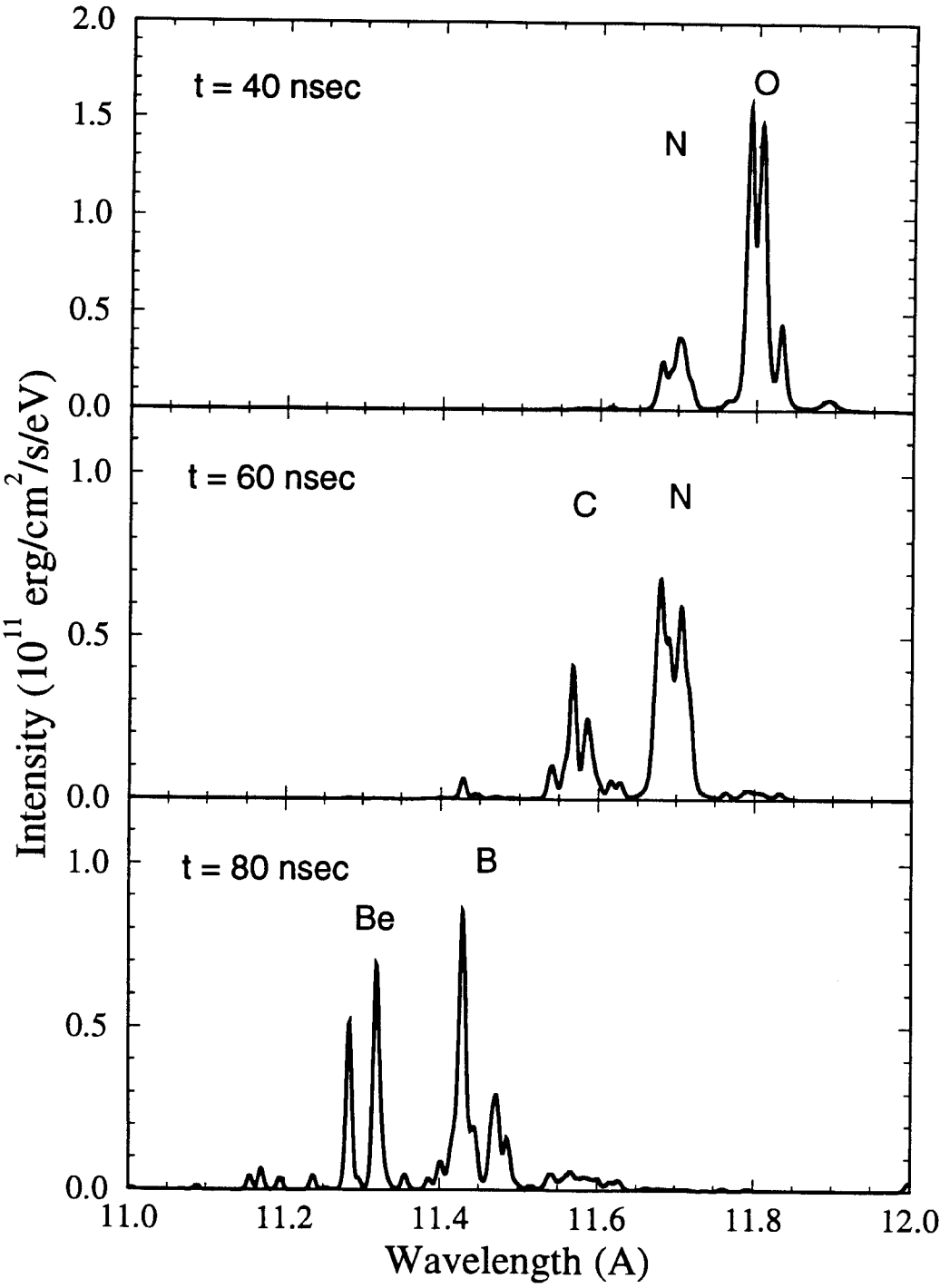

Figure 3.12. Na K_α satellite emission spectra calculated using plasma conditions at 40, 60, and 80 ns in baseline B_θ diode simulation.

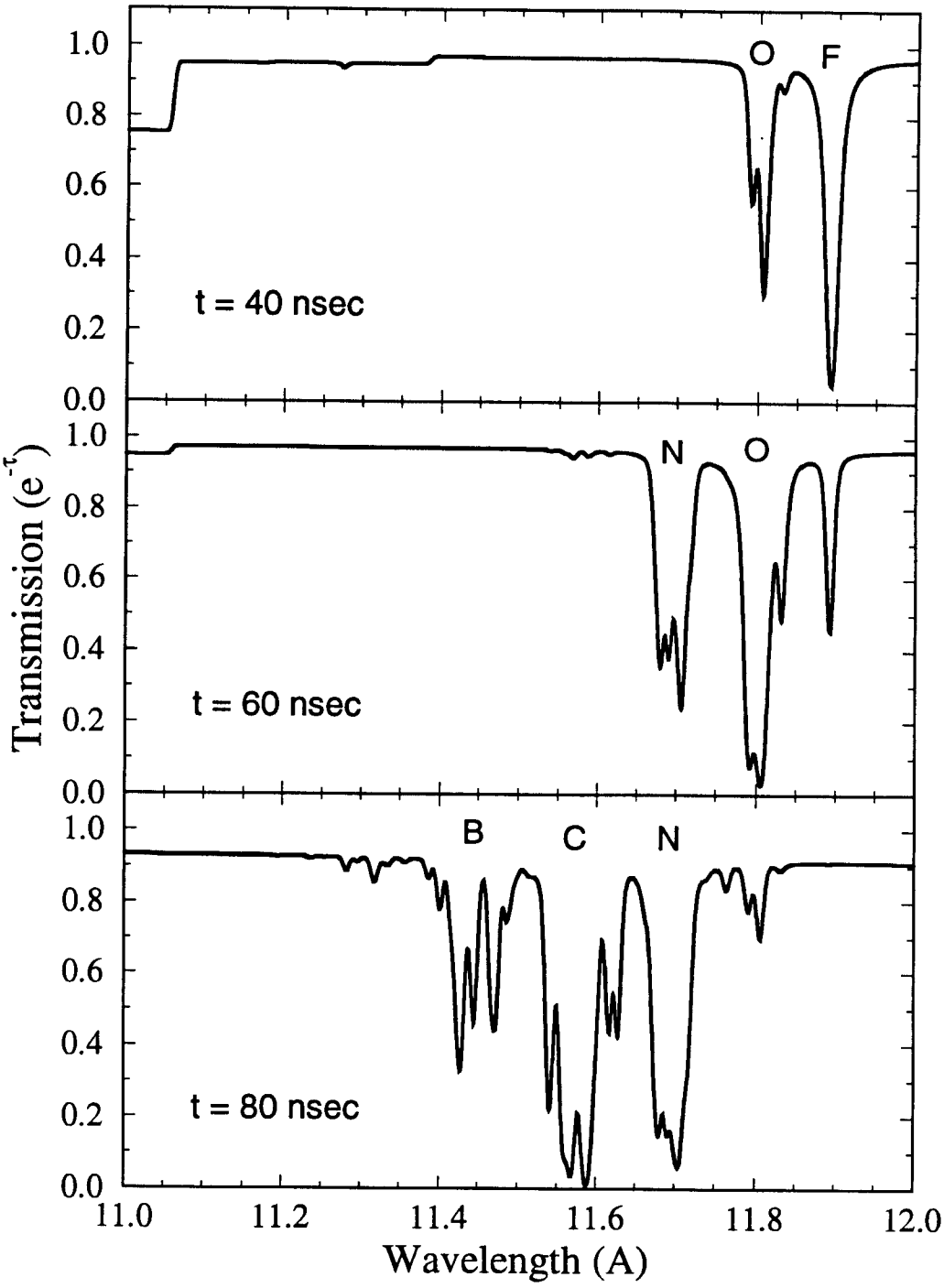

Figure 3.13. Na K_α satellite absorption spectra using same plasma conditions as in Fig. 3.12.

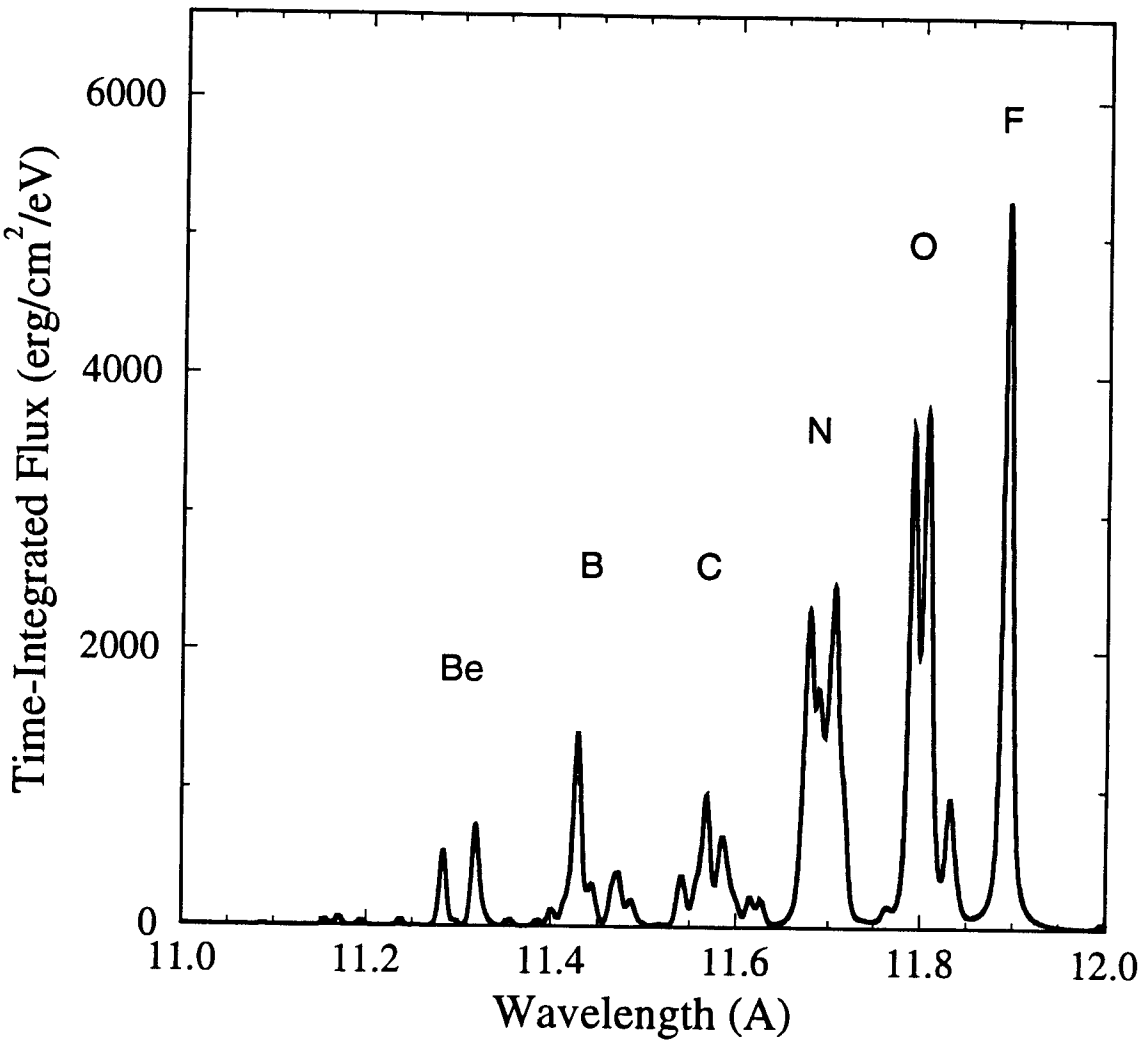

Figure 3.14. Time-integrated Na K_α emission spectrum for baseline B_θ diode simulation.

4. Upgrading and Benchmarking of Equation of State and Opacity Calculations

4.1. Introduction

Equations of state and radiative opacities are very important data for radiation-hydrodynamic simulations of high energy density plasma experiments. Unfortunately, experimental data for equations of state and opacities are very limited. To obtain these data for a wide domain of densities and temperatures, one must rely on theoretical calculations. We have developed an equation of state and opacity calculation package which can provide EOS and opacity data for a wide range of matter conditions relevant for KALIF beam-plasma interaction experiments. This package has been installed on KfK's computer systems (IBM mainframe and IBM workstation). In the past year, several significant improvements have been made for this package. This includes: (i) incorporating a "muffin-tin" model in equation of state calculations for intermediate and high density plasmas; (ii) incorporating an unresolved transition array (UTA) model in opacity calculations for high-Z plasmas; and (iii) extending atomic structure calculations by using jj coupling for high-Z systems.

In addition, we have made detailed comparisons of our EOS and opacity calculations with available experimental data and theoretical results of some of the reputable equation of state and opacity codes. In this chapter we present detailed descriptions of the model improvements and benchmark calculations.

4.2. Equations of State Modeling and Comparisons

4.2.1. Equations of State for Low Density Plasmas

At low plasma densities, EOSOPA uses a detailed configuration accounting (DCA) method; that is, it identifies atoms, ion stages, and electron configurations explicitly in the plasma, and each isolated ion in the plasma is in equilibrium with free electrons. For local thermodynamic equilibrium (LTE) plasmas, EOSOPA solves the Saha-Boltzmann equations to determine the ionization balance and the level occupation numbers. Continuum lowering and pressure ionization effects are included by using an occupation probability formalism [34] which ensures a smooth convergence of partition functions. The equations of state include contributions to the internal energy and pressure from: (i) the translations of ions and atoms, (ii) the partially degenerate electrons, (iii) configuration effects from Coulomb interaction (Debye-Hückel corrections), and (iv) atomic internal contributions (excitations and ionizations). For low-density high-temperature plasmas, an

Table 4.1. Comparison of $\bar{Z}$ Calculated from Two Equations of State and Opacity Codes

	EOSOPA	STA
H		
$\rho = 10^{-6}$ g/cm^3, $T = 1$ eV	0.076	0.077
$\rho = 10^{-6}$ g/cm^3, $T = 10$ eV	0.996	1.000
C		
$\rho = 10^{-3}$ g/cm^3, $T = 200$ eV	3.844	3.878
$\rho = 10^{-3}$ g/cm^3, $T = 100$ eV	5.967	5.977
$\rho = 10^{-1}$ g/cm^3, $T = 20$ eV	3.091	2.858
$\rho = 10^{-1}$ g/cm^3, $T = 100$ eV	5.011	5.364
$\rho = 10$ g/cm^3, $T = 20$ eV	3.874	3.032
$\rho = 10^{-6}$ g/cm^3, $T = 100$ eV	4.092	4.081
Au		
$\rho = 10^{-1}$ g/cm^3, $T = 20$ eV	6.81	7.024
$\rho = 10^{-1}$ g/cm^3, $T = 100$ eV	23.47	22.48
$\rho = 10^{-1}$ g/cm^3, $T = 500$ eV	51.89	51.72
$\rho = 10$ g/cm^3, $T = 20$ eV	5.233	6.530
$\rho = 10$ g/cm^3, $T = 100$ eV	13.81	16.99
$\rho = 10$ g/cm^3, $T = 500$ eV	39.22	38.65

ideal gas equation of state model should be reasonably good. The nonideal plasma effects can be taken into account as pertubations. Figure 4.1 shows a comparison of four different contributions to the total energy of carbon plasmas. It can be seen that nonideal effects, i.e., the Debye-Hückel corrections (long dashed curves), are very small in the low-density regime. Hence the crucial point in the calculation of equations of state for low-density and high-temperature plasmas is to calculate the ionization distribution of the plasma accurately. We have compared our calculated charge states of several different plasmas at various conditions with some reputable equation of state and opacity codes. Some of the typical results are given in Table 4.1. The agreement is satisfactory in most of the cases. Some small discrepancies appear at low temperatures and high densities. This is because continuum lowering and pressure ionization effects become important, and the treatments of this effect are different in different codes. The justification of using an occupation probability formalism to account for this effect has been discussed in a series of papers of Mihalas et al. [34].

In the cases where LTE is not valid, EOSOPA performs detailed collisional-radiative equilibrium (CRE) calculations with detailed atomic models. In the non-LTE calculations, radiation-induced transitions (e.g., photo-excitation and photoionization) are neglected. In

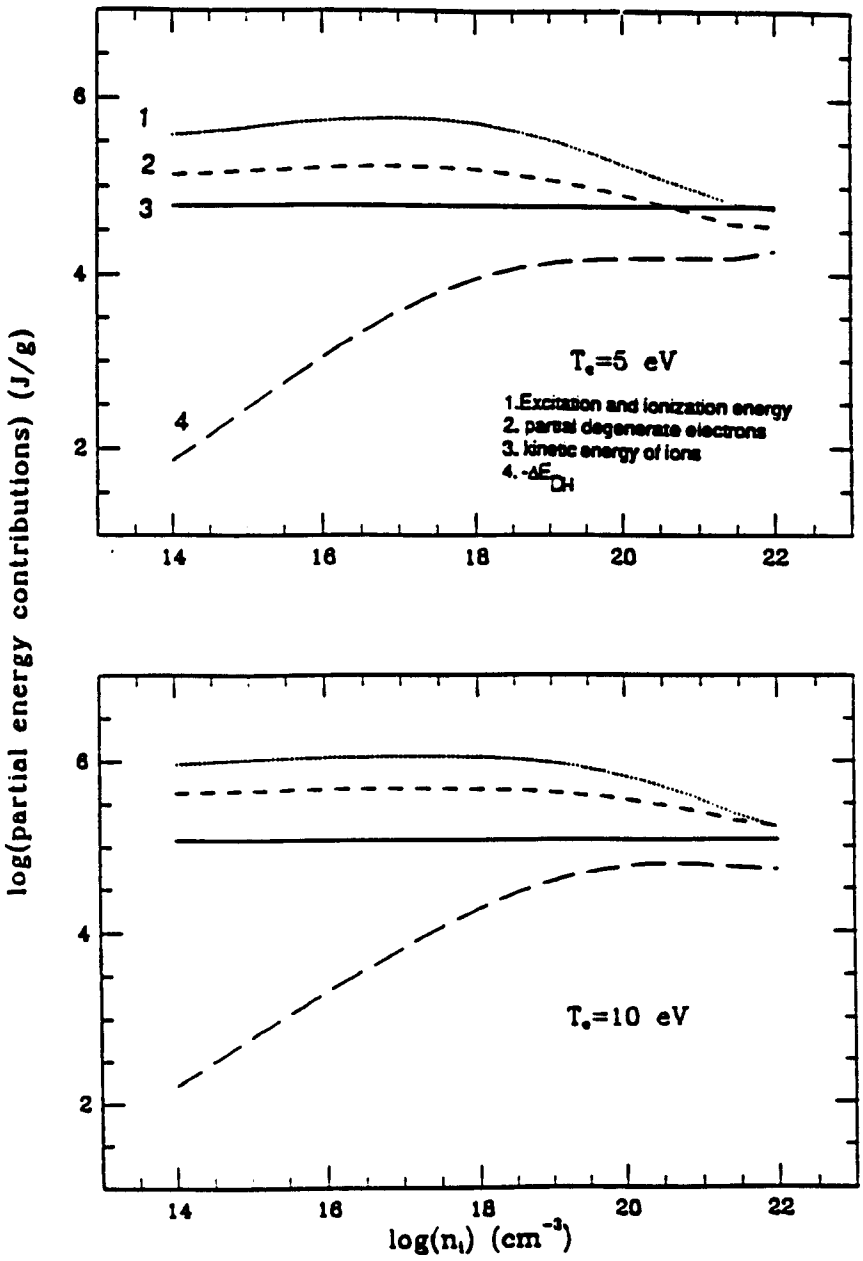

Figure 4.1. Comparison of different contributions to the internal energy of carbon plasmas at $T = 5$ eV and $T = 10$ eV.

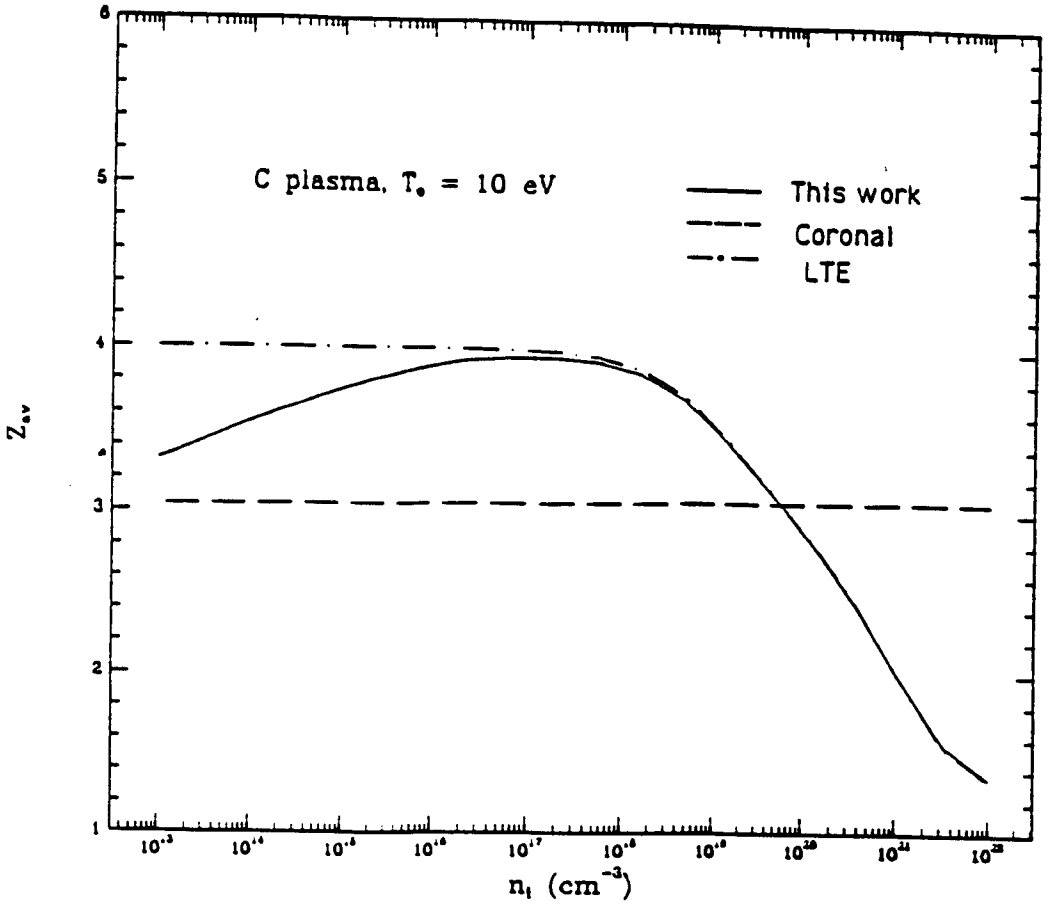

Figure 4.2. Average charge state as a function of plasma density for carbon plasma at $T = 10$ eV.

Fig. 4.2 we plot the average charge state of a carbon plasma as a function of plasma density at $T = 10$ eV. Results from three different models are shown. It can be seen that our result converges appropriately to the result of the coronal equilibrium at very low density regime, and merges smoothly to the LTE curve as density increases.

4.2.2. Equation of State for High Density Plasmas

The initial intention of developing EOSOPA was for the applications of high-temperature plasmas where the detailed configuration accounting (DCA) model is appropriate. Plasma effects on atomic systems are considered as perturbations. Since the low-temperature and high-density effects are not included in the DCA model self-consistently, the equations of state of EOSOPA previously could not provide a correct description of cohesion and the behavior of solids under compression. In the past year, we have extended our equation of state calculation to low temperature and high density plasma by using the "muffin-tin" model of Liberman [35].

The muffin-tin model improves the internal coherence of equation of state calculations for intermediate and high density plasmas. It can be generally applied to calculate electron distributions on the 0-K isotherm and for any finite temperature. It has much of the simplicity of an isolated atom but captures much of the physics of the band-structure model. Figure 4.3 illustrates the main features of the muffin-tin model. At the center of a spherical cavity is a point nucleus. Outside the cavity there is a uniform distribution of positive charge which takes the place of the surrounding ions. There are sufficient electrons in the system to give overall electrical neutrality, and the additional requirement of electrical neutrality inside the sphere is imposed. The electron density outside the sphere is replaced with its volume average in all potential energy expressions. It should be noted that in low-density cases where the spherical cavity becomes very large, this model describes an isolated atom or an ion in equilibrium with an electron gas. This is an average atom model, and the radius of the sphere is determined by matter density:

$$Ro = \sqrt{\frac{3N_{\text{ion}}}{4\pi}}\,. \tag{4.1}$$

The total energy of the system is:

$$E = K + U + V + W\,, \tag{4.2}$$

where the Dirac kinetic energy is

$$K = \sum_i n_i \int \varphi_i^*(r)(c\alpha \cdot p + \beta c^2 - c^2)\,\varphi_i\,(r)\,dr \tag{4.3}$$

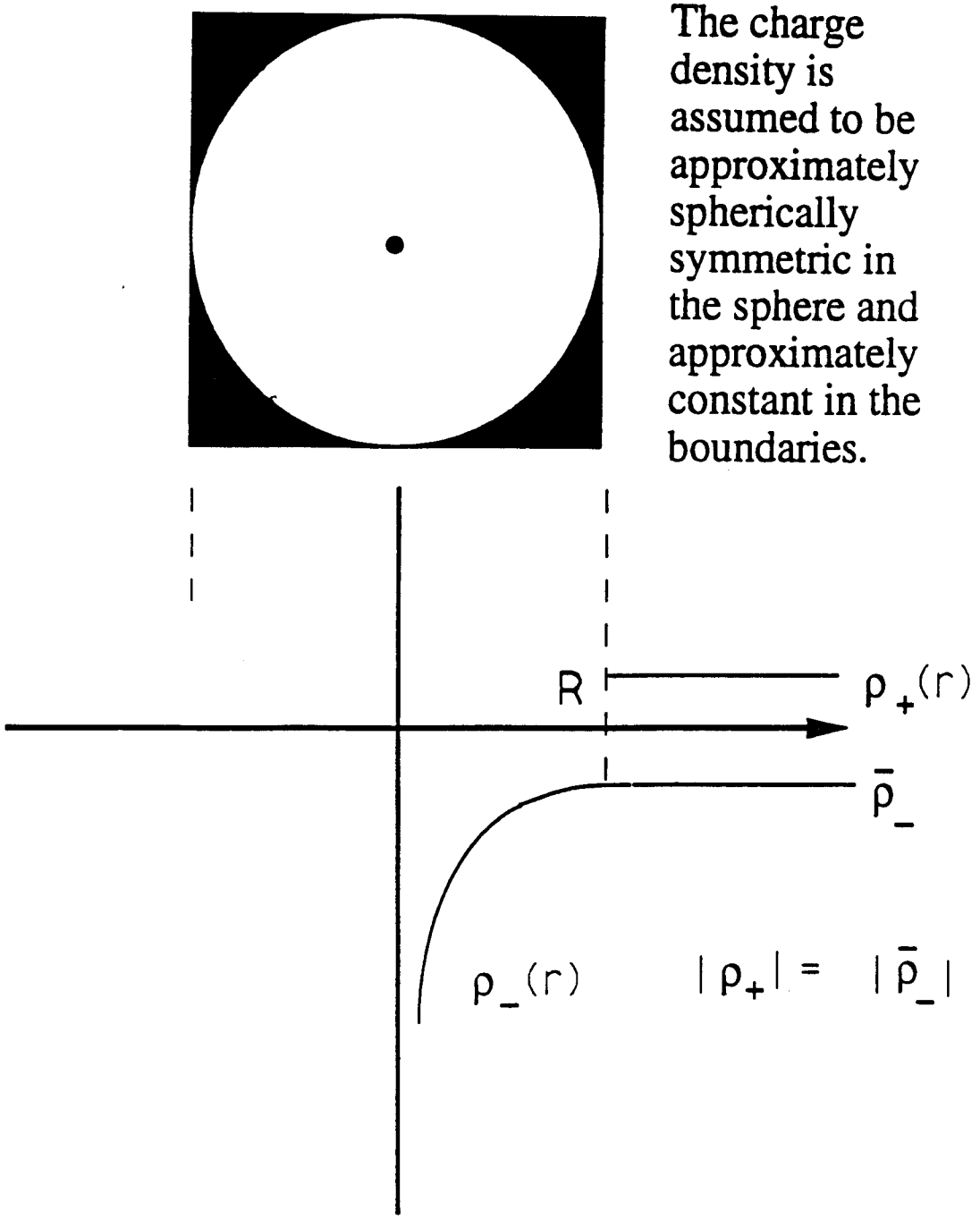

Figure 4.3. A schematic charge distribution for the "muffin-tin" model of Liberman [35].

and the potential terms are:

$$U = \int \frac{Z}{r} \left[\rho(r) - \rho_+(r)\right] dr \tag{4.4}$$

$$V = \frac{1}{2} \int\int \frac{[\rho(r) - \rho_+(r)][\rho(r') - \rho_+(r')]}{|r - r'|} \, dr \, dr \,, \tag{4.5}$$

and

$$W = \int \rho(r) \, \varepsilon_{xc}(p(r)) \, dr \,. \tag{4.6}$$

The quantity $\rho_+(r)$ is the positive charge distribution, which takes into account the average environment ion effects, and is defined as

$$\rho_+(r) = \begin{cases} 0 & r < R_0 \\ \overline{\rho} & r > R_0 \end{cases} \,, \tag{4.7}$$

and the "muffin-tinned" electron density, $\rho(r)$ is given by

$$\rho_+(r) = \begin{cases} \sum_i n_i |\varphi_i(r)|^2 & r < R_0 \\ \\ \int_{r>R_0} \sum_i n_i |\varphi_i(r)|^2 \, dr \, / \int_{r>R_0} dr & r > R_0 \,. \end{cases} \tag{4.8}$$

In the mean field approximation the entropy is

$$S = -\sum_i \left[n_i \, \log \, n_i + (1 - n_i) \, \log \left(1 - n_i\right)\right] , \tag{4.9}$$

with $n_i =$ Fermi function describing the occupation of the state i. The orbital wavefunctions $\varphi_i(r)$ can be obtained by solving the one electron Dirac equation

$$\left[c\vec{\alpha} \cdot \vec{p} + \beta c^2 - c^2 + V(r)\right] \varphi_i(\vec{r}) = \varepsilon_i \varphi_i(\vec{r}) \,, \tag{4.10}$$

where the self-consistent field potential function is

$$V(r) = -\frac{Z}{r} + \int_{r'<R_0} \frac{\rho(r')}{|\vec{r} - \vec{r}\,'|} \, d\vec{r}' - \frac{[e\pi^2 \rho(r)]^{1/3}}{\pi} - \nu \tag{4.11}$$

if $r < Ro$, and

$$V(r) = -\frac{[3\pi^2 \bar{\rho}]^{1/3}}{\pi} \tag{4.12}$$

if $r > Ro$.

For a given temperature and density, the electron distribution can be calculated self-consistently from (Eq. 4.7) – (Eq. 4.12), and the chemical potential is chosen so that

the cavity is electrically neutral. Most of the equation of state quantities are expectation values of the form

$$A_i = \int \varphi_i^*(\bar{r})\, A\, \varphi_i(\vec{r})\, d\vec{r}. \tag{4.13}$$

We take that portion of the integral within the sphere bounded by $r = R_o$ as the atomic part, and the part outside is discarded. The Helmholtz free energy F for the atomic system is

$$F = E - TS\,. \tag{4.14}$$

From this we can calculate pressure by calculating the numerical derivative:

$$P = \left.\frac{\partial F}{\partial V}\right|_T . \tag{4.15}$$

This internally consistent formulation means that the important high density plasma effects, such as pressure ionization, electron degeneracy, cohesion, and the behavior of solids under compression, etc., will be automatically included. The muffin-tin model is a natural extension of the Thomas-Fermi-Dirac (TFD) model, which itself is valid at high densities. On the other hand, this model also describes an isolated atom or an ion in equilibrium with an electron gas in low density cases. Hence the muffin-tin model smoothly connects the high-density TFD and low-density DCA models. This smooth connection provides thermodynamic consistency of calculated equations of state over a wide domain of temperatures and densities.

In Fig. 4.4, the zero-temperature isotherms based on shock wave data [35] are shown together with the pressures calculated using the muffin-tin model. It can be seen that the calculations are in good agreement with the experimental data. In this "intermediate" density regime the TFD model is poor. The corresponding TFD pressures are very much higher than the experimental data and can not conveniently be shown in Fig. 4.4.

In Fig. 4.5, we present our calculations of shock Hugoniot of aluminum and gold with experimental data [36]. The agreement is seen to be quite good. It should be noted that the comparisons shown in these figures are at pressures of a few Mbar. The self-consistent field muffin-tin model becomes more accurate at high densities. Thus, it is expected that the agreement with experimental data should be better in higher density regimes.

4.2.3. Hybrid Equation of State Model

The general method for constructing an equation of state in a wide domain of densities and temperatures consists in adding three contributions: (1) a term representing the zero-temperature isotherm, (2) a thermal electronic component, and (3) a thermal ionic

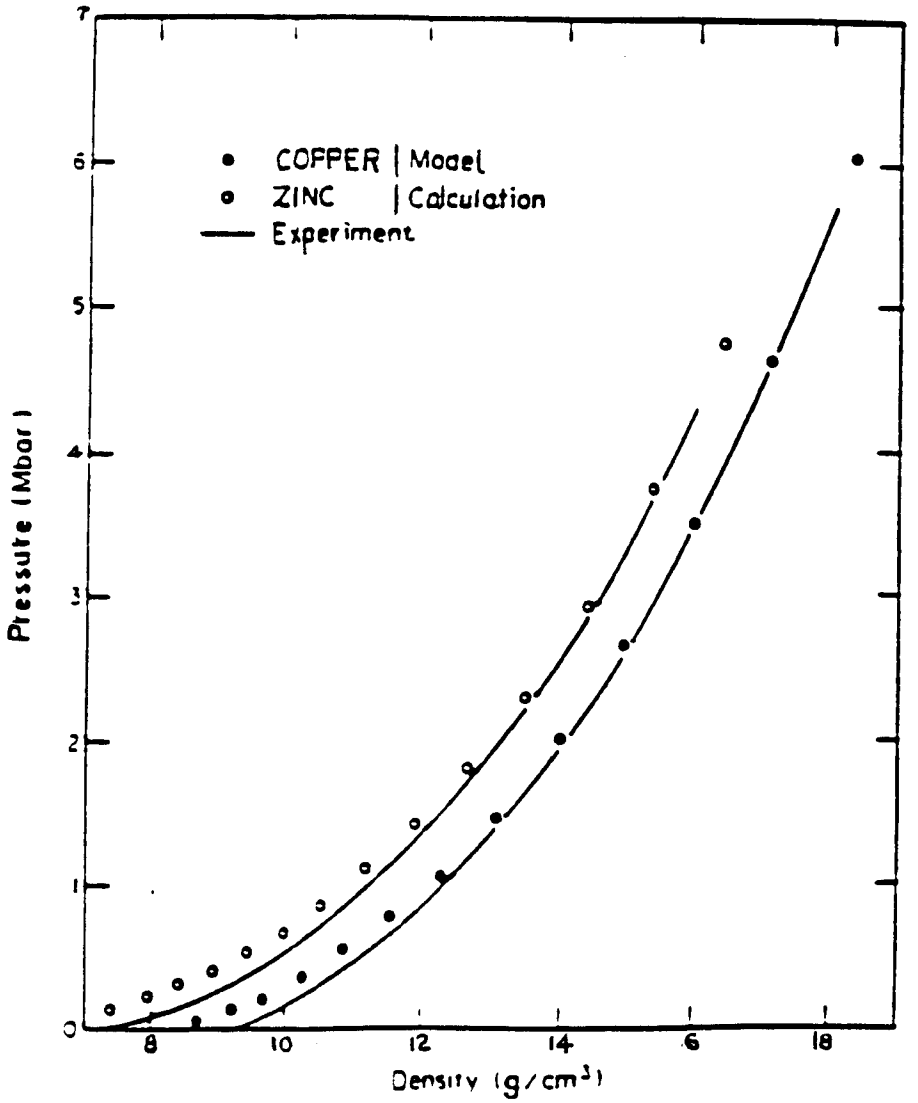

Figure 4.4. Zero temperature pressure of copper and zinc. The lines are experimental data of Altschuler, et al. from Ref. [35]. The circles are calculated values with the "muffin-tin" model. The TFD pressures are much too high to show on the graph.

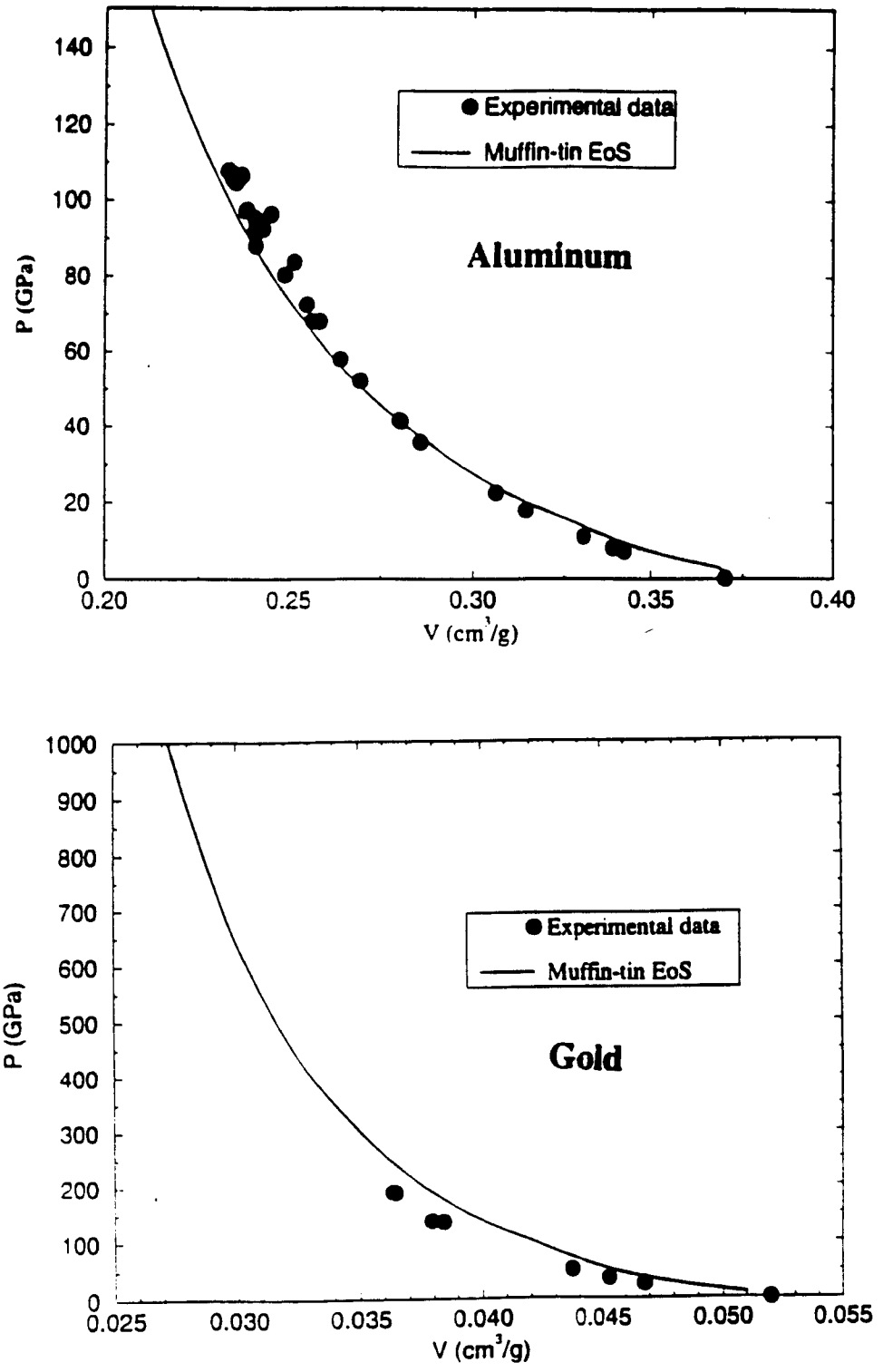

Figure 4.5. Shock Hugoniot of aluminum and gold. The lines are the calculated values with the "muffin-tin" model. The circles are experimental data.

part. Though more or less sophisticated models can be chosen for calculating these various pieces, they are in general derived independently and without intrinsic coherence. The internal incoherent equations of state can have serious drawbacks for use in hydrodynamic simulations because they are not thermodynamically consistent over the whole density and temperature domain of interest. From this consideration, we have improved EOSOPA by using a hybrid model in equation of state calculations: (1) detailed configuration accounting (DCA) model for low-density, high-temperature regime, (2) the muffin-tin model for intermediate-and high-density regime, and (3) an interpolation region where the two models are smoothly connected together.

Our hybrid model is designed to provide reliable equations of state over a wide range of temperatures and densities. First and foremost, the equations of state generated from this model are thermodynamically consistent. This has been justified by testing the energy conservation in radiation-hydrodynamic simulations. Figure 4.6 shows our results for energy and pressure isotherms of aluminum. In the low-density regime, the nonlinear behavior due to ionization/excitation is clearly seen. The cohesive, degenerate, and pressure ionization effects are observed for the high-denisty regime.

4.2.4. SESAME Equations of State: Evaluation and Comparison

The SESAME equation-of-state tables from Los Alamos National Laboratory [37] are used in many computer codes for a variety of types of simulations. They have been created using a combination of theoretical calculations and fits to experimental data. There are often several different SESAME data tables corresponding to an element. Each of these tables is useful within certain temperature and density ranges. To use the SESAME tables properly, one must understand how the tables are generated, what physics models are used, and for what class of problems each table is useful. Here, we discuss the models used to create the single set of gold SESAME tables that is available to us, and several sets for aluminum. We will also present the details of comparisons of EOSOPA and SESAME equations of state.

For aluminum, we have sets of five tables. The isotherms of total energy density and pressure from these data are plotted in Figs. 4.7 to 4.11. It is clear from these plots that the differences between different sets of data are quite significant, especially in the regime where densities are below solid.

The 3713 tables are only useful for densities above solid and for temperatures below 100 eV. These curves are designed for low temperature shock experiments in solids. The

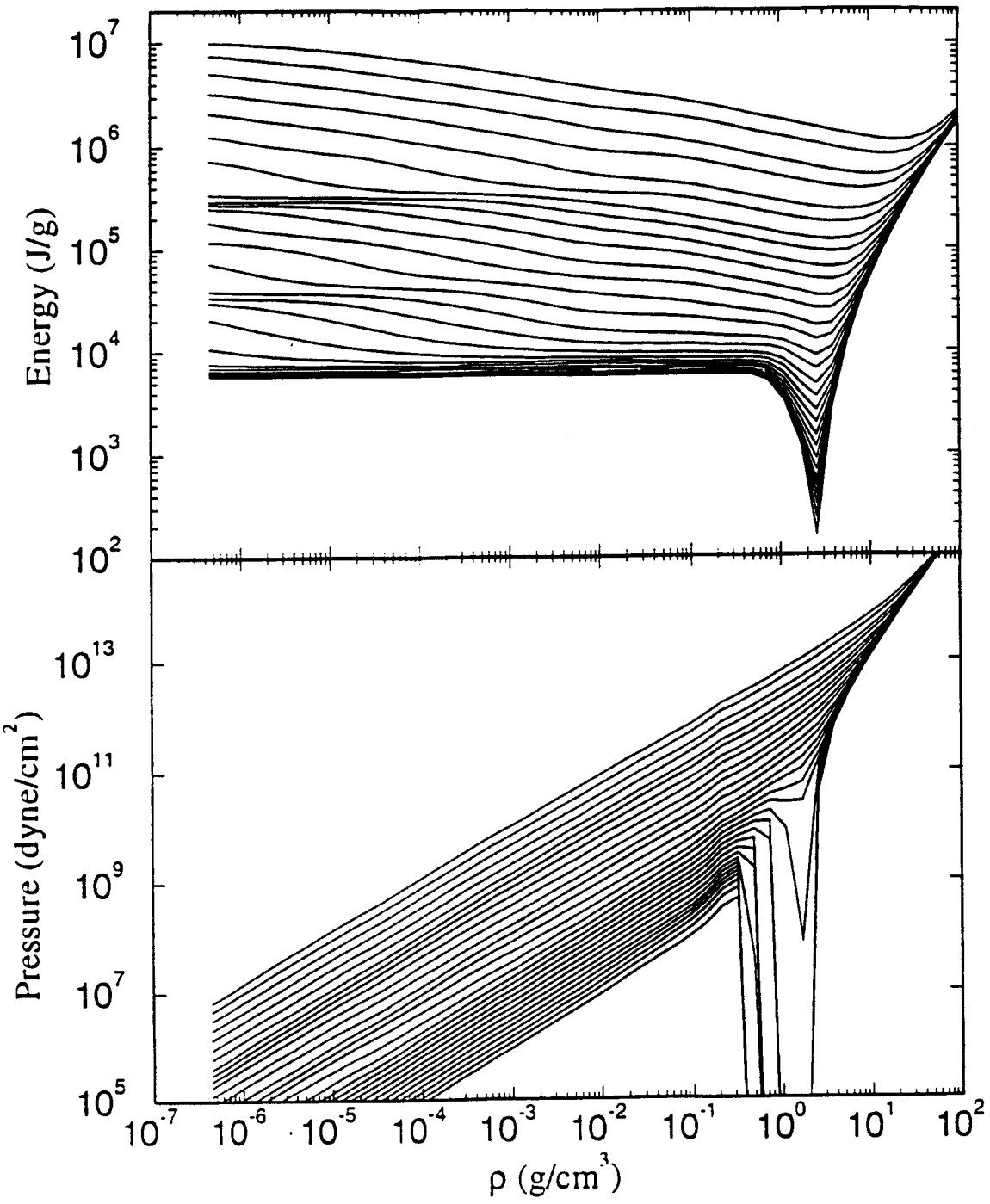

Figure 4.6. Hybrid model equations of state: isotherms of total energy density and pressure for aluminum plasma.

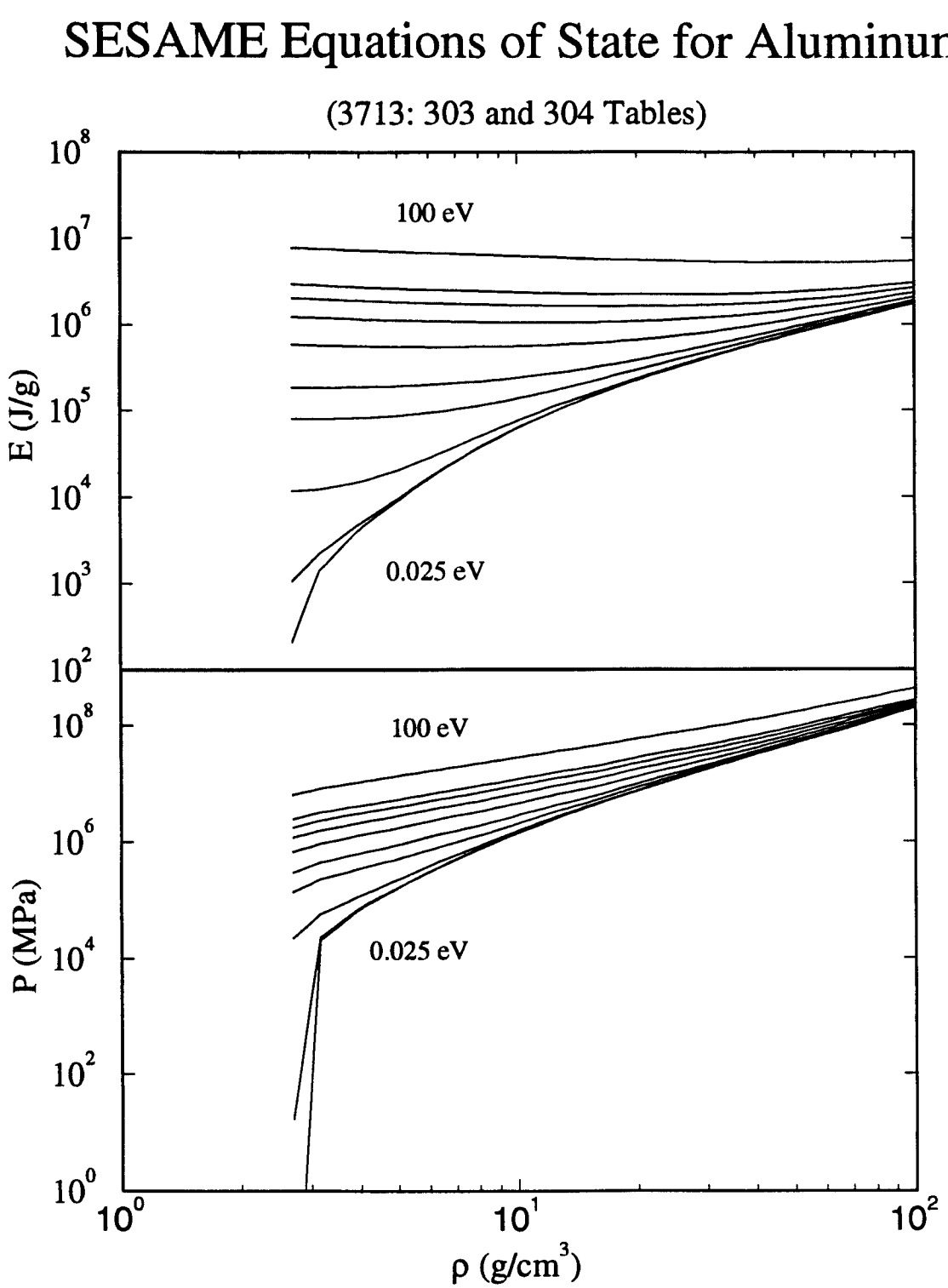

Figure 4.7. SESAME equations of state: isotherms of total energy density and pressure of aluminum. Data are taken from Table 3713.

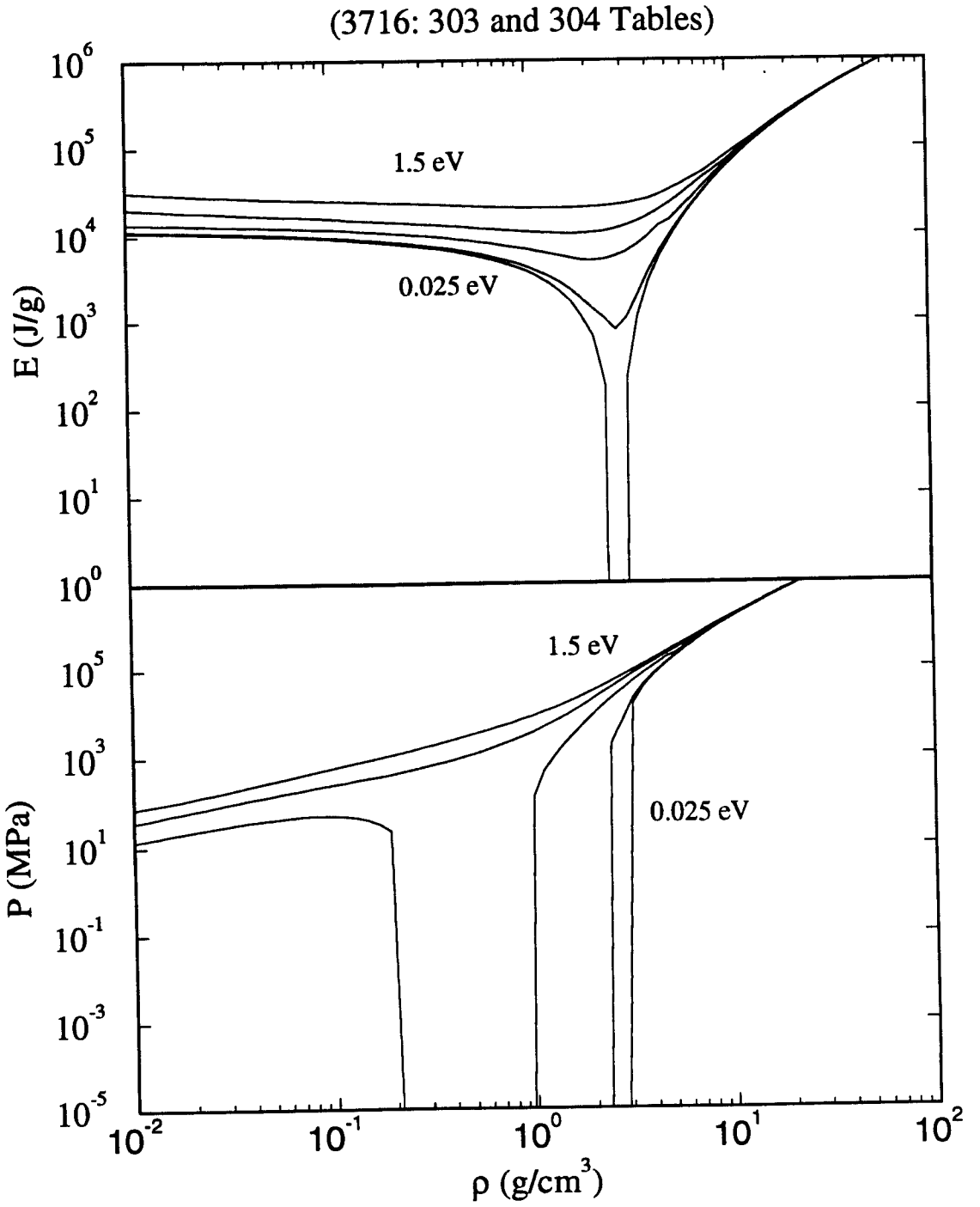

Figure 4.8. SESAME equations of state: isotherms of total energy density and pressure of aluminum. Data are taken from Table 3716.

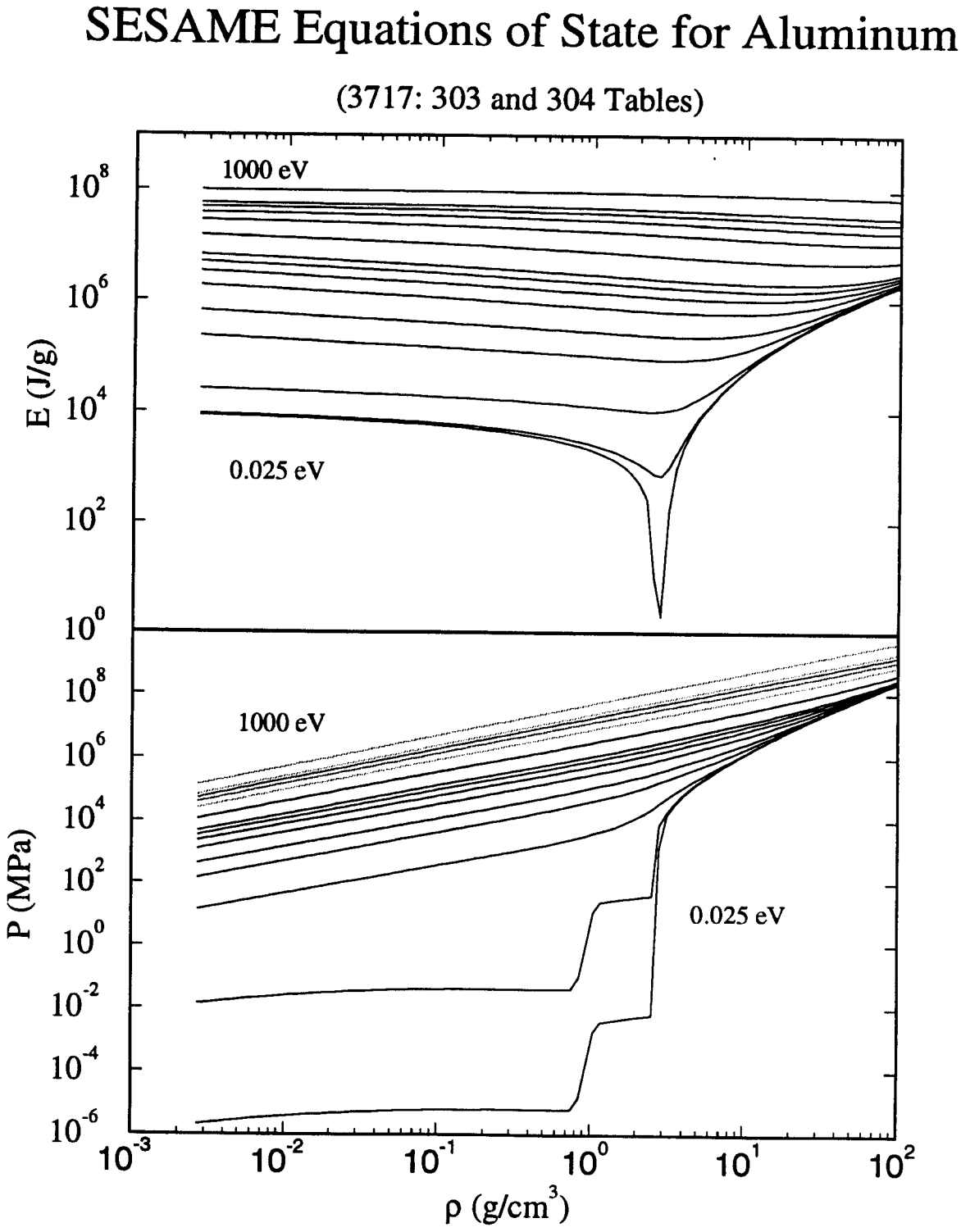

Figure 4.9. SESAME equations of state: isotherms of total energy density and pressure of aluminum. Data are taken from Table 3717.

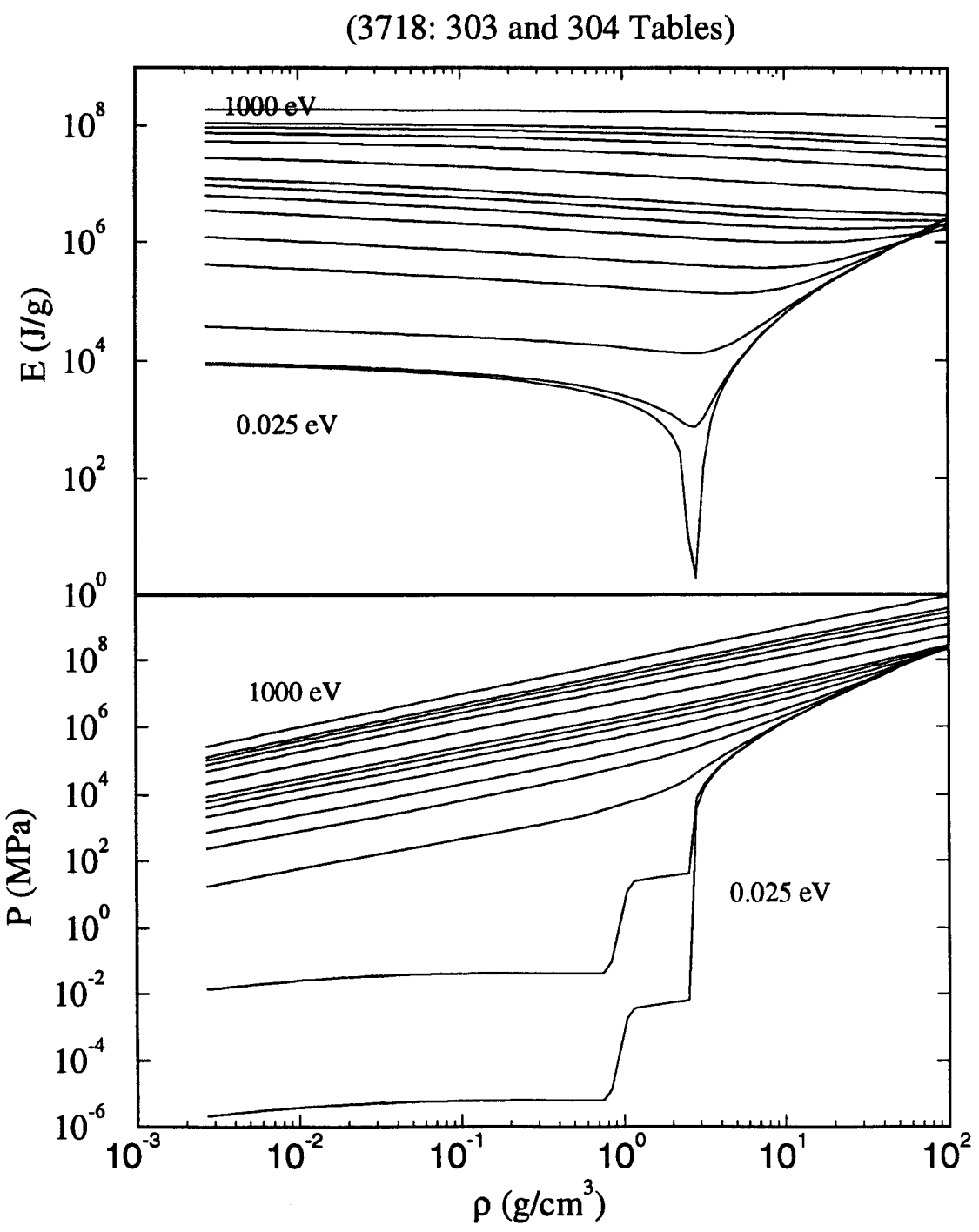

Figure 4.10. SESAME equations of state: isotherms of total energy density and pressure of aluminum. Data are taken from Table 3718.

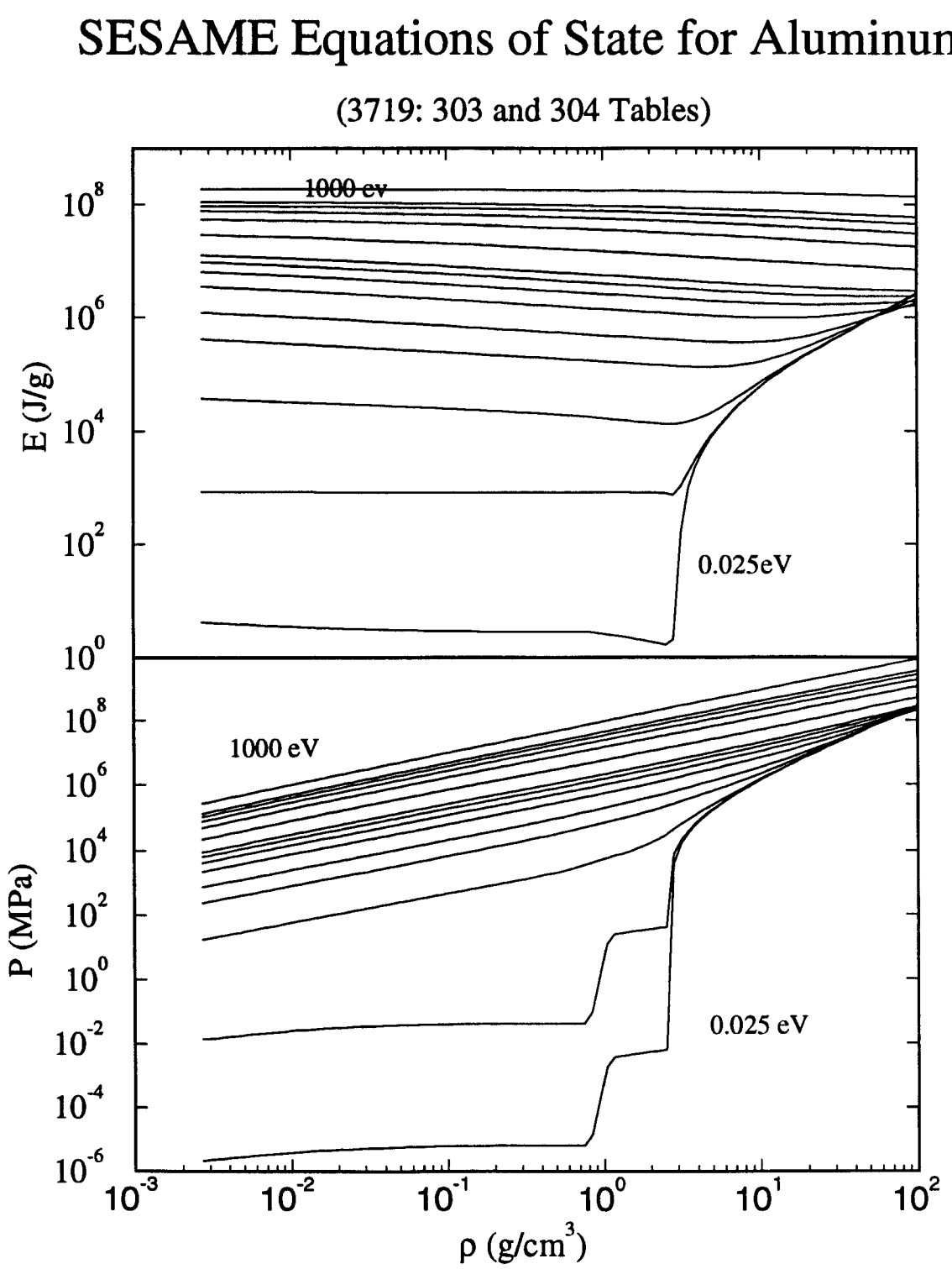

Figure 4.11. SESAME equations of state: isotherms of total energy density and pressure of aluminum. Data are taken from Table 3719.

thermal electronic contribution was calculated with the use of Augmented Plane Wave (APW) method [38]. The APW is a more general form of the Linearized Muffin Tin Orbital method, and assumes that each lattice atom is at the center of a spherical well. The nuclear thermal contributions are calculated with the Grüneisen model. Figures 4.12 and 4.13 present the comparisons of EOSOPA equations of state and the data in 3713 tables. The dotted lines are particular isotherms of our calculation with the use of EOSOPA. In this high density regime, the agreement of EOSOPA and SESAME equations of state is reasonably good. At low temperature and intermediate density regime, our calculated pressures are about 10 to 20 percent lower than the SESAME data.

The 3716 tables for aluminum are advertised as being valid from 0.001 to 1000 g/cc, and from room temperature to 1.6 eV. The cold isotherms are calculated with the APW band structure method. The thermal electron contribution is calculated based on Thomas-Fermi-Kirzhnits theory. Nuclear contributions are calculated with a Grüneisen model. Liquid and gas region calculations use a soft sphere model [39]. Most of the table's mesh is below 0.1 eV and from 0.4 g/cc to 5 g/cc. The low temperature part of the table agrees well with experimental Hugoniots. The comparison of EOSOPA with the data in Table 3716 is shown in Fig. 4.14. In this low temperature regime, there are some significant discrepancies between the EOSOPA and SESAME equations of state. Especially at room temperature, our calculated energy minimum is not at the solid density. These discrepancies could be due to the approximation of average environment around an atomic sphere in the 'muffin-tin' model. In this temperature and density regime, the effects of ion-ion interactions should be accounted for more accurately, and the average description is not adequate. Further improvement in this direction is under consideration.

Of the available aluminum table sets, 3717, 3718, and 3719, which are very similar to each other, are valid over the broadest range. As shown in Figs. 4.9 to 4.11, they have approximately the expected behavior in energy density. However, at low temperatures and low densities, the pressure isotherms are not correct because they are inconsistent with the corresponding energies. Comparing our calculated results, which are shown in Fig. 4.6, with the data of 3717, 3718, and 3719 tables, it is clear that the overall consistency of our calculated results are better. On the other hand, *it should be noted that the detailed nonlinear effect of ionization/recombination equilibrium in low density, high temperature regime, which is clearly seen in EOSOPA's isotherms, is not shown in the SESAME data.* In the relatively high density regime, the overall agreement of EOSOPA and SESAME equations of state is reasonably good.

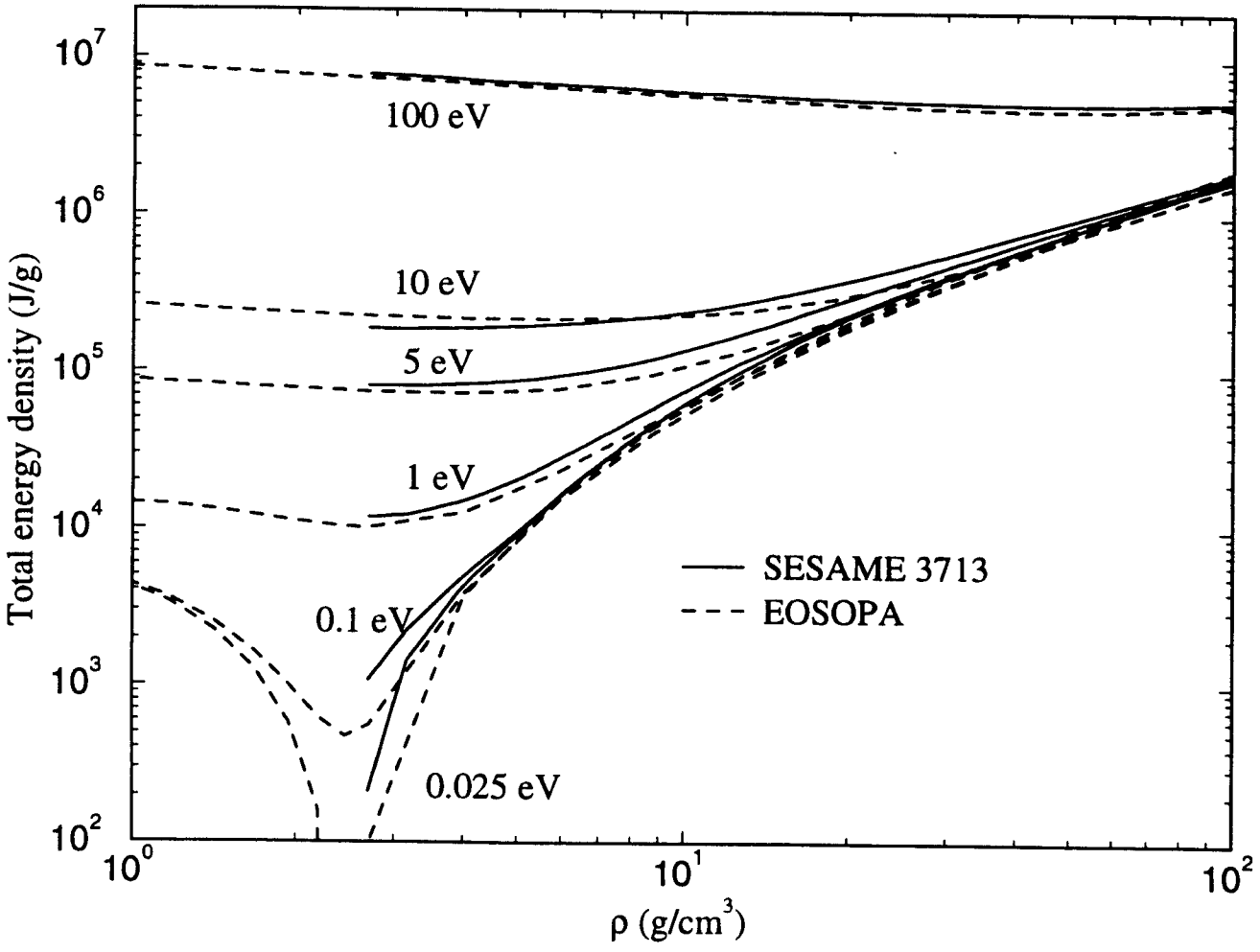

Figure 4.12. Comparison of EOSOPA and SESAME equations of state: isotherms of total energy density of aluminum.

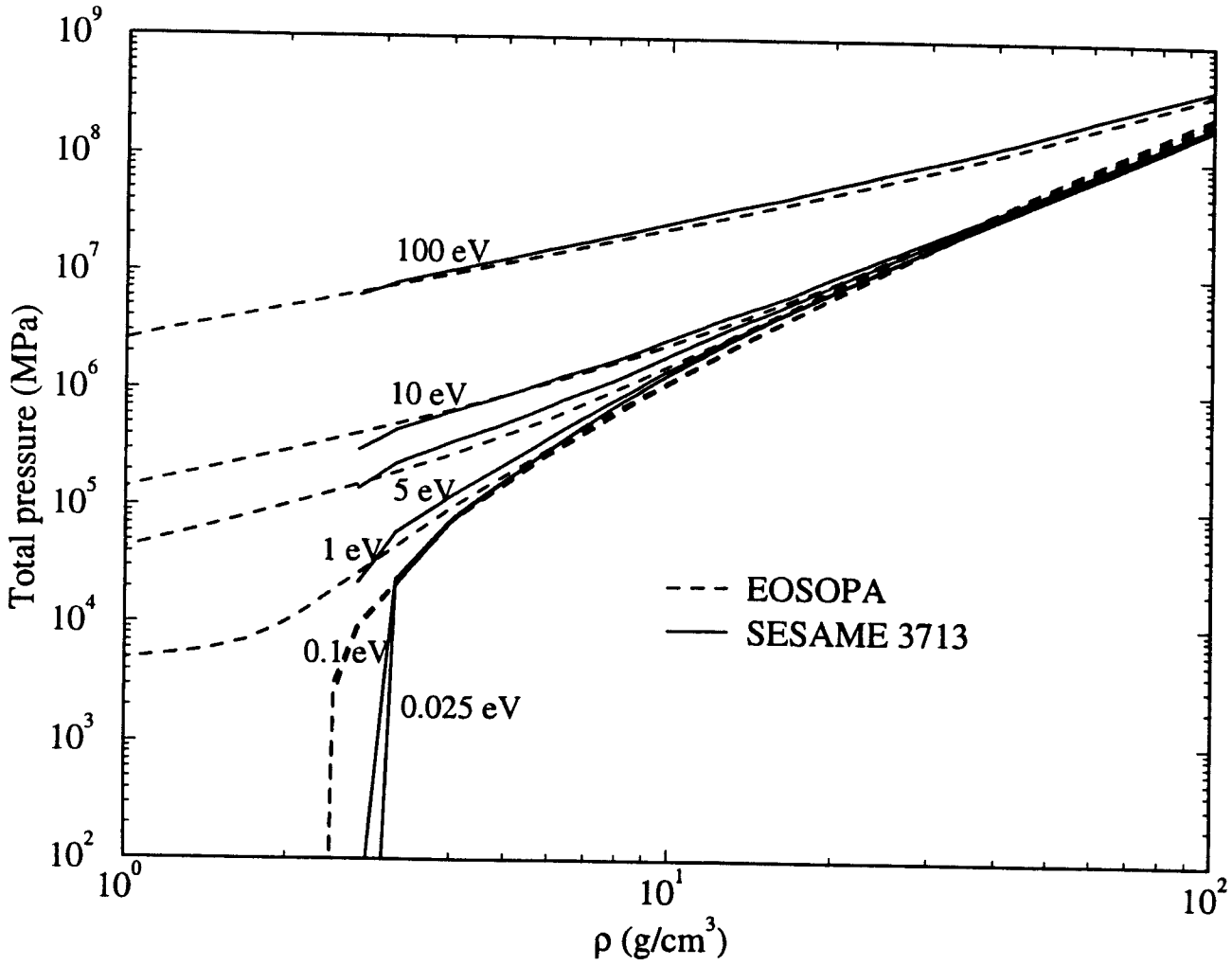

Figure 4.13. Comparison of EOSOPA and SESAME equations of state: isotherms of total pressure of aluminum.

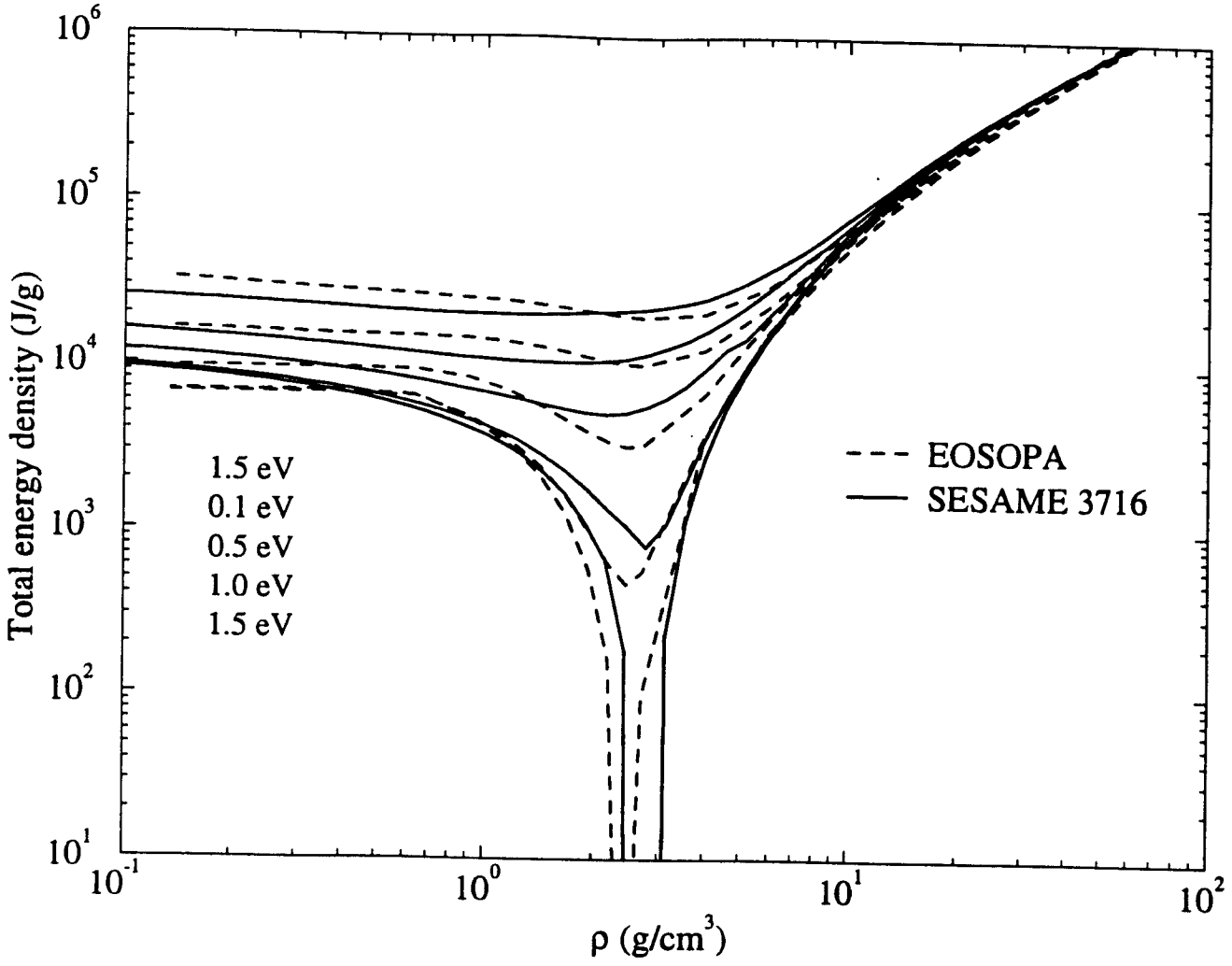

Figure 4.14. Comparison of EOSOPA and SESAME equations of state: isotherms of total energy density of Al.

The gold 2700 set of tables is the oldest of the those reported here (generated in January 1976). The electronic contribution at high density was calculated with Thomas-Fermi-Dirac theory. The cold curve is based on a modified Morse model. The nuclear contribution is calculated with a Grüneisen and Debye model. The comparisons of EOSOPA's result and this set of SESAME data are presented in Figs. 4.15 and 4.16. It can be seen from the figures that the agreement is very good in the high density and high temperature regime. Significant discrepancies appear in the low temperature, low density regime. We believe that the arbitrary constant extension of energy density in SESAME's 2700 tables is not correct.

In conclusion, the EOSOPA's equations of state are in general in reasonably good agreement with SESAME data in the temperature and density regime where SESAME data are believed to be valid. Some discrepancies are found in the regime around solid densities and low temperatures. The SESAME equations of state may be very accurate in some specific regime, but these tables could have certain painful drawbacks for use in hydrodynamic simulations because different tables are not smoothly connected. In this respect the EOSOPA's equations of state seem to have better overall thermodynamic consistency. In addition, the detailed excitation and ionization effects, which are very important in high temperature and low density regimes, are taken into account with the use of a DCA model in EOSOPA. However, these important effects are not properly accounted for in many of the SESAME EOS tables. For the plasma conditions relevant for KALIF high energy density plasma experiments, the ionization and excitation effects can have significant contributions to the equations of state, and must be included properly.

4.3. Opacity Modeling and Comparisons

In order to be able to properly treat the transfer of radiation in plasma, it is necessary to have values of the opacity over a wide range of conditions. In our model, radiation is absorbed by atoms and ions via the following types of process:

1. bound-bound transitions (line absorption);
2. bound-free transitions (photoionization);
3. free-free transitions (bremsstrahlung);
4. scattering of photon by electrons.

In principle the calculations of opacity for low-Z and high-Z systems are the same. In practice, however, the detail treatments are very different. We use the detailed term

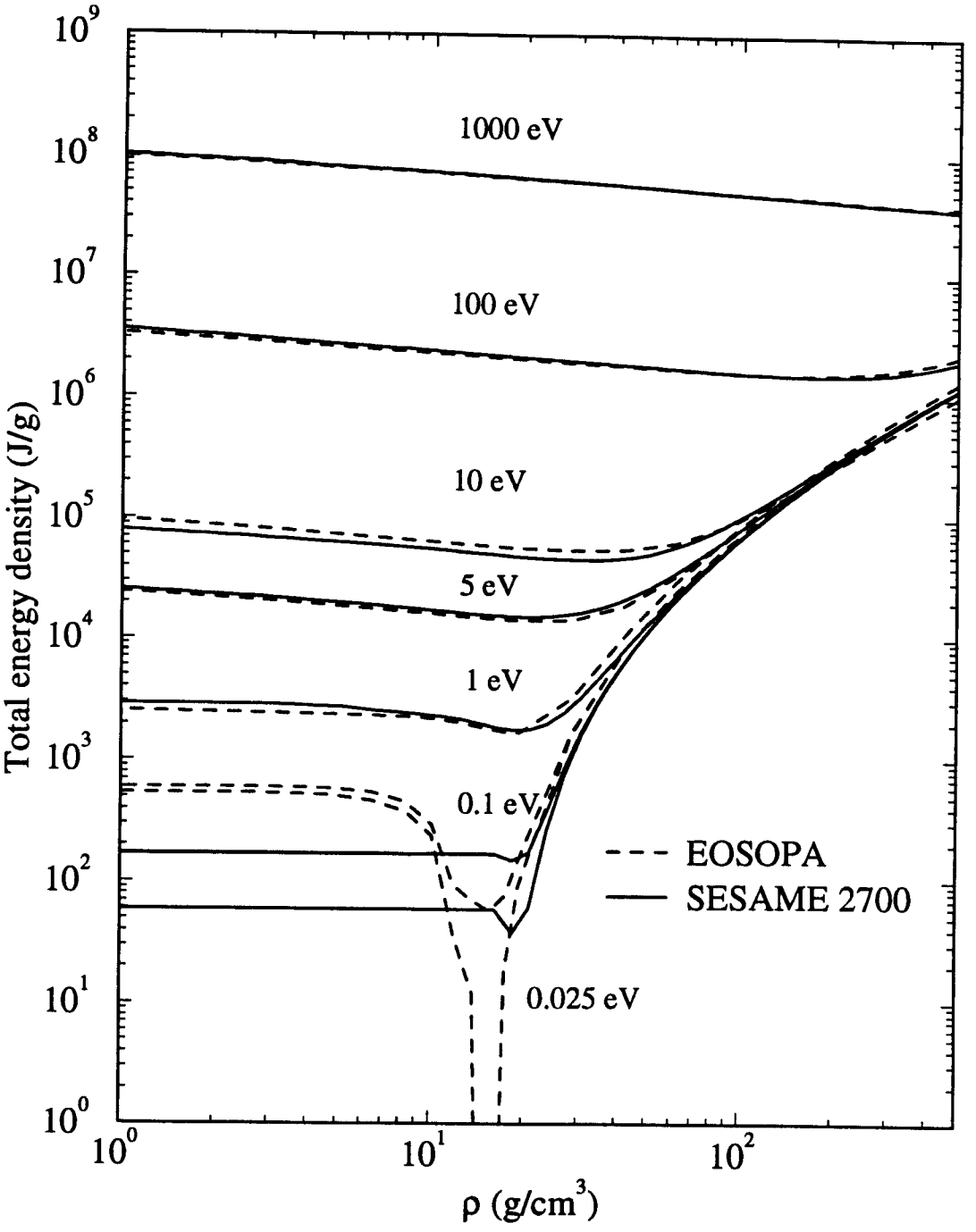

Figure 4.15. Comparison of EOSOPA and SESAME equations of state: isotherms of total energy density of gold.

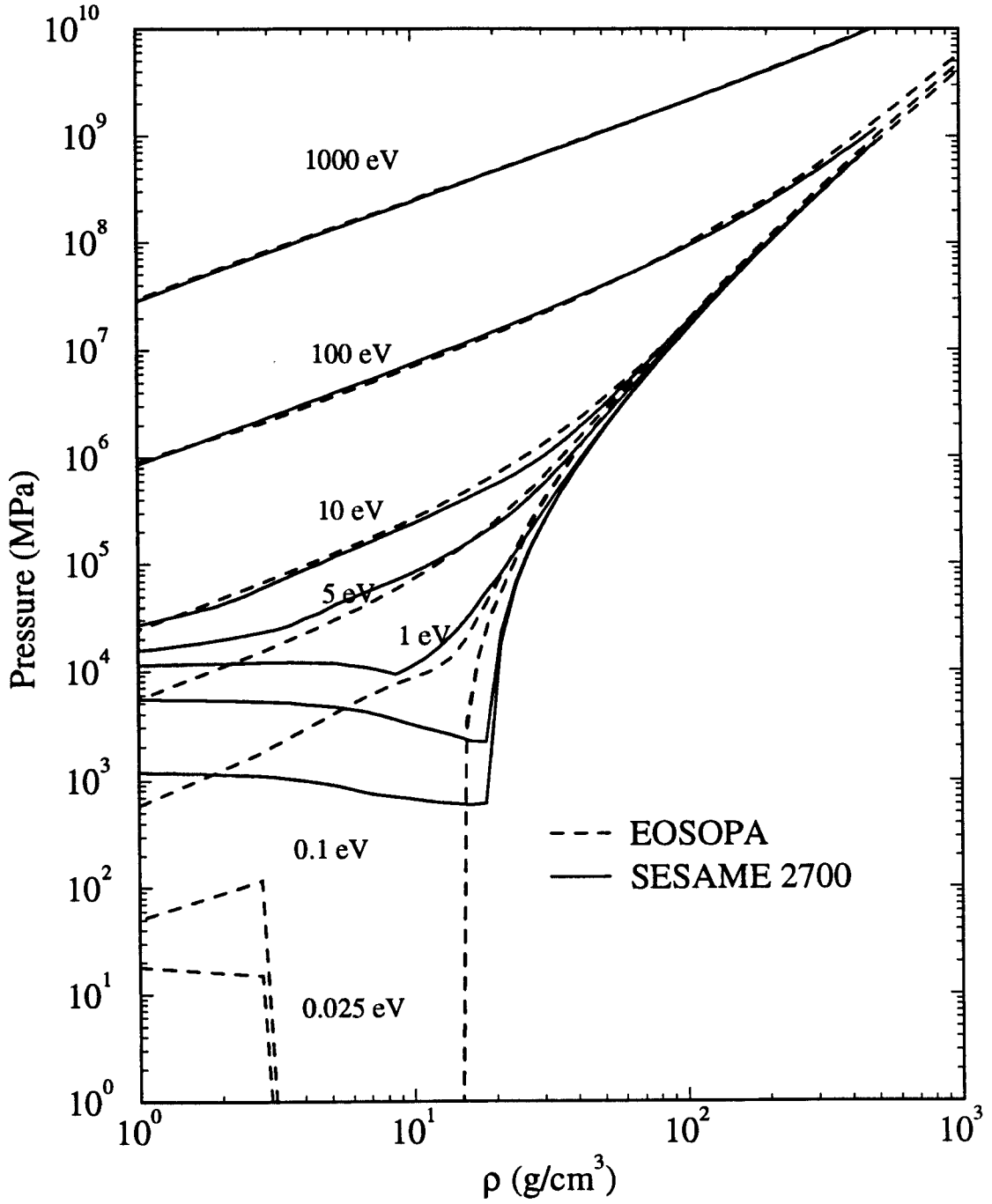

Figure 4.16. Comparison of EOSOPA and SESAME equations of state: isotherms of total pressure of gold.

accounting (DTA) method for low-Z systems, and use an unresolved transition array (UTA) model for high-Z systems.

4.3.1. Opacity Calculations for Low-Z Plasmas

For low-Z atomic systems, the bound-bound transitions are calculated for all subshells in each configuration of various ion stages explicitly. The line spectrum is treated in full intermediate coupling; i.e., including fine-structure. The line shapes are Voigt profiles with Gaussian widths given by Doppler broadening and Lorentz widths given by natural and electron impact broadening.

We compute the opacity and emissivity in the framework of the chemical picture with occupation probabilities. As in all of statistical physics, we rely heavily on the one-to-one relation between "availability" of states (statistical weight of level i) and "occupation" of those states (atoms actually in level i). Due to the perturbations of close neighbors, the availability of the bound level i may not be 1 but some fractional number w_i. Hence, as density increases, some spectrum lines will disappear because of the destruction of corresponding excited levels. This effect has been taken into account in our opacity calculations. In Fig. 4.17 we present our calculations of absorption coefficient for carbon plasmas at various densities. It can be seen that some spectral lines disappear as the density increases. These lines correspond to transitions involving excited levels with very low availabilities in high density cases. Figure 4.18 shows results from MINSK's calculations for the same conditions. It is suspected that the continuum lowering model used in MINSK's code may be more sensitive to density than the one we use. Note that in the MINSK calculations fewer lines are seen at relatively low photon energies in the lower density cases. It is not clear why this occurs.

We have made a series of comparisons with available MINSK opacity data for beryllium and carbon. Detailed results are ploted in Fig. 4.19 through Fig. 4.34. Generally speaking, the overall agreement is reasonably good, particularly in regard to continuum levels. However, our EOSOPA calculations tend to provide a more detailed line structure. There are some discrepancies in ionization distributions, as can be seen, for instance, in the bound-free absorption for C at $T = 1$ eV and $n = 10^{16}$ cm^{-3} (Fig. 4.27). Since the procedures for calculating opacities for low-Z plasmas are quite standard, we believe that the following could be the most likely reasons for discrepancies between the two codes:

- differences in raw atomic data (energy levels, oscillator strengths, photoionization cross sections, collisional rate coefficients);

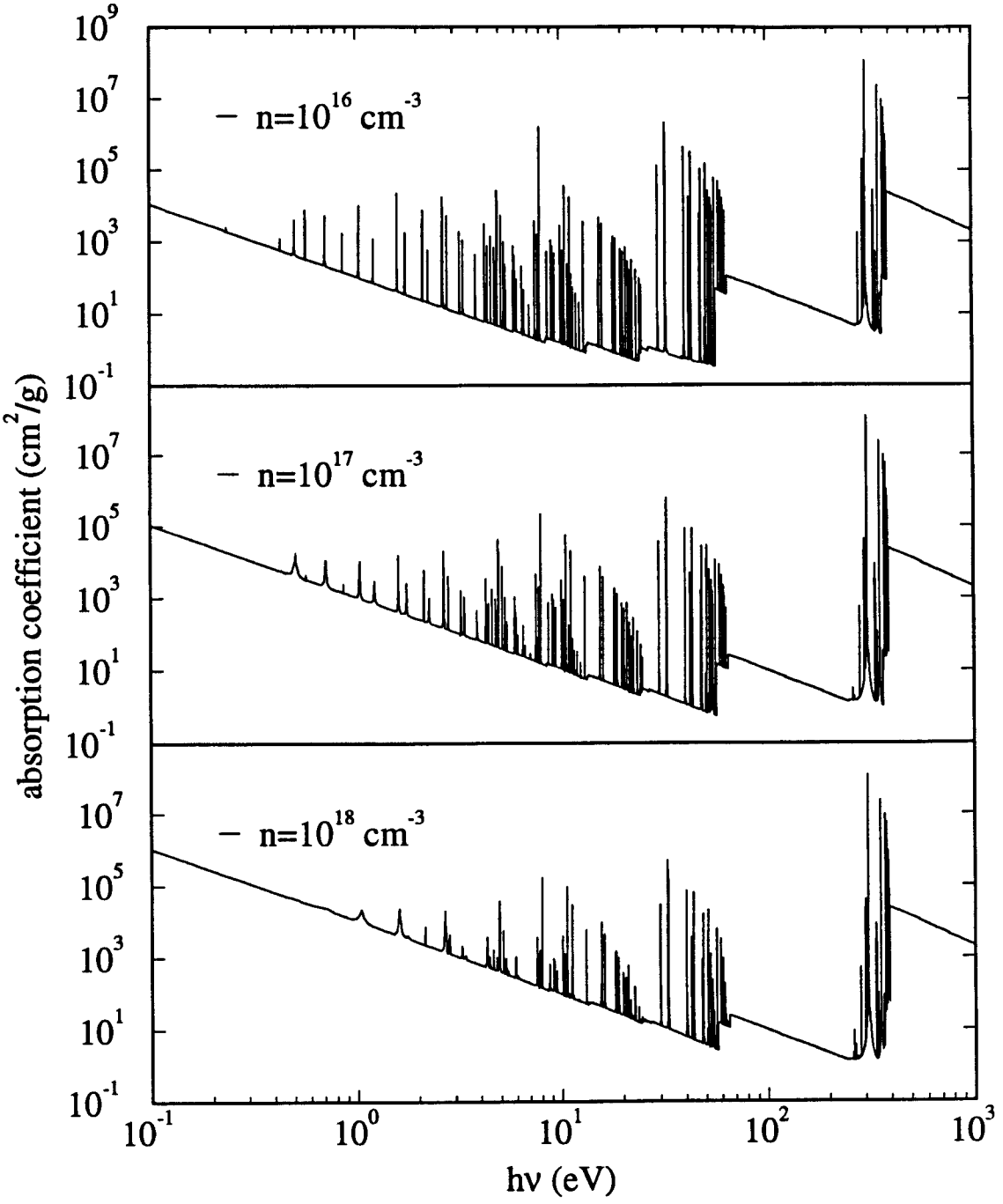

Figure 4.17. EOSOPA's result: absorption coefficient of carbon plasma as a function of plasma density.

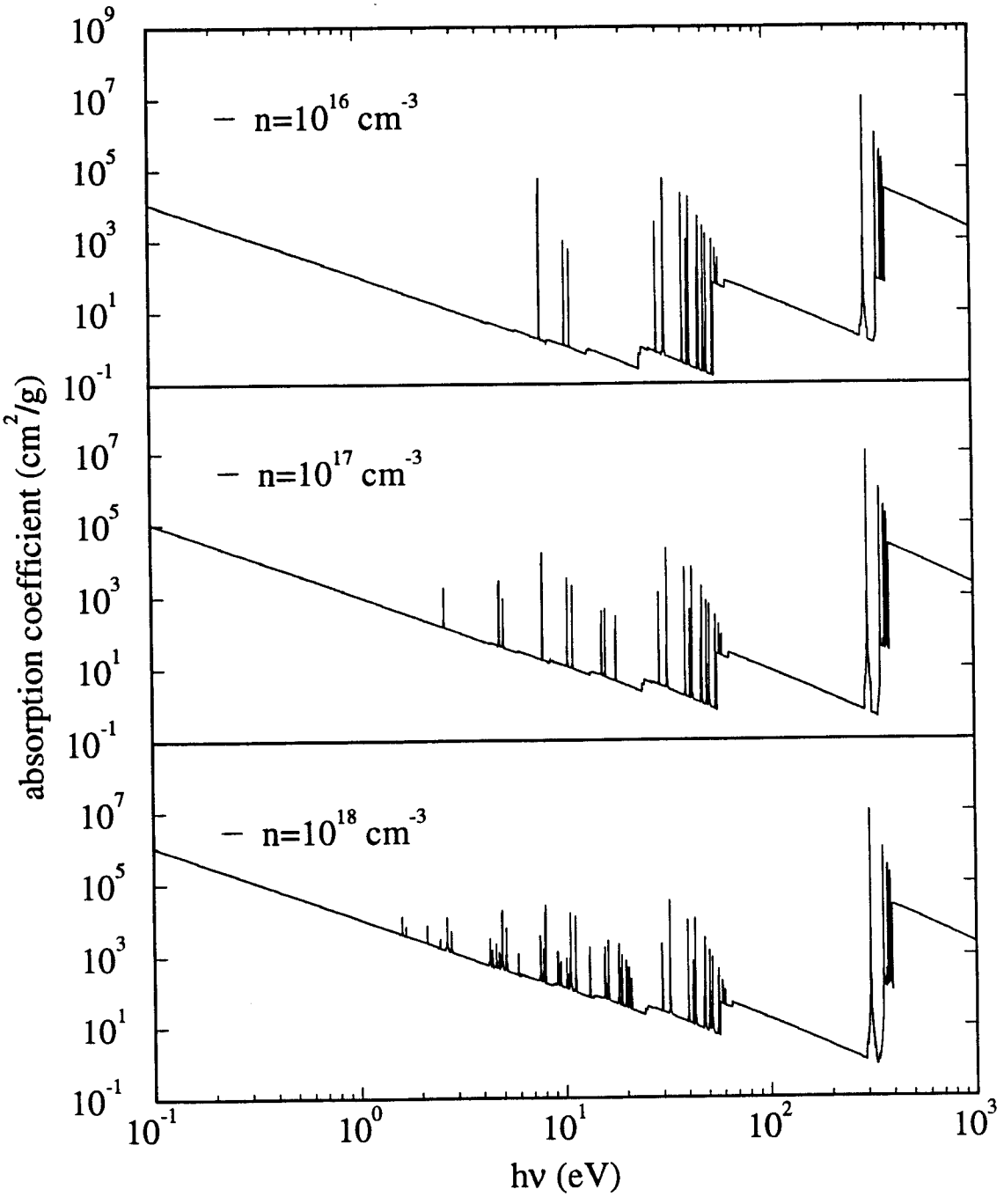

Figure 4.18. MINSK's result: absorption coefficient of carbon plasma as a function of plasma density.

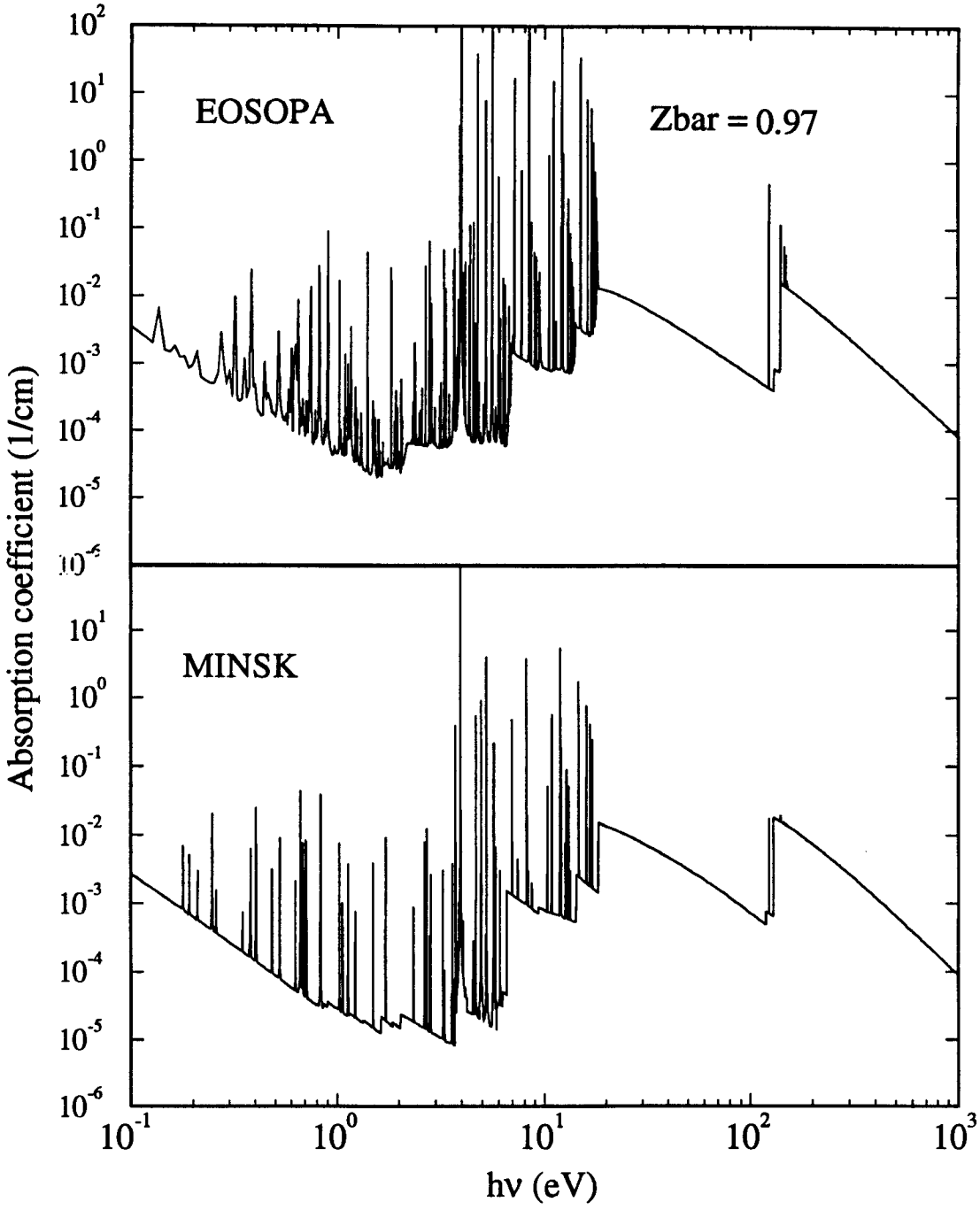

Figure 4.19. Opacity comparison: absorption coefficient of beryllium plasma at $n = 10^{16}$ cm^{-3}, $T = 1$ eV.

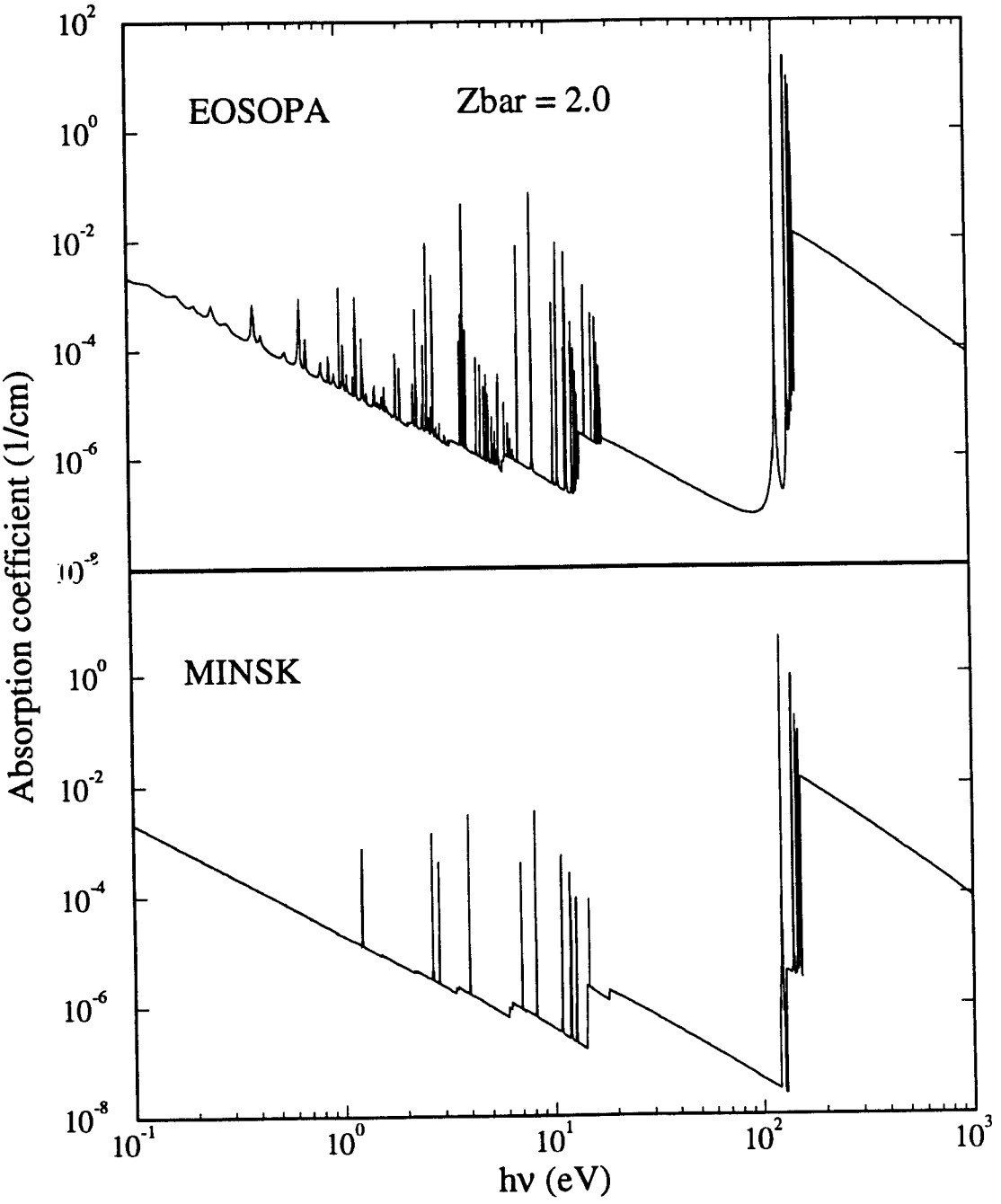

Figure 4.20. Opacity comparison: absorption coefficient of beryllium plasma at $n = 10^{16}$ cm^{-3}, $T = 5$ eV.

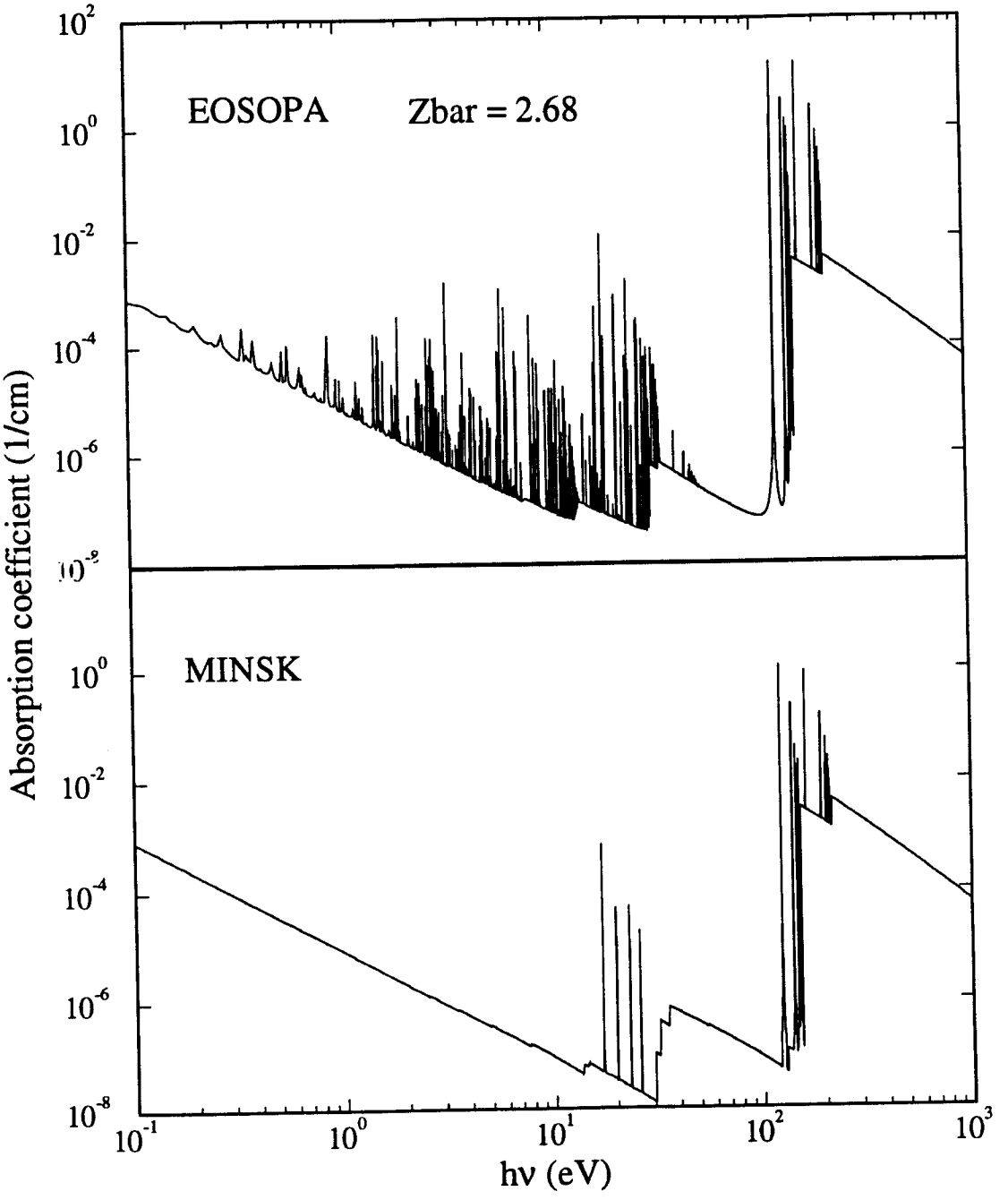

Figure 4.21. Opacity comparison: absorption coefficient of beryllium plasma at $n = 10^{16}$ cm^{-3}, $T = 20$ eV.

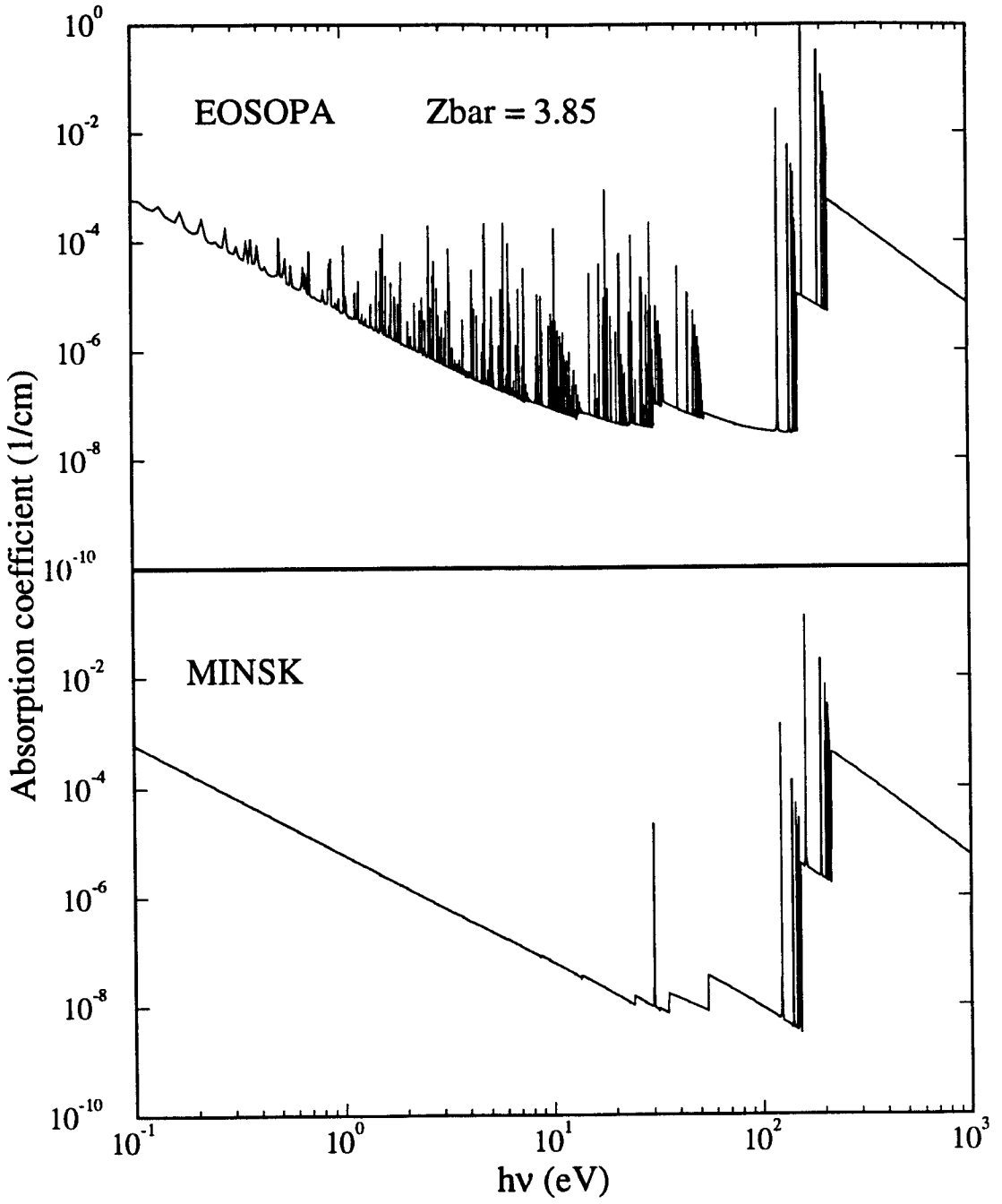

Figure 4.22. Opacity comparison: absorption coefficient of beryllium plasma at $n = 10^{16}$ cm^{-3}, $T = 50$ eV.

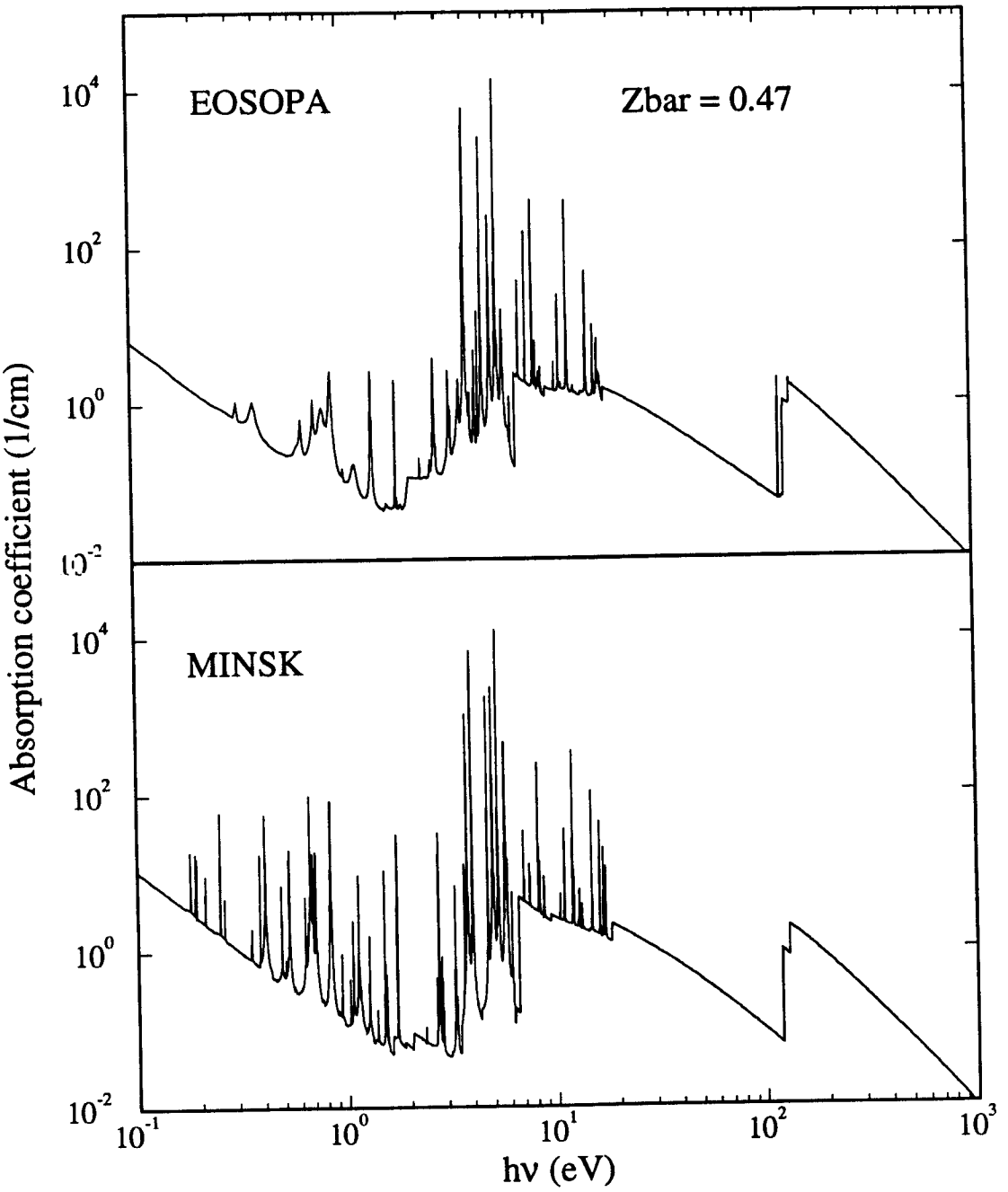

Figure 4.23. Opacity comparison: absorption coefficient of beryllium plasma at $n = 10^{18}$ cm^{-3}, $T = 1$ eV.

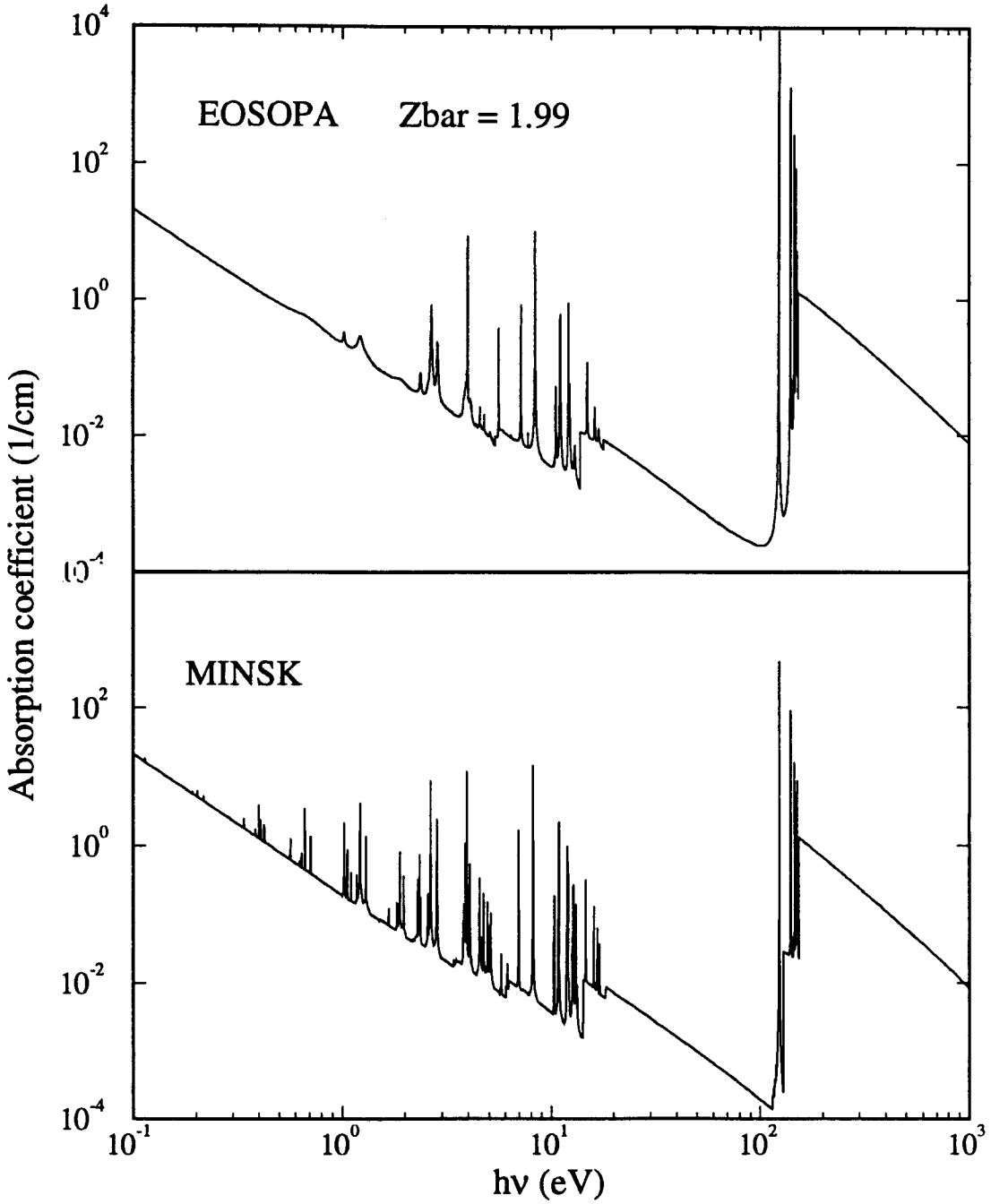

Figure 4.24. Opacity comparison: absorption coefficient of beryllium plasma at $n = 10^{18}$ cm^{-3}, $T = 5$ eV.

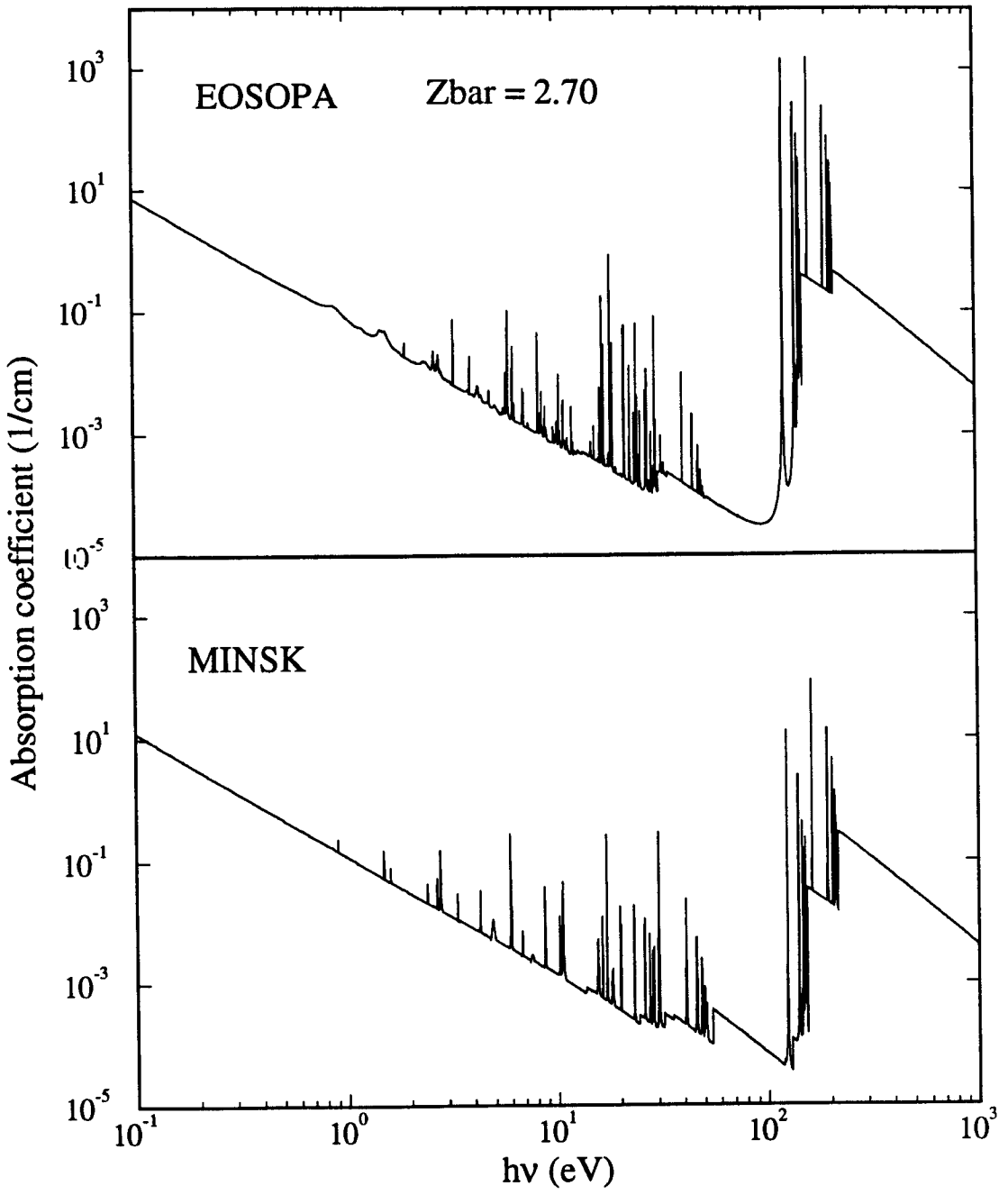

Figure 4.25. Opacity comparison: absorption coefficient of beryllium plasma at $n = 10^{18}$ cm^{-3}, $T = 20$ eV.

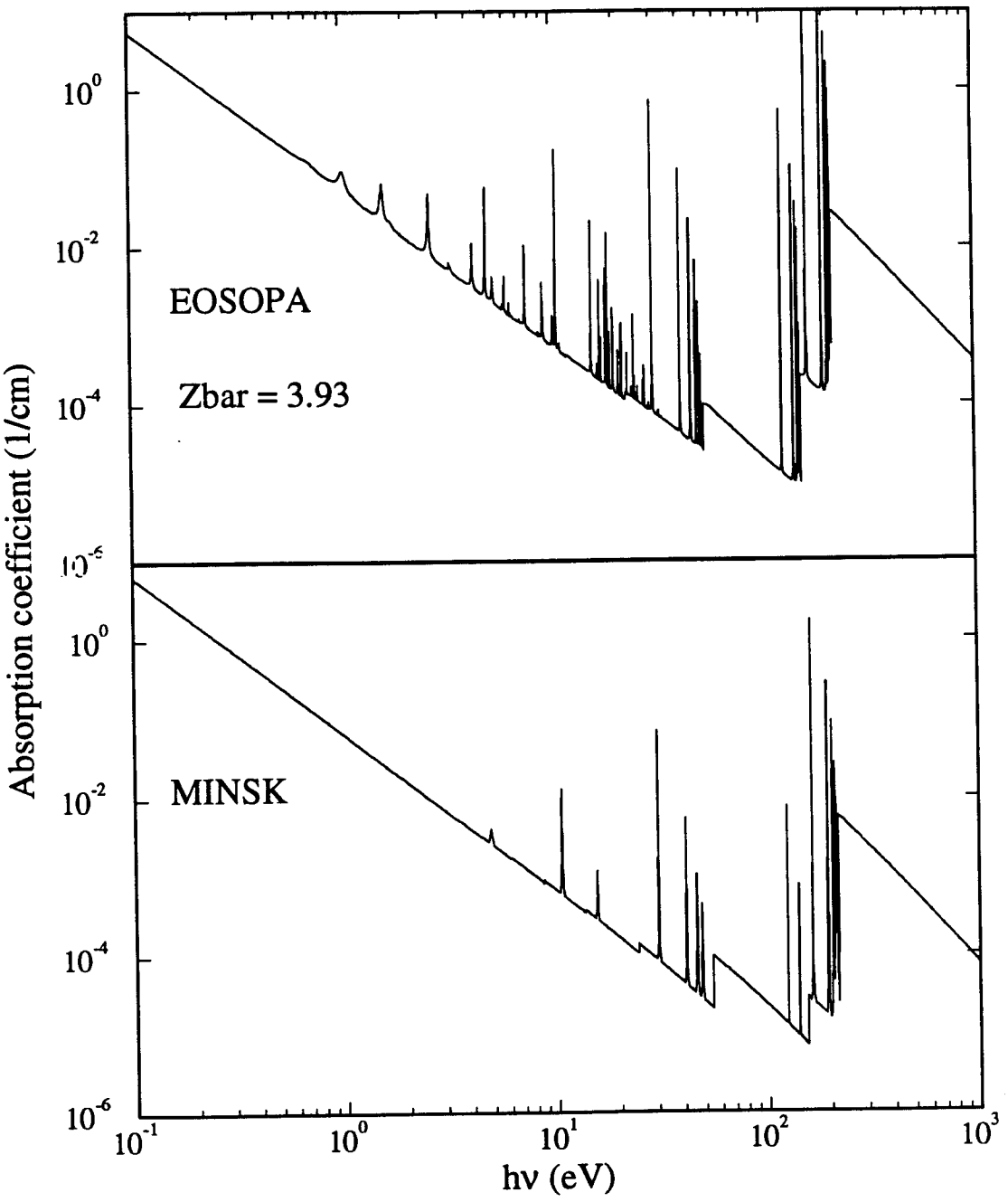

Figure 4.26. Opacity comparison: absorption coefficient of beryllium plasma at $n = 10^{18}$ cm^{-3}, $T = 50$ eV.

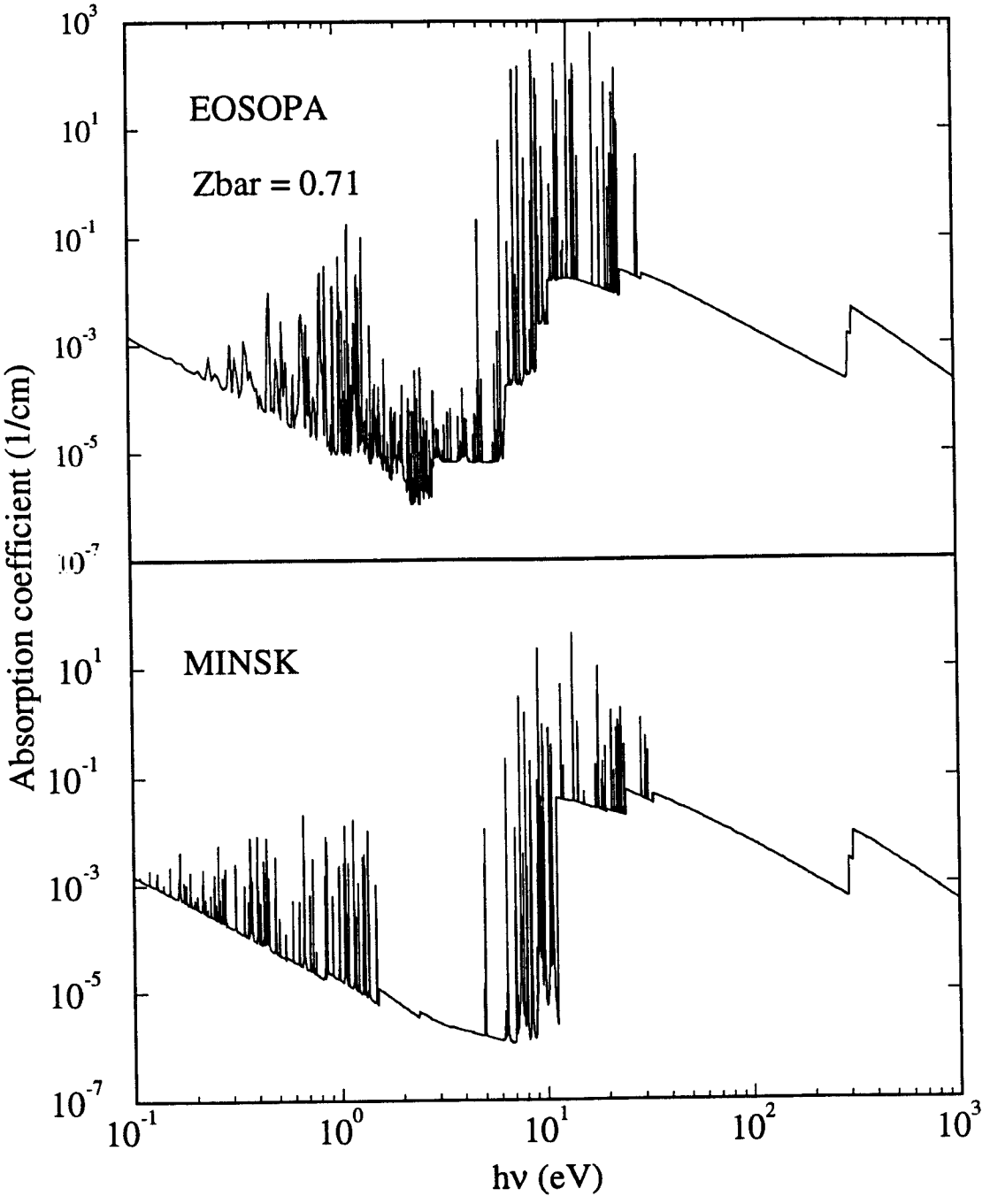

Figure 4.27. Opacity comparison: absorption coefficient of carbon plasma at $n = 10^{16}$ cm^{-3}, $T = 1$ eV.

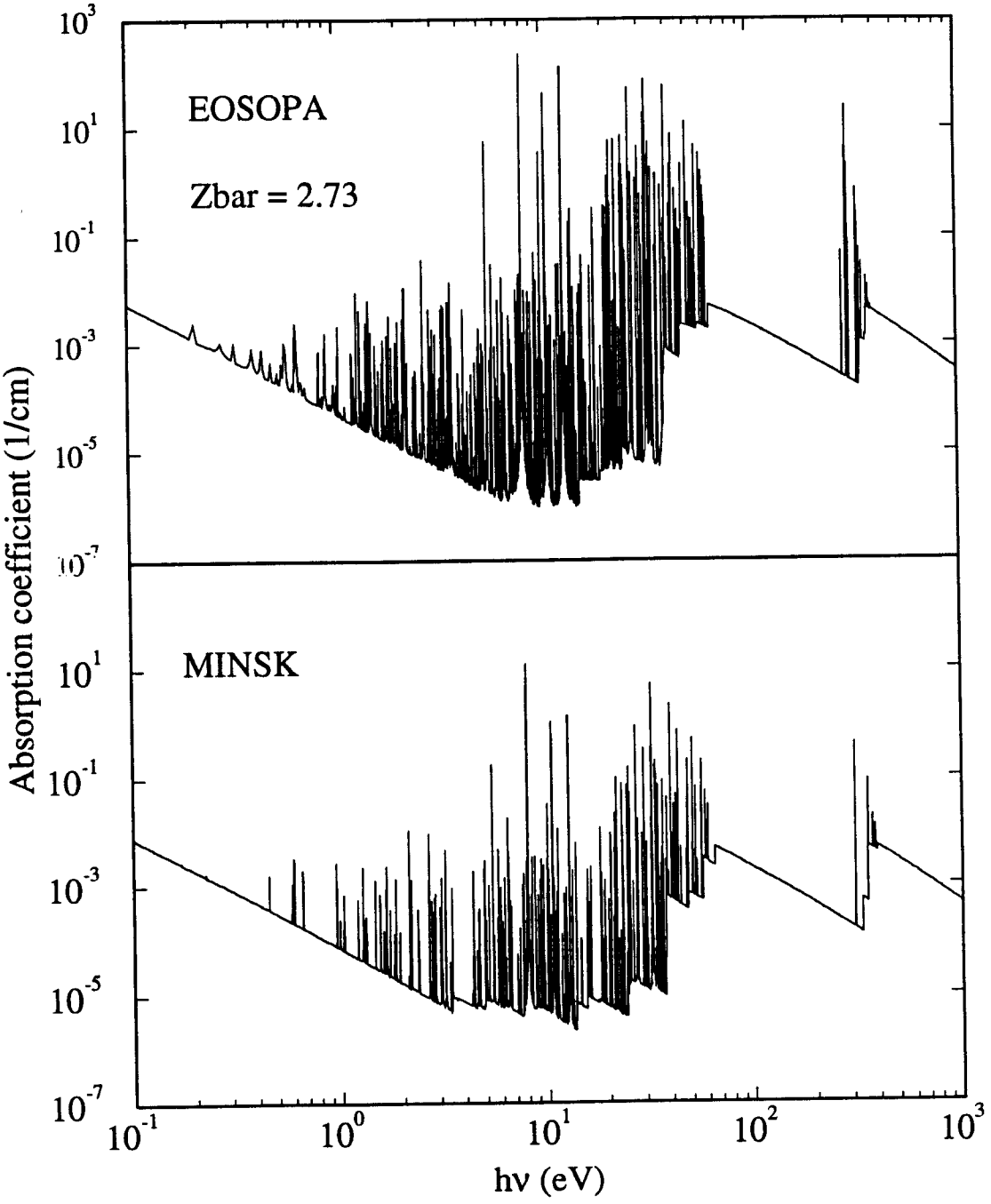

Figure 4.28. Opacity comparison: absorption coefficient of carbon plasma at $n = 10^{16}$ cm^{-3}, $T = 5$ eV.

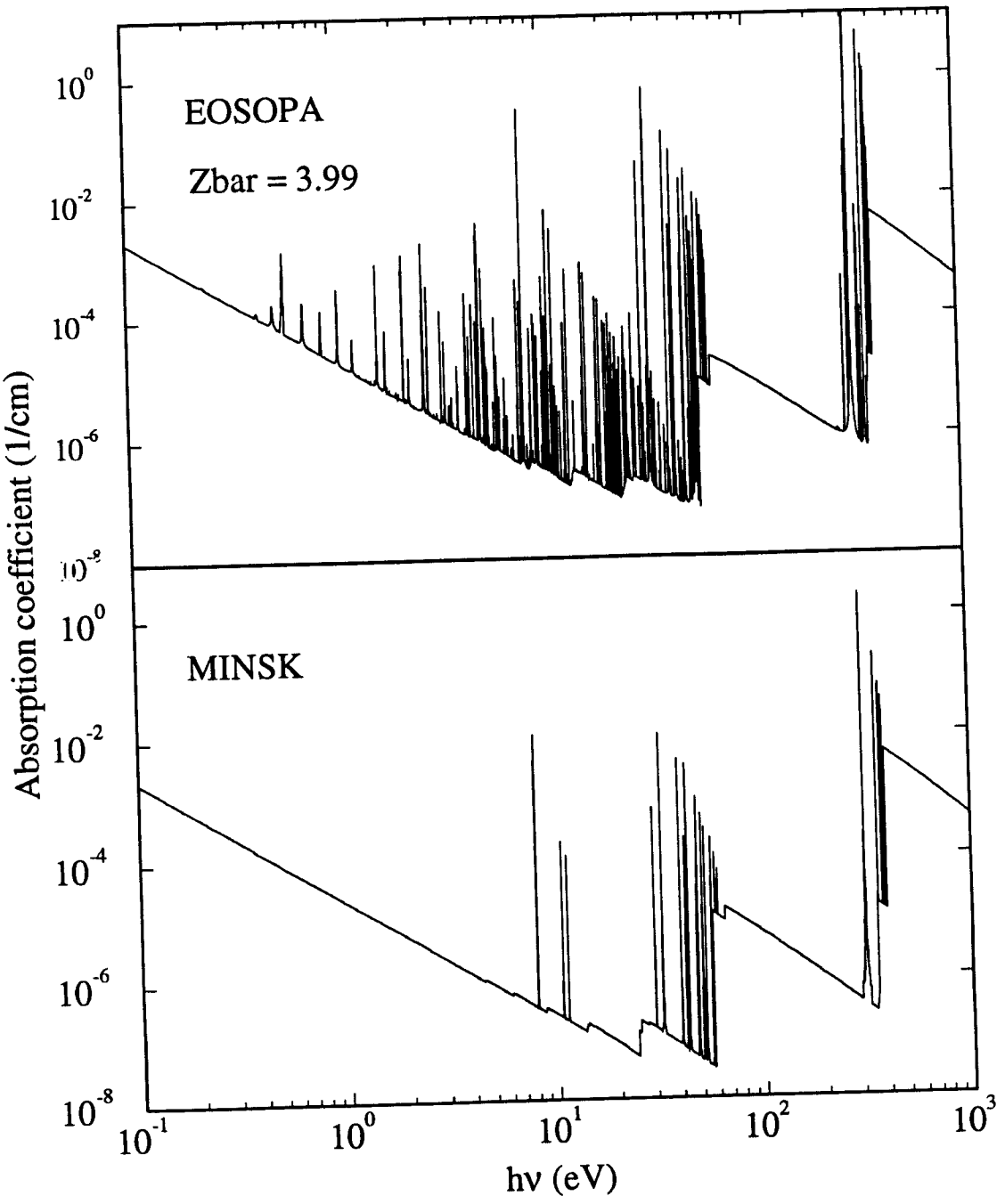

Figure 4.29. Opacity comparison: absorption coefficient of carbon plasma at $n = 10^{16}$ cm^{-3}, $T = 20$ eV.

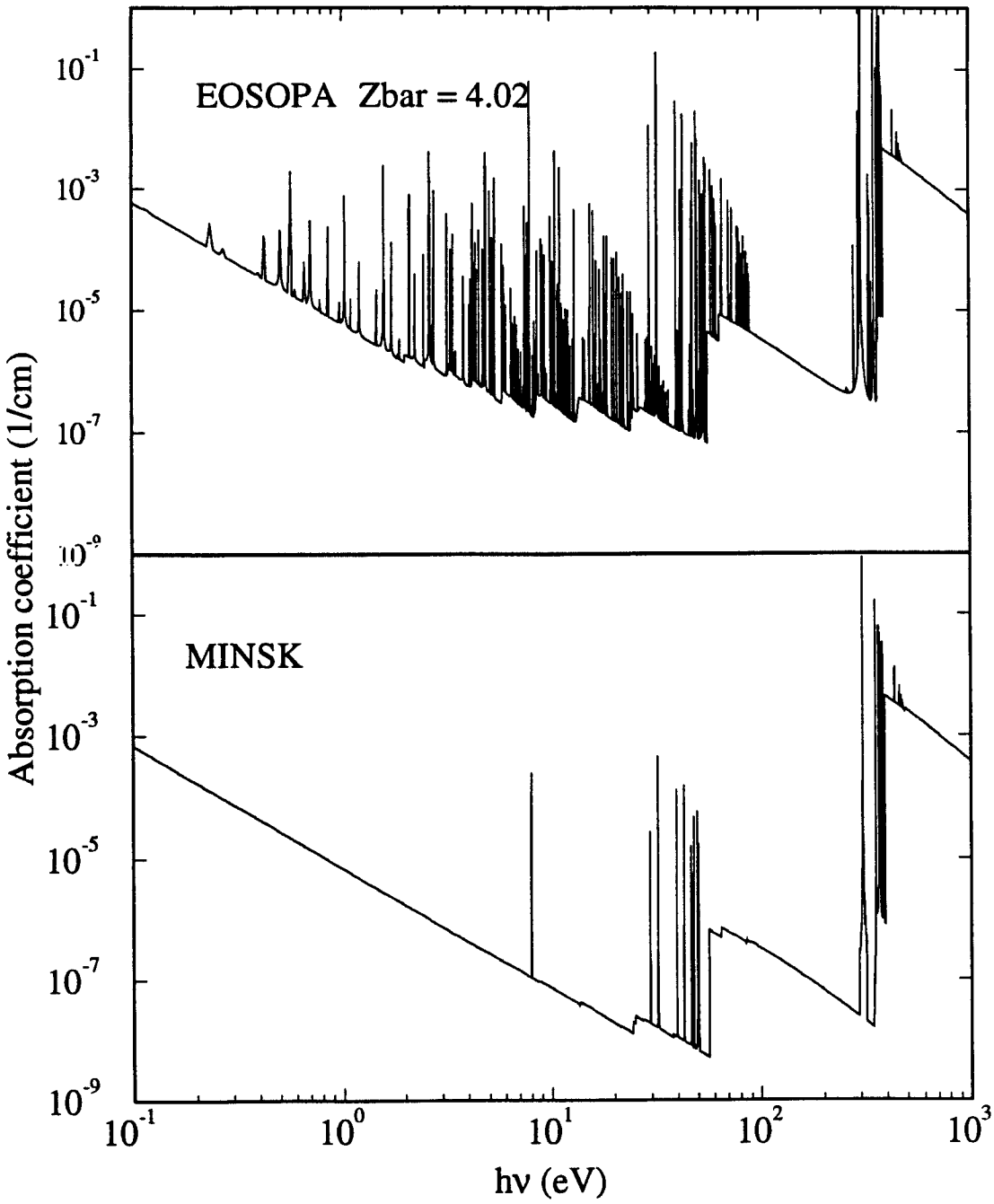

Figure 4.30. Opacity comparison: absorption coefficient of carbon plasma at $n = 10^{16}$ cm^{-3}, $T = 50$ eV.

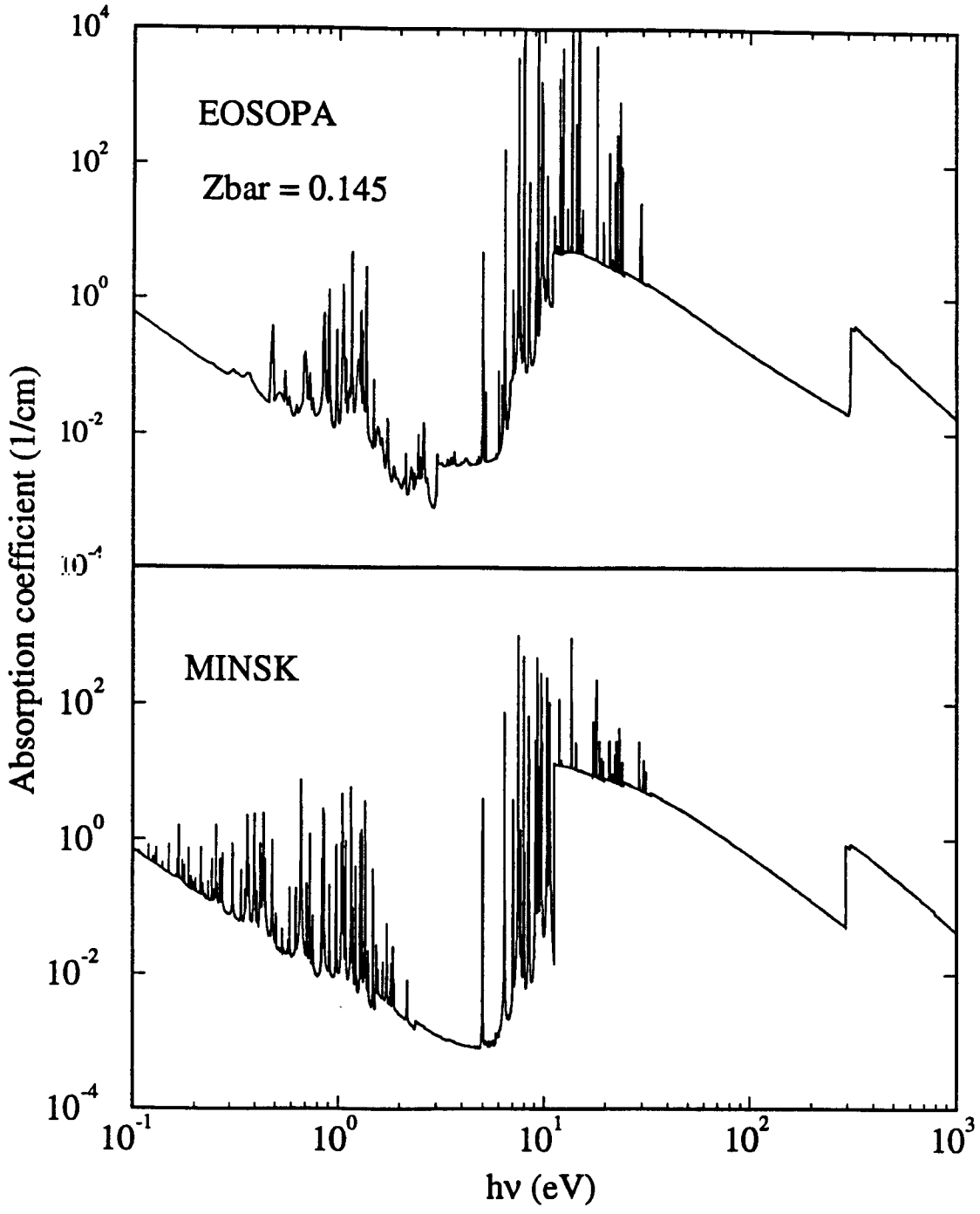

Figure 4.31. Opacity comparison: absorption coefficient of carbon plasma at $n = 10^{18}$ cm^{-3}, $T = 1$ eV.

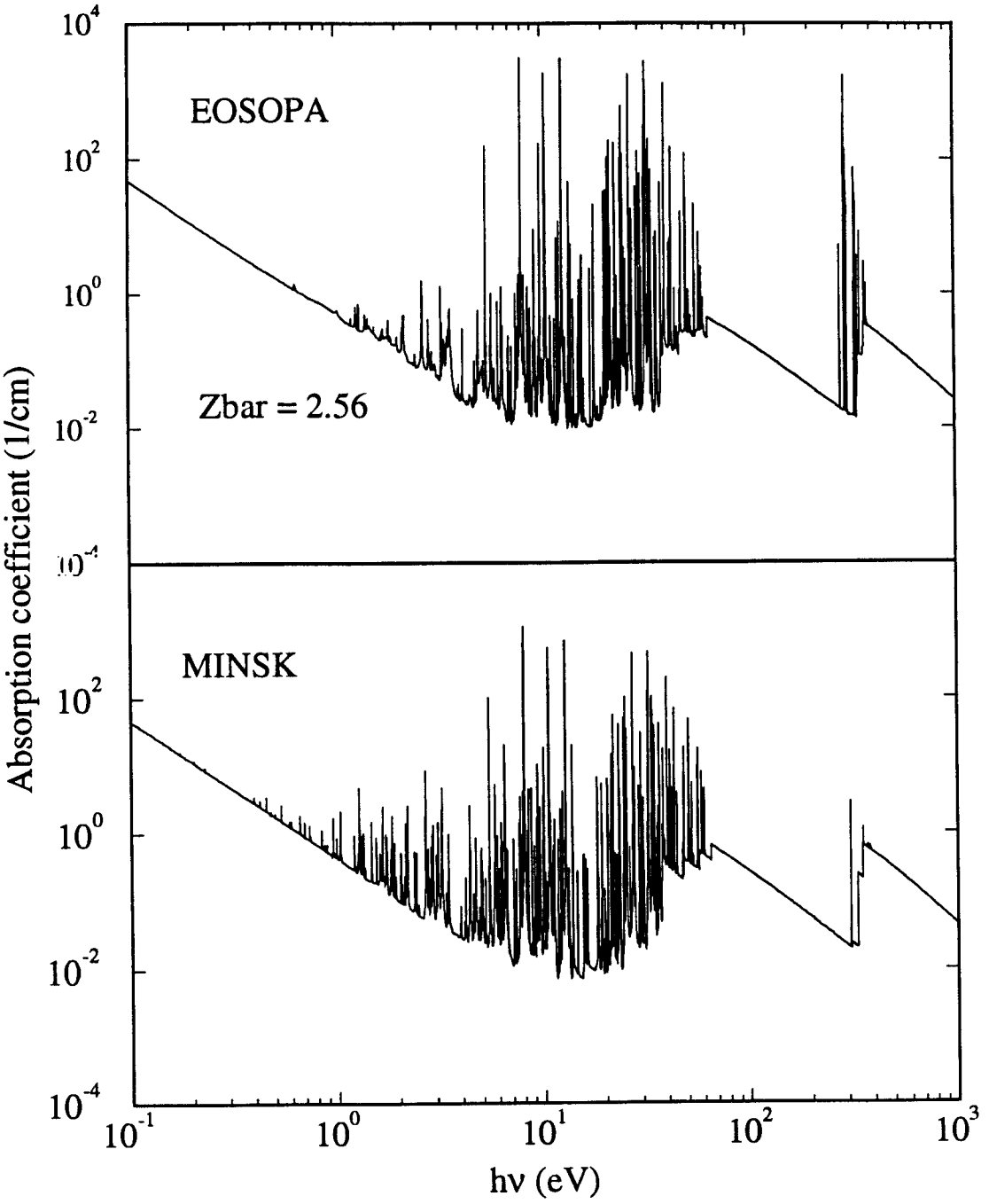

Figure 4.32. Opacity comparison: absorption coefficient of carbon plasma at $n = 10^{18}$ cm^{-3}, $T = 5$ eV.

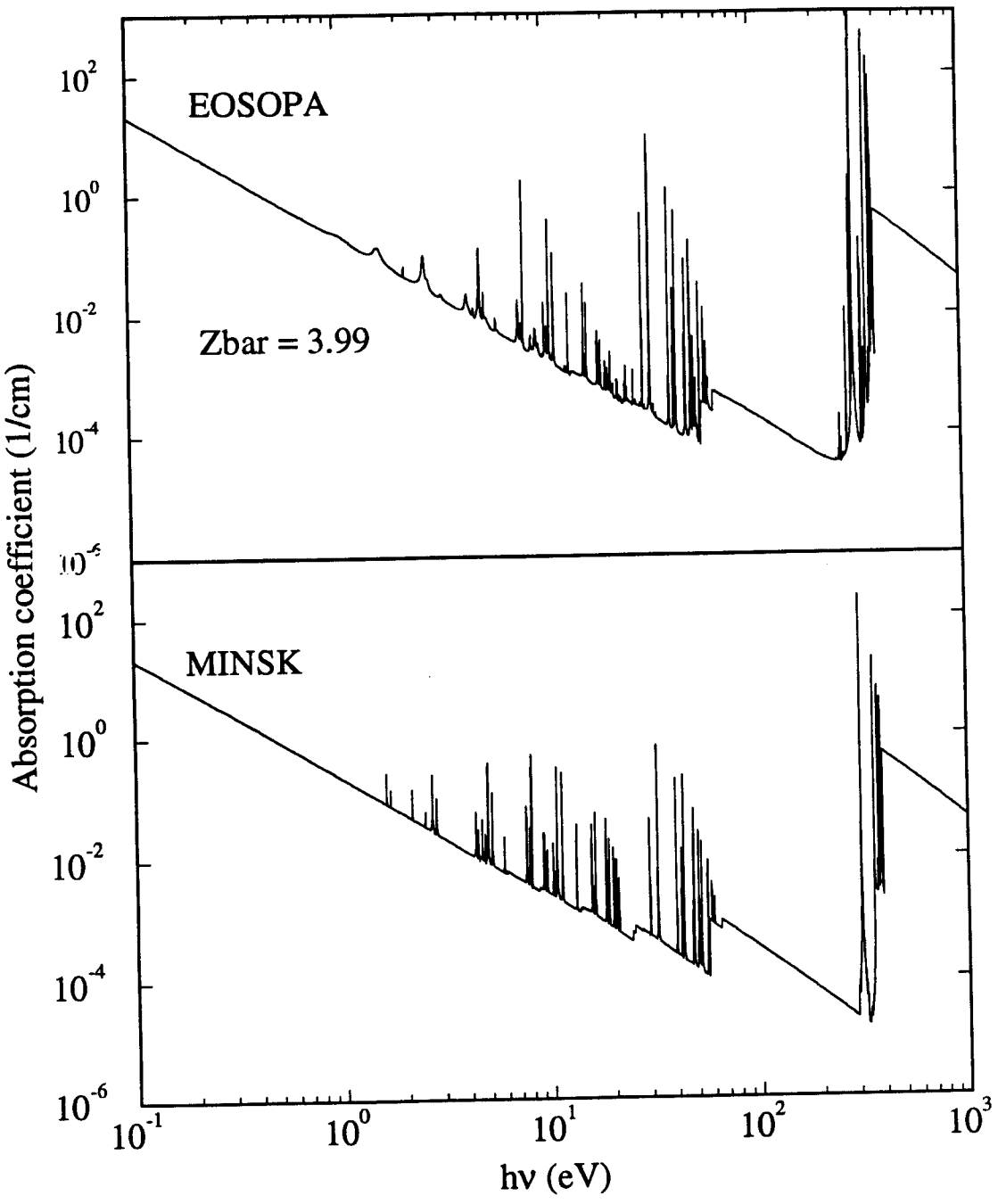

Figure 4.33. Opacity comparison: absorption coefficient of carbon plasma at $n = 10^{18}$ cm^{-3}, $T = 20$ eV.

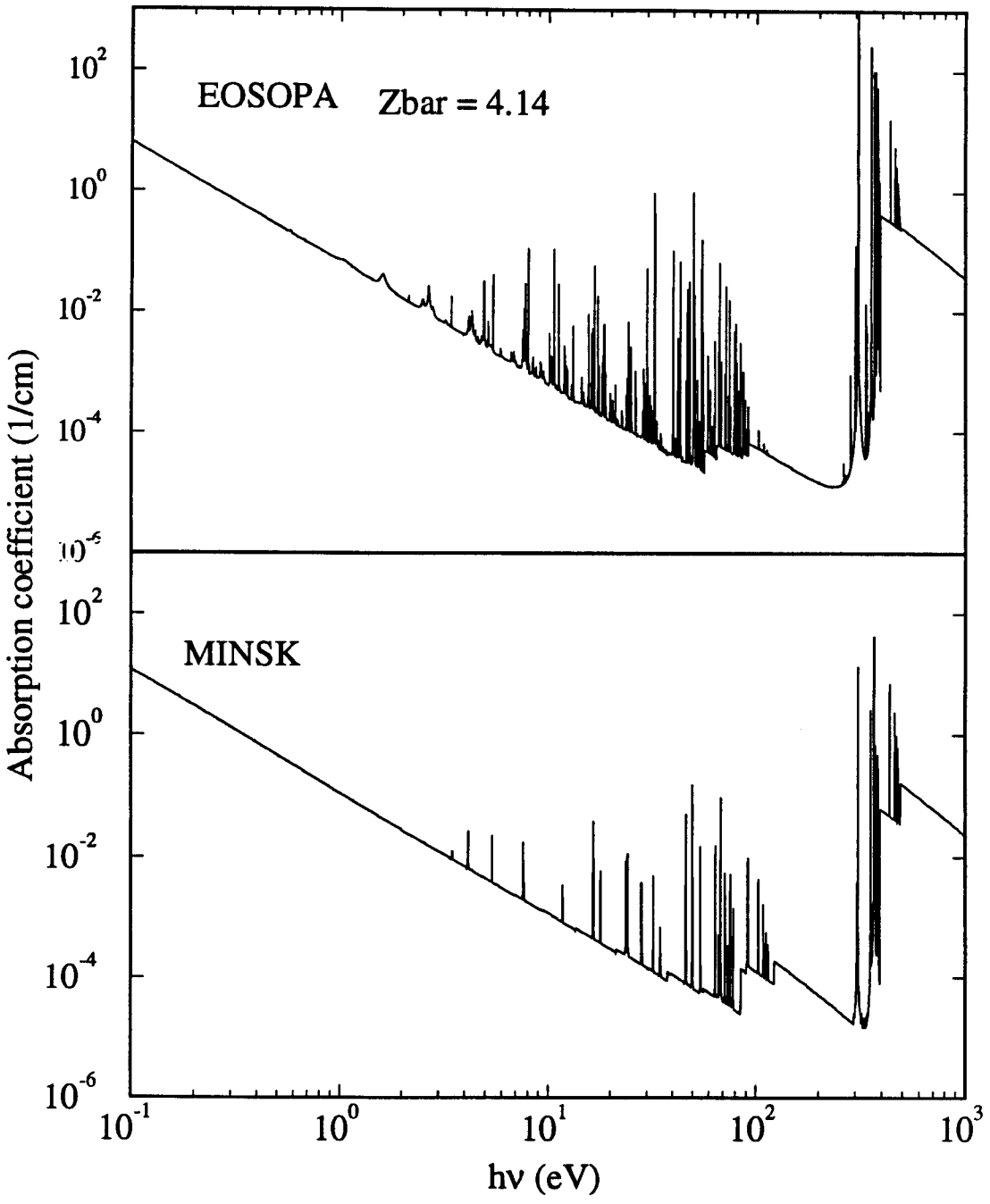

Figure 4.34. Opacity comparison: absorption coefficient of carbon plasma at $n = 10^{18}$ cm^{-3}, $T = 50$ eV.

- differences in continuum lowering models;
- differences in line profile calculations.

It is worth noting that ATBASE, which provides the raw atomic data for EOSOPA, has been used successfully in tests of our spectral analysis calculations. An example of this is shown in Fig. 4.35, where we compare our benchmark calculation of opacity for aluminum plasma against the experimental data of Lawrence Livermore National Laboratory [41]. It can be seen that the calculated line positions and relative intensities agree with experimental data very well. This also indicates that our calculations for equations of state (as reflected through the agreement in ionization balance) should also be reliable.

4.3.2. Opacity Calculations for High-Z Plasmas

For high-Z atomic systems, especially for the ions in electronic configurations with open d or f shells, each configuration contains a very large number of levels. As a consequence, the number of lines corresponding to the bound-bound transitions between these levels are so numerous that it is in practice impossible to do detailed line accounting calculations. On the other hand, these lines are so closely packed that Doppler and/or other broadening effects suffice to merge them together, and the spectra show characteristic "bands" originating from different ionization stages and transitions. This characteristic of high-Z line spectra suggests that unresolved transition array (UTA) model [42] should be a very good approximation for high-Z opacity calculations.

The UTA model describes each transition array as one entity with a statistical distribution of transition energies, rather than as a superposition of many transitions which have to be computed separately. The moments of such a distribution are defined as

$$\mu_n = \frac{\sum_{a,b} E_{ab}^n \, w_{ab}}{W_{AB}} \,, \tag{4.16}$$

where E_{ab} is the transition energy between the state a of configuration A and the state b of the configuration B. w_{ab} is a weight related to the transition probability and $W_{AB} = \sum_{a,b} w_{ab}$. Of special interest are μ_1, the mean energy of transition, and μ_2, or rather $\sigma^2 = \mu_2 - (\mu_1)^2$, the variance of the array, related to the spectral width at half maximum by a simple relationship depending on the shape of the distribution ($\Delta E = 2\sqrt{2}\ln 2\sigma$ or Gaussians). Detailed formulae for the moments μ_n have been given for several types of transition arrays [43]. These formulae consist of sums of angular coefficients multiplied by radial Slater and spin-orbit integrals. These radial integrals may be obtained by Hartree-Fock or central potential models or empirically. In our calculations, we performed

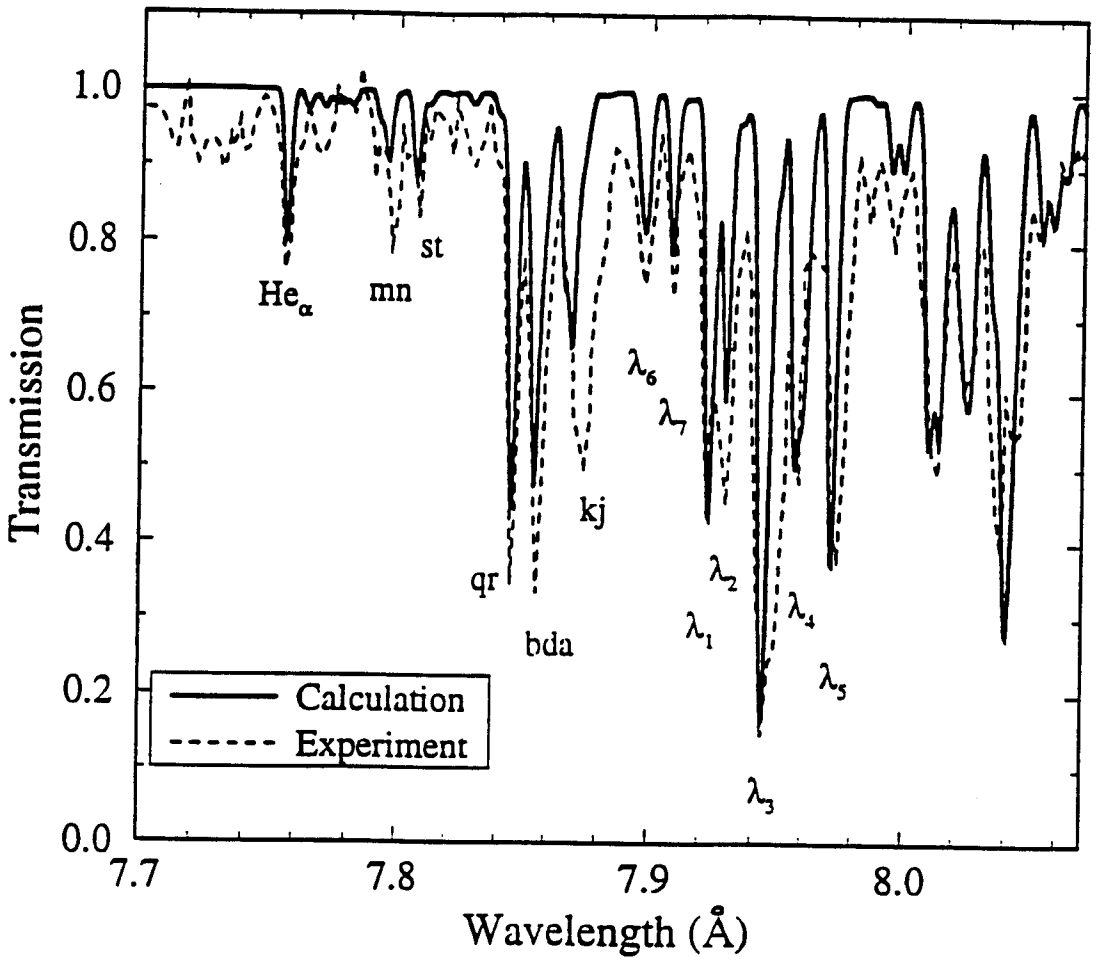

Figure 4.35. Comparison of calculated (solid curve) and experimental (dotted curve) K_α satellite absorption spectra for Al.

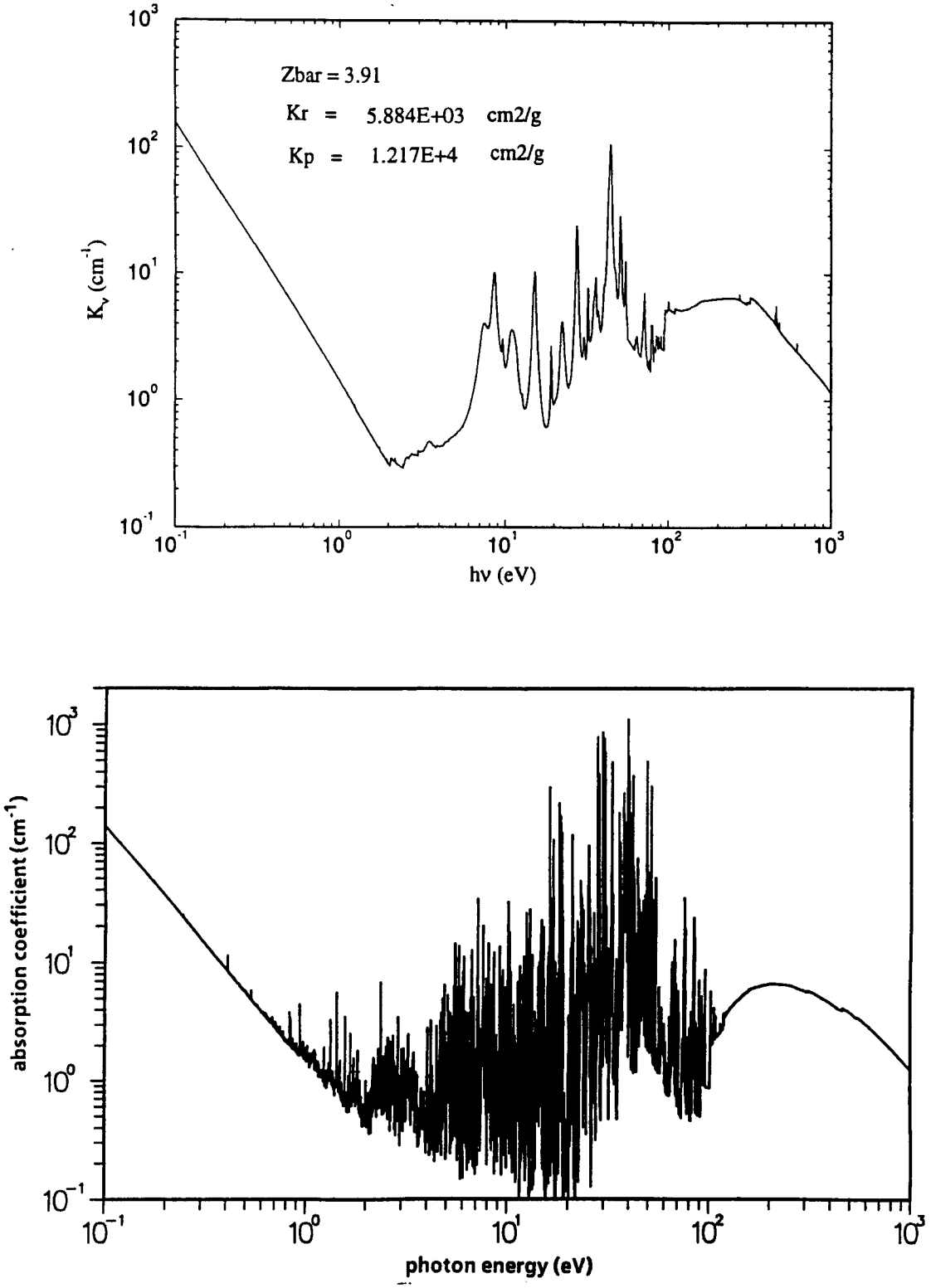

Figure 4.36. Opacity of W plasma at $n = 10^{18}$ cm^{-3}, $T = 5$ eV. The upper plot is the calculated result of EOSOPA with the use of UTA model. The lower plot is MINSK's result.

relativistic Hartree-Fock calculations to determine these radial integrals. Figure 4.36 shows a comparison of our UTA calculation with MINSK's detailed line-by-line calculation for a tungsten (wolfram) plasma. It can be seen that results are qualitatively similar, but there are differences in the detailed structure. It should be mentioned that MINSK's calculation is more elaborate than our UTA calculation in this special case. But this kind of calculation, although successful in low temperature cases, is extremely lengthy and costly, and is impossible to extend to high temperature cases where the ions with open d and f shells become abundant. For tungsten plasmas the contributions from the ions with open d and f shell become significant when $T \gtrsim 10$ eV.

It is very important to calculate the distribution shape of a transition array properly when the UTA model is used for opacity calculations. Figure 4.37 shows a comparison of gold opacities calculated by using UTA model with different line shapes. The result on the left was calculated with normal line shapes including Doppler, natural, and electron impact broadening, while the result on the right is calculated with the inclusion of detailed line distribution moments in each line shape. It is seen that the Rosseland mean opacity is increased by almost a factor of 40 when UTA broadening is included. The UTA result is more accurate and is used in all our high-Z opacity calculations.

We participated in the Third International Opacity Workshop and Code Comparison study [44] in March 1994 and made detailed comparisons with twenty-two opacity codes. Generally speaking, our opacities compare favorably with the results of reputable codes. STA [45] is a highly recognized high-Z opacity code. With the permission of STA's author [46], the comparisons with STA results are shown in Figs. 4.38–4.41. Also shown are the corresponding mean opacities. It can be seen that our calculations of gold opacities are in good agreement with STA in all these cases. This gives us the confidence in our UTA high-Z opacity calculations. It is also worth noting that our high-Z opacities are currently being utilized at both Lawrence Livermore National Laboratory and Wisconsin to simulate Au radiation burnthrough experiments on NOVA [47]. Preliminary results suggest the good agreement with experimental data [48]. Final results of this study will be published elsewhere [49].

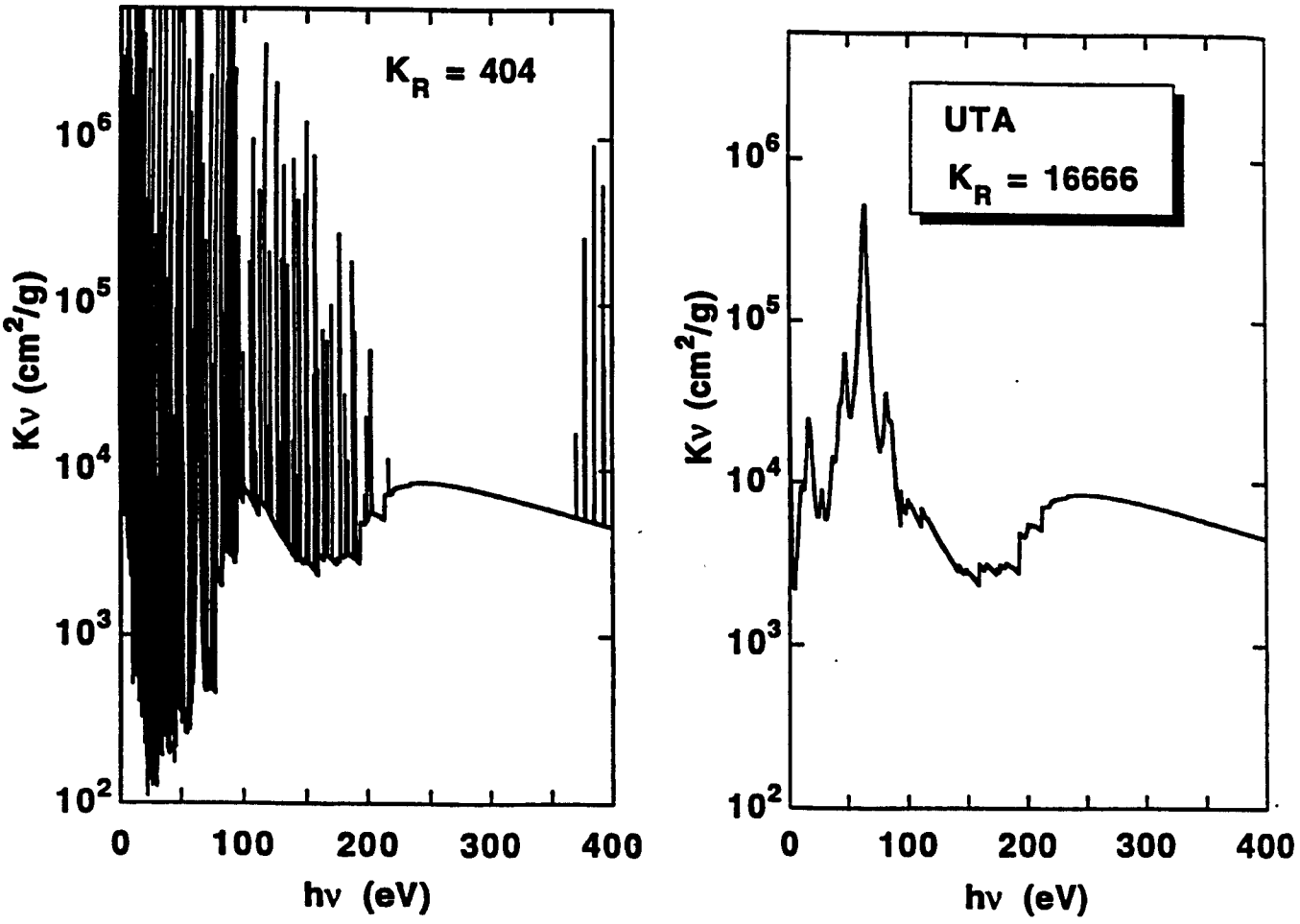

Figure 4.37. Frequency-dependence of Au opacity from calculations neglecting (left) and including (right) broadening due to UTA's.

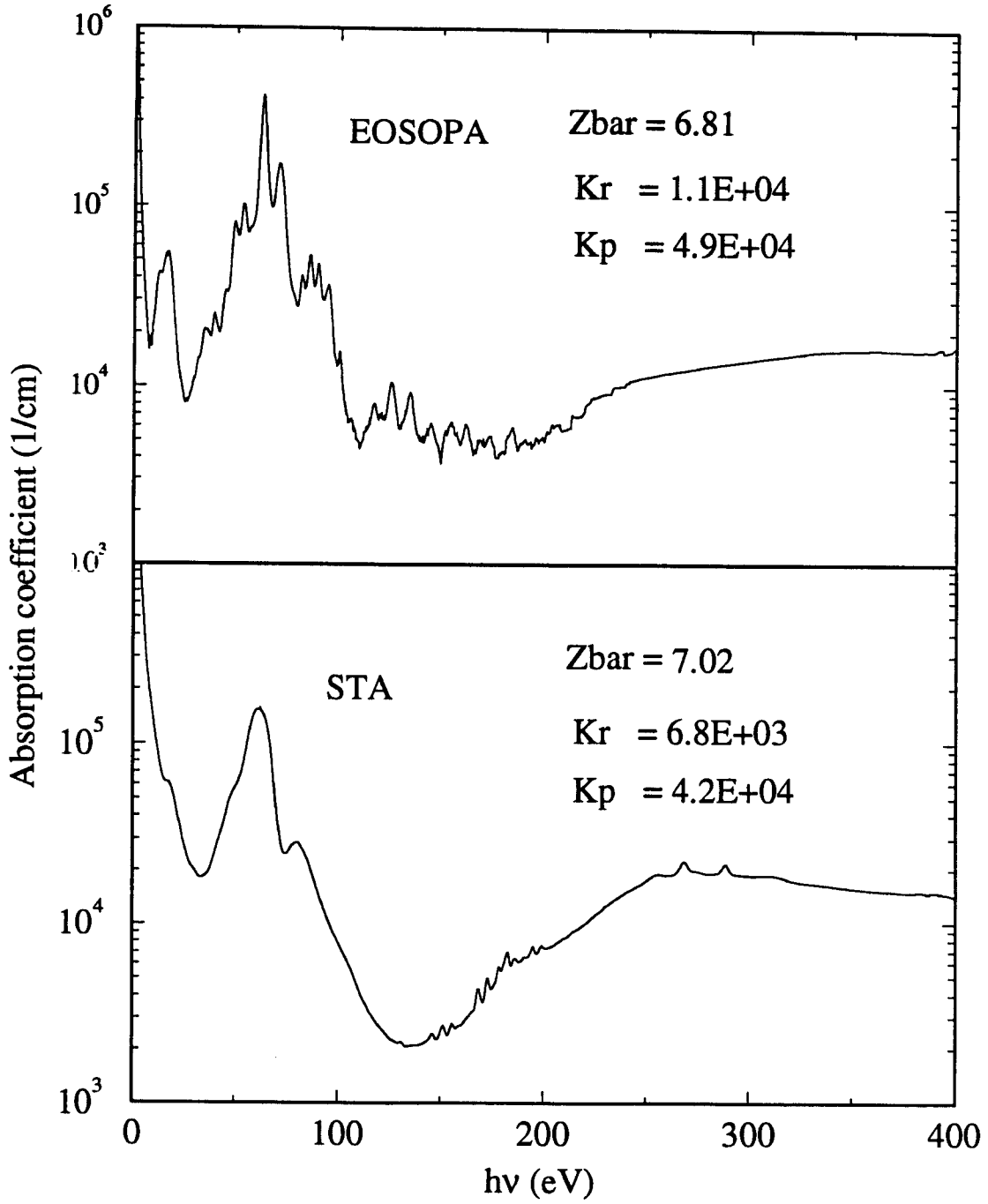

Figure 4.38. Opacity comparison: absorption coefficient for a gold plasma at ρ = 0.1 g/cm^3, T = 20 eV.

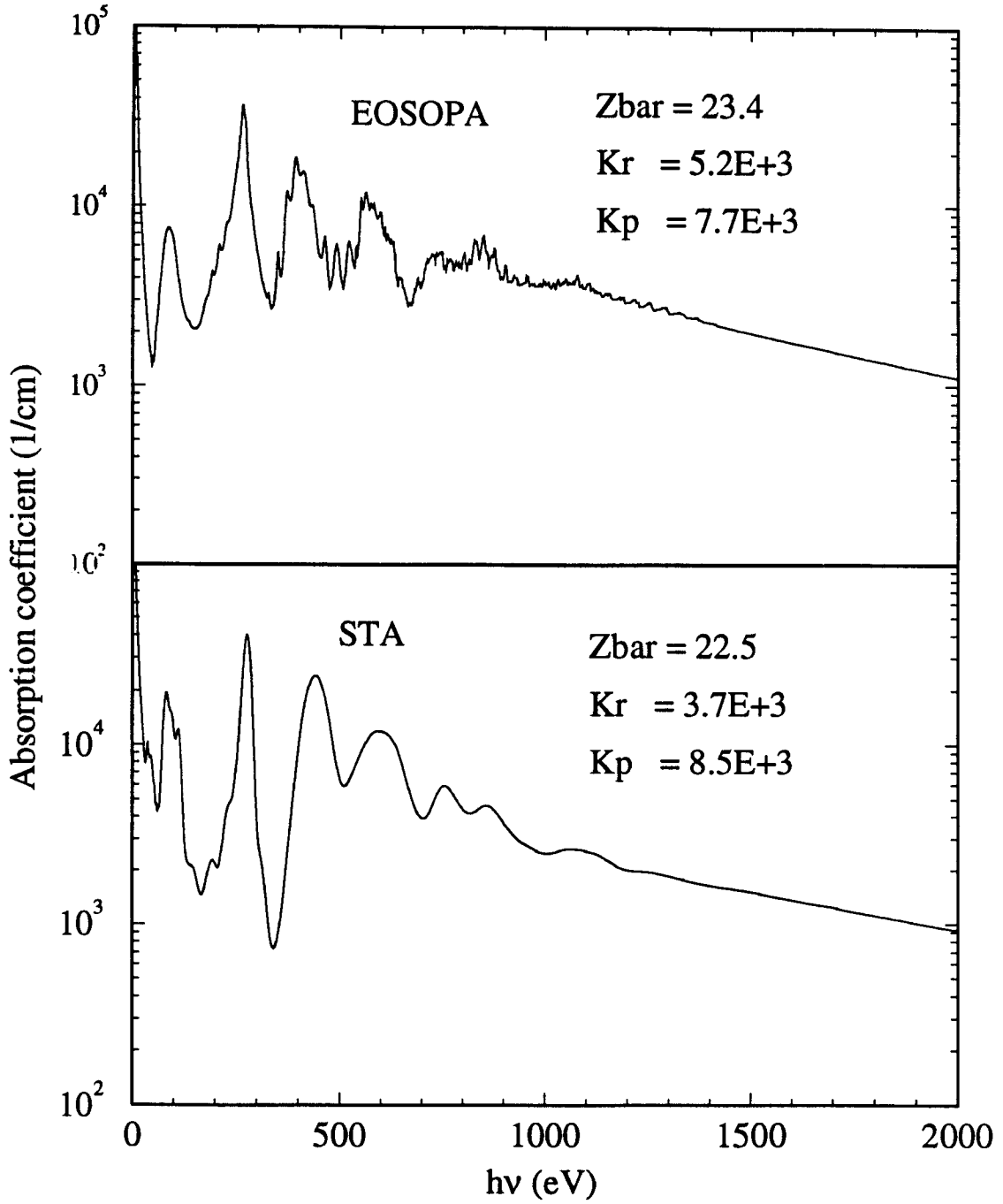

Figure 4.39. Opacity comparison: absorption coefficient for a gold plasma at $\rho = 0.1$ g/cm^3, $T = 100$ eV.

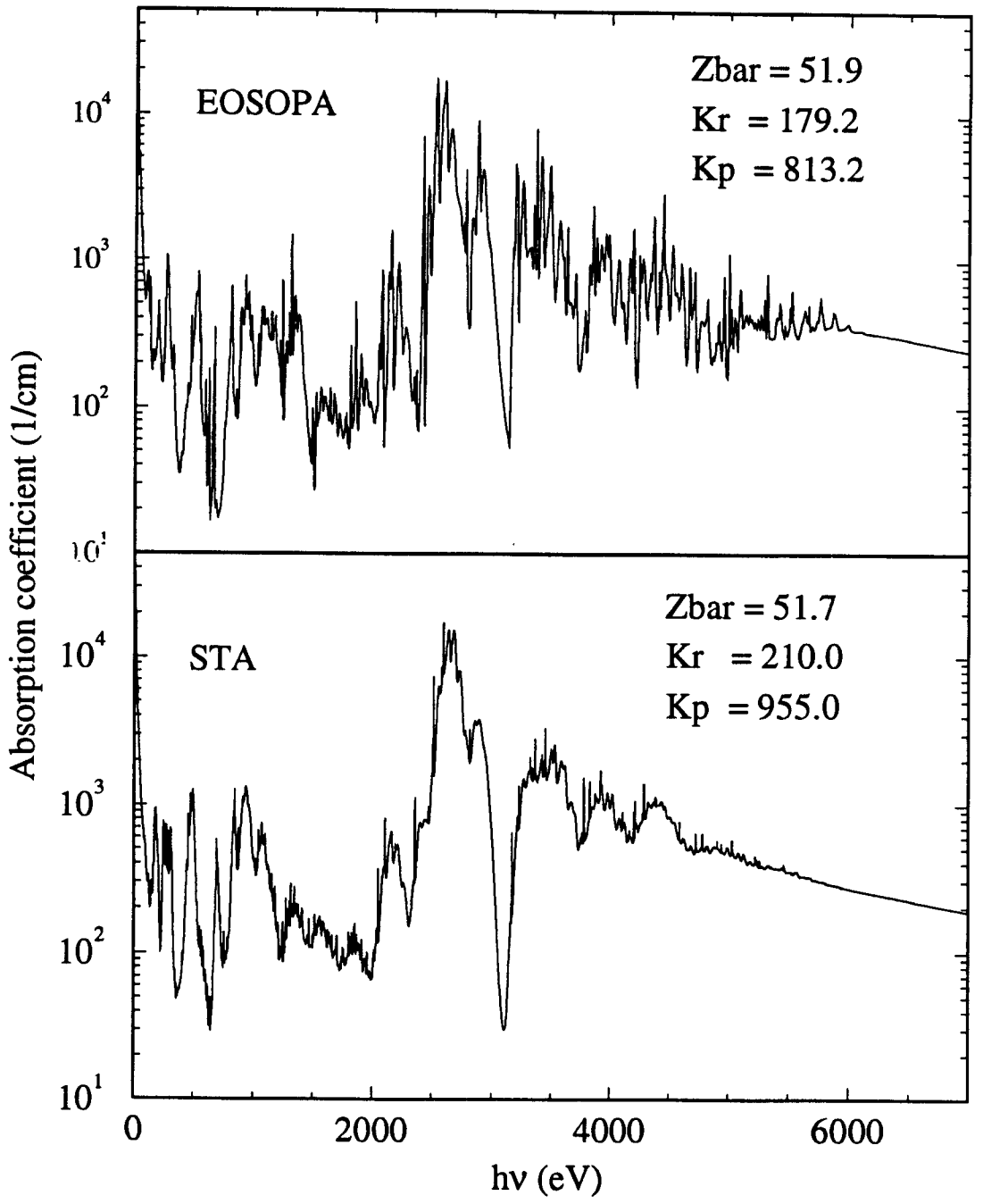

Figure 4.40. Opacity comparison: absorption coefficient for a gold plasma at $\rho = 0.1$ g/cm^3, $T = 500$ eV.

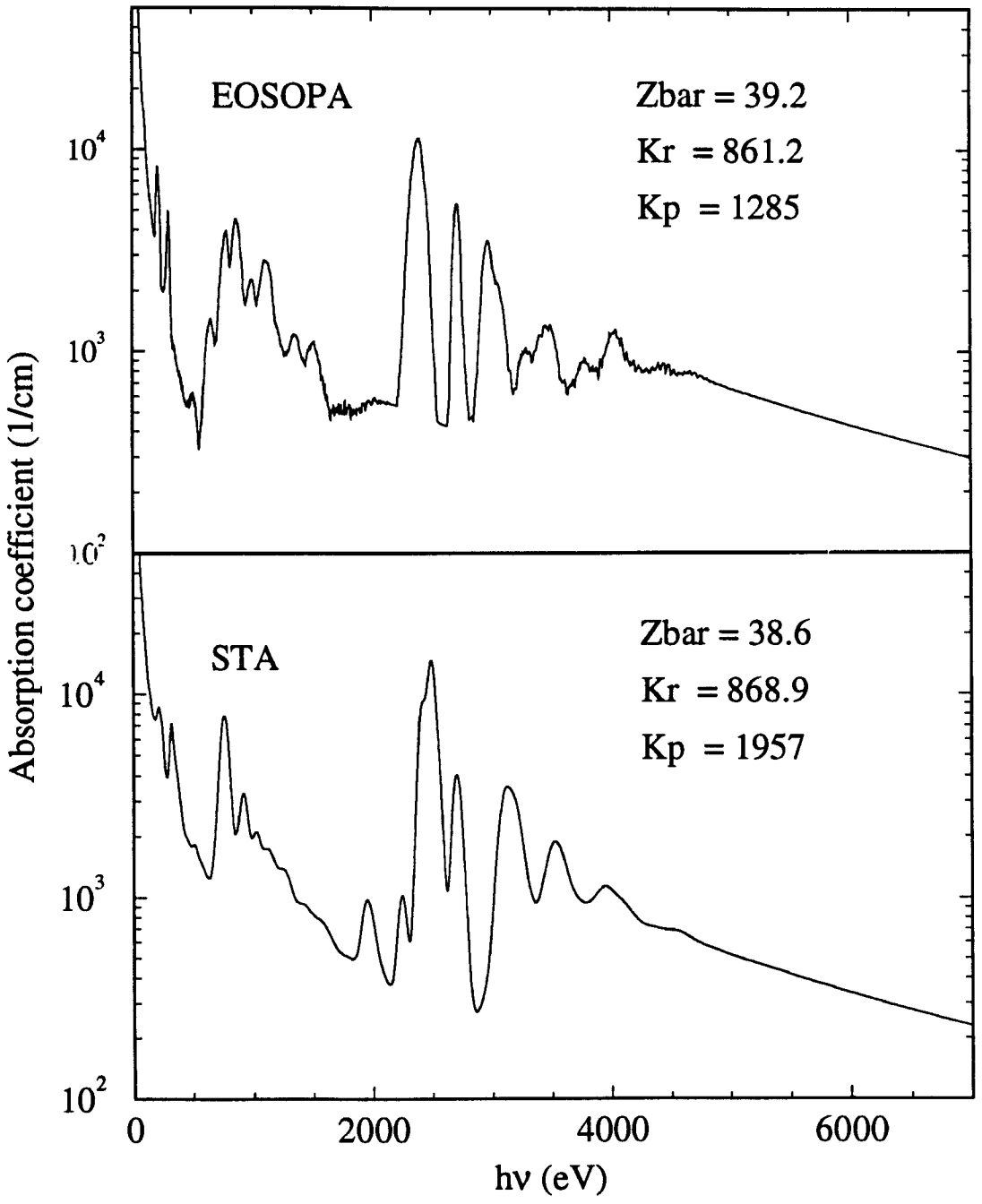

Figure 4.41. Opacity comparison: absorption coefficient for a gold plasma at $\rho = 10$ g/cm^3, $T = 500$ eV

References

1. MacFarlane, J.J., "NLTERT – A Code for Computing the Radiative Properties of Non-LTE Plasma," Fusion Power Associates Report FPA-93-6 (December 1993).
2. Wang, P., "ATBASE User's Guide," Fusion Power Associates Report FPA-93-7 (December 1993).
3. Wang, P., "EOSOPA – A Code for Computing the Equations of State and Opacities of High Temperature Plasmas with Detailed Atomic Models," University of Wisconsin Fusion Technology Institute Report UWFDM-933 (December 1993).
4. MacFarlane, J.J., Moses, G.A., and Peterson, R.R., "BUCKY-1 – A 1-D Radiation-Hydrodynamics Code for Studying Inertial Fusion Plasmas," University of Wisconsin Fusion Technology Institute Report, in preparation (1995).
5. Moses, G.A., Magelssen, G., Israel, R., Spindler, T., and Goel, B., "PHD-IV – A Plasma Hydrodynamics, Thermonuclear Burn, Radiative Transfer Computer Code," University of Wisconsin Fusion Technology Institute Report UWFDM-194 (August 1985).
6. Peterson, R.R., MacFarlane, J.J., and Moses, G.A., "CONRAD – A Combined Hydrodynamics-Condensation/Vaporization Computer Code," University of Wisconsin Fusion Technology Institute Report UWFDM-670 (July 1988); see also Ref. [28].
7. Wang, P., MacFarlane, J.J., and Mehlhorn, T.A., "A Self-Consistent Field Model for Calculating Stopping Powers for Partially Ionized Plasmas," presented at the 10th International Conference on High Power Particle Beams, San Diego, CA (June 1994).
8. Wang, P., MacFarlane, J.J., Moses, G.A., and Mehlhorn, T.A., "Atomic Physics Calculations in Support of Numerical Simulations for High Energy Density Plasmas," presented at the 36th Annual Meeting of the APS Division of Plasma Physics, Minneapolis, MN (November 1994).
9. Wang, P., "BFIT User's Manual," see Appendix A, this report (1995); see also Ref. [16].
10. MacFarlane, J.J., "Collisional-Radiative Equilibrium (CRE) Model for the KATACO Radiation-Hydrodynamics Code," Fusion Power Associates Report FPA-93-9 (December 1993).
11. Goel, B., Höbel, W., and Küfner, K., "The Karlsruhe Target Code System KATACO," to be published.

12. MacFarlane, J.J., Wang, P., and Henderson, D.L., "Theoretical Diagnostic Analyses in Support of KALIF Beam-Plasma Interaction Experiments," Fusion Power Associates Report FPA-92-1.

13. MacFarlane, J.J., Wang, P., Bailey, J.E., Mehlhorn, T.A., Dukart, R.J., and Mancini, R.F., *Phys. Rev.* **E47**, 2748 (1993).

14. Wang, P., MacFarlane, J.J., and Moses, G.A., *Phys. Rev.* **E48**, 3934 (1993).

15. MacFarlane, J.J., Wang, P., Henderson, D.L., and Yasar, O., "Numerical Simulation of High Energy Density Plasmas in Support of KALIF Experiments," Fusion Power Associates Report FPA-93-1 (January 1993).

16. MacFarlane, J.J., and Wang, P., "Plasma Spectral Diagnostic Analyses in Support of KALIF Experiments," Fusion Power Associates Report FPA-94-1 (January 1994).

17. Northcliffe, L.C., and Schilling, R.F., *Nucl. Data Tables* **A7**, 233 (1970).

18. Bailey, J.E., private communication (1994).

19. MacFarlane, J.J., Wang, P., and Moses, G.A., "Non-LTE Radiation Transport in Moderate Density Plasmas," Fusion Power Associates Report FPA-90-2 (January 1990).

20. MacFarlane, J.J., Wang, P., and Henderson, D.L., "Numerical Simulation of Non-LTE Radiative Transfer Effects in Plasmas Created by Intense Proton Beams," Fusion Power Associates Report FPA-91-1 (January 1991).

21. Wang, P., MacFarlane, J.J., and Moses, G.A., "Effects of Multiple Ionization on the K_α Spectrum of Aluminum in Intense Lithium Beam Experiments," *Lasers and Particle Beams*, in press (1995).

22. Boiko, V.A., Faenov, A. Ya, and Pikuz, S.A., *J. Quant. Spectrosc. Radiat. Transfer* **19**, 11 (1978).

23. Brandt, W. and Lapicki, G., *Phys. Rev.* **A23**, 1717 (1981). Lapicki, G. and Zander, A.R., *Phys. Rev.* **A23**, 2072 (1981).

24. Richard, P., Kauffman, R.L., and McGuire, J.H., *Phys. Rev.* **A8**, 1369 (1973).

25. Khan, J.M., Potter, D.L., and Worley, R.D., *Phys. Rev.* **A139**, 1735 (1965). Rutledge, C.H., and Watson, R.L., *Atomic Data and Nuclear Data Tables* **12**, 195 (1973).

26. Fano, U., *Phys. Rev.* **124**, 1866 (1961).

27. Cowan, R.D., "The Theory of Atomic Structure and Spectra," University of California Press, Berkeley (1981).

28. Moses, G.A., Peterson, R.R., and McCarville, T.J., "MF-FIRE — A Multifrequency Radiative Transfer Hydrodynamics Code," *Comput. Phys. Commun.* **36**, 249 (1985).

29. Apruzese, J.P., Davis, J., Duston, D., and Whitney, K.G., *J. Quant. Spectrosc. Radiat. Transfer* **23**, 479 (1980).

30. Apruzese, J.P., J. Quant. Spectrosc. Radiat. Transfer **34**, 447 (1985).

31. MacFarlane, J.J., Peterson, R.R., Wang, P., and Moses, G.A., "Radiation Transport Effects in the Target Chamber Gas of the Laser Fusion Power Reactor SIRIUS-P," *Fusion Technology*, in press (1995).

32. Mehlhorn, T.A., *J. Appl. Phys.* **52**, 6522 (1981).

33. Goel, B., private communication (1994).

34. Mihalas, D., and Hummer, D.G., *Ap. J.* **331**, 794 (1988). *Ap. J.* **331**, 815 (1988).

35. Liberman, D.A., *Phys. Rev.* **B20**, 4981 (1979).

36. "LASL Shock Hugoniot Data," (edited by Marsh, S.P.), University of California Press, Berkeley (1980).

37. "T-4 Handbook of Material Properties Data Bases, Vol. 1c: Equations of State," (edited by K. Holian), Los Alamos National Laboratory Report LA-10160-MS (1984).

38. Loucks, T, "Augmented Plane Wave Method," (W. Benjamin, Inc., New York, 1967).

39. Young, D.A., "A Soft Sphere Model for Liquid Metals," Lawrence Livermore National Laboratory Report UCRL-52352 (1977).

40. van Thiel, M., "Compendium of Shock Wave Data," Lawrence Livermore National Laboratory Report UCRL-50108 (1977).

41. Perry, T.S., Davidson, S. J., Serduke, F.J.D., Bach, D.R., Smith, C.C., Foster, J.M., Doyas, R.J., Ward, R.A., Iglesias, C.A., Rogers, F.J., Abdallah, J., Stewart, R.E., Kilkenny, J.D., and Lee, R.W., *Phys. Rev. Lett.* **67**, 3784 (1991).

42. Bauche-Arnoude, C. Bauche, J., and Klapisch, M., *Adv. At. Mol. Phys.* **23**, 131 (1988).

43. Bauche-Arnoude, C. Bauche, J., and Klapisch, M., *Phys. Rev.* **20**, 2424 (1979), *Phys. Rev.* **25**, 2641 (1982), *Phys. Rev.* **31**, 2248 (1985).

44. Wang, P., and MacFarlane, J.J., Third International Opacity Workshop and Code Comparison Study, MPI Quantenoptik, Garching, March 7-11, 1994.

45. Bar-Shalom, A., Oreg, J., Goldstein, W.H., Sharis, D., and Zigler, A., *Phys. Rev.* **A40**, 3183 (1989),

46. Bar-Shalom, A., private communication, December 1994.

47. Orzechowski, T., private communication, October 1994.

48. Orzechowski, T., et al. (1995) in preparation.

Appendix A. B_FIT User's Manual

A.1 Introduction

Zeeman spectra can be used to measure the magnetic field intensity in high power diode plasmas. The magnetic field can be determined by fitting the observed spectral line profile if the Zeeman splitting dominates over other contributions to the line broadening. In order to have reliable best fitting to the observed data points, it is necessary to calculate the Zeeman splitting emission pattern accurately. This includes the energies of Zeeman splitting levels and component intensities of Zeeman splitting lines.

We have developed a computer code, B_FIT, which can do detailed Zeeman spectrum analysis. In this code, the detailed energy matrix of both magnetic field interaction and spin-orbit interaction is computed and diagonalized to determine the Zeeman energy levels. The important level interaction effects can also be included if necessary. Hence the Zeeman-split emission pattern of a specified line can be calculated accurately for a wide range of magnetic field ($0 < B < \infty$), as opposed to models which are accurate in only the high B-field limit or low B-field limit.

B_FIT has been installed on KfK's computer systems. In this manual we describe the structure of the program and provide a description of how to use the program.

A.2 Defining the Problem

B_FIT can serve for two purposes: (1) checking the sensitivity of a spectral line profile to B-field, (2) diagnosing the B-field strength by fitting the observed line profile data. In both cases, one must first define the problem; i.e., specify the spectral line and its corresponding transition. The line must be isolated and spectrally resolvable. This step can be done by looking up the standard atomic transition wavelength tables. Also needed are the absorption oscillator strength of the transition which can be obtained from published tables or ATBASE calculations.

A.3 Input/Output Descriptions

The B_FIT uses 1 namelist input file, 3 output files, and 1 scratch file. The files are listed in Table A.1, along with their default logical unit number (LUN), names (for Unix systems), types, and a brief description of their contents.

Table A.1. Input/Output Files

Default Unit Number	Default Name (Unix)	Type	Description
1	BFIT.INP	input	namelist input file
2		Scratch	
4	ZEEMAN.LINES	output	(x,y) data file of Zeeman stick spectrum
5	ZEEMAN.SPECTRUM	output	(x,y) data file of Zeeman spectrum fitting with proper line shape
6	BFIT.OUT	output	output data file

A.3.1 Input

All parameters defining a problem are specified in the namelist input file (bfit.inp). Details concerning variable names and definitions are the follows:

(1) Specifying atomic properties of the emitting ion

nz – atomic nuclear charge of the emitting ion.
az – atomic weight of the ion in atomic unit.
iee – number of bound electrons of the emitting ion.
Examples: IEE=13 for Al^{+0}, IEE=4 for C^{+2}, etc.

(2) Specifying properties of the upper atomic level

confg1 – electronic configuration identification of the upper level.
It is a character string of length between 0 to 80 characters. It only serves as 'identification' and does not have any effect on the calculation. Conventionally we input the spectroscopic symbols of outer shells. Example: confg1='2s(1)2p(2)' for the first excited configuration of neutral carbon.

lup – the value of (2*L+1). Here L is the total orbital quantum number of the upper level.

sup – the value of (2*S+1). Here S is the total spin quantum number of the upper level.

njup – number of fine-structure levels included in upper level. In most cases, we only deal with an isolated, well resolvable line. For this kind of line, level mixing effect is not important, only one fine-structure level should be included, i.e., njup=1. In some special cases, level mixing within the same LS term may be important. In these cases, several fine-structure levels within the same LS term should be included. We recommend a general user use njup=1 because it requires some atomic physics experience to understand the concept of level mixing.

jup(i) – the values of $(2 * J_i + 1)$. Here J_i is the total angular momentum quantum numbers of the upper levels.
If njup=1, one should assign only one value here.
Example: for neutral carbon 1s(2)2s(1)2p(2) $^2D_{3/2}$, we have
confg1 = '1s(2)2s(1)2p(2)'
lup = 5 (L=2)
sup = 2 (S=1/2)
njup = 1 (one fine-structure level)
jup(1) = 4 (J=3/2)

iunit – specifying the unit of energy:
iunit=1: Ry
iunit=2: eV
iunit=3: cm^{-1}

eup(i) – atomic energy of the ith upper level in the unit specified by 'iunit'.

(3) Specifying properties of the lower atomic level

confg2 – electronic configuration identification of the lower level. It is a character string of length between 0 to 80 characters. It only serves as 'identification' and does not have any effect on the calculation. Conventionally we input the spectroscopic symbols of outer shells. Example: confg1='2s(1)2p(2)' for the first excited configuration of neutral carbon.

llw – the value of (2*L+1). Here L is the total orbital quantum number of the lower level.

slw – the value of (2*S+1). Here S is the total spin quantum number of the lower level.

njlw – number of fine-structure levels included in lower level. In most cases, we only deal with an isolated, well resolvable line. For this kind of line, level mixing effect is not important, only one fine-structure level should be included, i.e., njup=1. In some special cases, level mixing within the same LS term may be important. In these cases, several fine-structure levels within the same LS term should be included. We recommend a general user use njup=1 because it requires some atomic physics experience to understand the concept of level mixing.

jlw(i) – the values of $(2 * J_i + 1)$. Here J_i is the total angular momentum quantum numbers of the lower levels. If njlw=1, one should assign only one value here.

elw(i) – atomic energy of the ith lower level in the unit specified by 'iunit'.

(4) Specifying the propertities of the transition

nf – total number of J-dependent oscillator strengths included.
This parameter is determined by 'njup' and 'njlw'.
If njup=1 and njlw=1, then nf=1.
jp(i) – the value of (2*J+1) of the ith upper level of the transition.
jl(i) – the value of (2*J+1) of the ith lower level of the transition.
fjj(i) – absorption oscillator strength of the transition.

(5) Specifying plasma temperature and magnetic field flux

tp – plasma temperature in the units of eV
bb – magnetic field flux in the unit of gauss

(6) Specifying the instrumental spectral resolution

fwhmi – FWHM of the instrumental spectral resolution in the units of angstrom.

A.3.2 Output

All the calculation results are written to the formatted file BFIT.OUT. Additional output useful for plotting results are contained in two files, ZEEMAN.LINES and ZEEMAN.SPECTRUM.

ZEEMAN.LINES can be used for showing Zeeman stick spectra for both σ and π transitions. The first set of data is for π transitions, while the second and the third sets of data are for σ transitions. The x column represents the distance of component lines from the line center in the units of angstrom, the y column is the component line strengths in the units of 10^{10} s^{-1}.

ZEEMAN.SPECTRUM can be used for fitting the experimental spectra to determine the applied B-field. The x column is the distance from the line center in the units of angstrom, y-1 column is the calculated spectrum of the π transition, and y-2 column is the calculated spectrum of the σ transition.

A.4 Subroutines

In the following, we list the name of each subroutine in B_FIT along with a brief description of its primary function. A flow diagram showing the relation of the higher level subroutines is shown in Fig. A.1. With the exception of using NAMELIST input, all subroutines are written in FORTRAN 77.

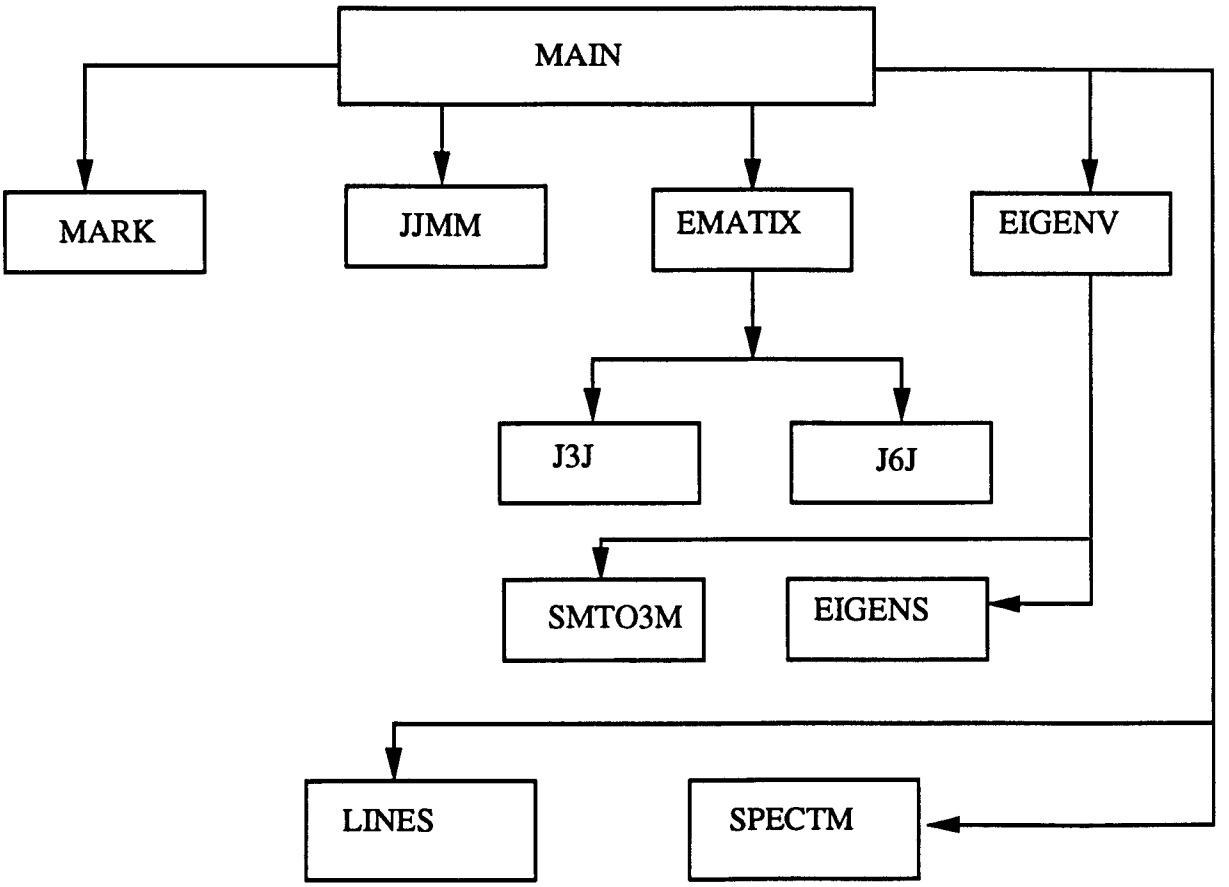

Figure A.1. Flow diagram for selected subroutines of B_FIT.

MAIN	–	Driver routine (main program), reads input.
MARK	–	Shows the title of the calculation
JJMM	–	For a given LS term, this routine evaluates all possible total angular momentum J values and related M values.
EMATIX	–	This routine evaluates magnetic matrix elements and forms a matrix.
EIGENV	–	This routine controls the evaluation of eigenvalues and eigenvectors of the magnetic energy matrix.
LINES	–	This routine computes component line positions and intensities.
SPECTM	–	This routine calculates spectrum by incorporating Gaussian profile for each line.
J3J	–	This routine evaluates 3J-symbol.
J6J	–	This routine evaluates 6J-symbol.
SMTO3M	–	This routine reduces real symmetric matrix to symmetric tridiagonal matrix using an accumulating orthogonal transformation.
EIGENS	–	This routine computes eigenvalues and eigenvectors of symmetric tridiagonal matrix.

A.5 Sample Calculation

As an example, we study the Zeeman spectrum of the GeII $3d^{10}4d^1\ ^2D_{5/2}$ - $3d^{10}4f^1\ ^2F_{5/2,7/2}$ transitions at 24 kG magnetic field. The nuclear charge of Ge is 32, atomic weight is 72, and the total number of bound electrons is 31 for GeII. The electronic configuration of the upper levels is '$3d^{10}4f^1$', the term ^2F means that $L = 3$ and $S = 1/2$. In this sample calculation, we include two fine structure upper levels because of the level interaction effect (in most cases, one can neglect this effect by only using one level): 5/2 and 7/2. The electronic configuration of the lower levels is '$3d^{10}4d^1$', the term ^2D means that $L = 2$ and $S = 1/2$. The value of the total quantum number of the lower level is 5/2. The energy of each level can be obtained from standard atomic energy level tables. It should be noted that we are only concerned with the transition energy between the upper and lower levels, hence the important thing for energy values is that they should have the same reference point. The absorption oscillator strengths for the transitions $3d^{10}4d^1\ ^2D_{5/2}$ - $3d^{10}4f^1\ ^2F_{7/2}$ and $3d^{10}4d^1\ ^2D_{5/2}$ - $3d^{10}4f^1\ ^2F_{5/2}$ are 0.17 and 0.0137, respectively, which are calculated from ATBASE. The plasma temperature is 15 eV, which is used to determine the Doppler profile of the spectrum. The namelist input file of this sample calculation is given in Table A.2. The sample output is given in Table A.3. The schematic form of the computed Zeeman patterns, which is obtained from data file 'zeeman.lines', is shown in Fig. A.2.

Table A.2. Namelist Input for the Sample Calculation.

```
*****************************************************************************
*
*                          NAMELIST INPUT FILE FOR B_FIT
*

&bfitinp

* .... atomic number and atomic weight (in a.u.)
*
        nz = 32,                              ! atomic unclear charge Z
        iee= 31,                              ! number of bound electrons in the system
        az = 72.600,                          ! atomic weight
*
* .... configuration and state's quantum number
*      2L+1, 2S+1, and 2J+1 of the upper levels
*
        confg1 = '3d(10)4f(1)',               ! electronic configuration ID
        lup    = 7,                           ! 2*L+1 of the upper level
        sup    = 2,                           ! 2*S+1 of the upper level
        njup   = 2,                           ! number of J values included for upper level
        jup(1) = 8,6                          ! 2*J1+1, 2*J2+1, ....
        iunit  = 3                            ! unit of the energy:
*                                             ! iunit=1: Ry, iunit=2: eV, iunit=3: cm-1
        eup(1) = 100317,100318                ! atomic energy of the upper level
*
*
* .... configuration and state's quantum number
*      2L+1, 2S+1, and 2J+1 of the lower levels
*
        confg2 = '3d(10)4d(1)',               ! electronic configuration ID
        llw    = 5,                           ! 2*L+1 of the lower level
        slw    = 2,                           ! 2*S+1 of the lower level
        njlw   = 1,                           ! number of J values included for lower level
        jlw(1) = 6,                           ! 2*J1+1, 2*J2+1, ....
        elw(1) = 81013                        ! atomic energy of the lower level

*
* .... absorption oscillator strength
*
        nf  = 2                               ! total number of J-dependent f(ab) included
        jp(1)  = 8,6,                         ! 2*J+1 of the upper state of the transition
        jl(1)  = 6,6,                         ! 2*J+1 of the lower state of the transition
        fjj(1) = 0.17,0.0137                  ! f-values
*
* .... plasma temperaure (in eV)  and magnetic field flux (in gauss)
*
        tp = 15,                              ! plasma temperature in eV
        bb = 24025                            ! magnetic field flux in gauss
*
* .... instrumental spectral resolution (in the unit of angstrom)
*
        fwhmi=0.00                            ! FWHM of instrumental spectral resolution
*
*
 &end
```

Table A.3. Output of the Sample Calculation

```
                ************************************************
                *                                              *
                *           OUTPUTS FROM B_FIT                 *
                *                                              *
                ************************************************

      STUDY THE ZEEMAN EFFECT ON THE FOLLOWING TRANSITIONS:


      atomic system Ge+01
      upper levels:          3d(10)4f(1) 2^P_ 7/2, 5/2,
      lower levels:          3d(10)4d(1) 2^D_ 5/2,

M (2M+1) vector for ( 2L= 6, 2S= 1, 2J= 7 ) :

  8    6    4    2    0   -2   -4   -6    6    4    2    0   -2   -4


M (2M+1) vector for ( 2L= 4, 2S= 1, 2J= 5 ) :

  6    4    2    0   -2   -4


energy matrix for ( 2L= 6, 2S= 1, 2J= 7 ) :

 3.62E+00   .00E+00   .00E+00   .00E+00   .00E+00   .00E+00   .00E+00   .00E+00   .00E+00   .00E+00
  .00E+00  2.48E+00   .00E+00   .00E+00   .00E+00   .00E+00   .00E+00   .00E+00 -3.51E-01   .00E+00
  .00E+00   .00E+00  1.33E+00   .00E+00   .00E+00   .00E+00   .00E+00   .00E+00   .00E+00 -4.53E-01
  .00E+00   .00E+00   .00E+00  1.89E-01   .00E+00   .00E+00   .00E+00   .00E+00   .00E+00   .00E+00
  .00E+00   .00E+00   .00E+00   .00E+00 -9.54E-01   .00E+00   .00E+00   .00E+00   .00E+00   .00E+00
  .00E+00   .00E+00   .00E+00   .00E+00   .00E+00 -2.10E+00   .00E+00   .00E+00   .00E+00   .00E+00
  .00E+00   .00E+00   .00E+00   .00E+00   .00E+00   .00E+00 -3.24E+00   .00E+00   .00E+00   .00E+00
  .00E+00   .00E+00   .00E+00   .00E+00   .00E+00   .00E+00   .00E+00 -4.38E+00   .00E+00   .00E+00
  .00E+00 -3.51E-01   .00E+00   .00E+00   .00E+00   .00E+00   .00E+00   .00E+00  2.65E+00   .00E+00
  .00E+00   .00E+00 -4.53E-01   .00E+00   .00E+00   .00E+00   .00E+00   .00E+00   .00E+00  1.79E+00
  .00E+00   .00E+00   .00E+00 -4.96E-01   .00E+00   .00E+00   .00E+00   .00E+00   .00E+00   .00E+00
  .00E+00   .00E+00   .00E+00   .00E+00 -4.96E-01   .00E+00   .00E+00   .00E+00   .00E+00   .00E+00
  .00E+00   .00E+00   .00E+00   .00E+00   .00E+00 -4.53E-01   .00E+00   .00E+00   .00E+00   .00E+00
  .00E+00   .00E+00   .00E+00   .00E+00   .00E+00   .00E+00 -3.51E-01   .00E+00   .00E+00   .00E+00

  .00E+00   .00E+00   .00E+00   .00E+00
  .00E+00   .00E+00   .00E+00   .00E+00
  .00E+00   .00E+00   .00E+00   .00E+00
-4.96E-01   .00E+00   .00E+00   .00E+00
  .00E+00 -4.96E-01   .00E+00   .00E+00
  .00E+00   .00E+00 -4.53E-01   .00E+00
  .00E+00   .00E+00   .00E+00 -3.51E-01
  .00E+00   .00E+00   .00E+00   .00E+00
  .00E+00   .00E+00   .00E+00   .00E+00
  .00E+00   .00E+00   .00E+00   .00E+00
 9.38E-01   .00E+00   .00E+00   .00E+00
  .00E+00  8.11E-02   .00E+00   .00E+00
  .00E+00   .00E+00 -7.76E-01   .00E+00
  .00E+00   .00E+00   .00E+00 -1.63E+00


energy matrix for ( 2L= 4, 2S= 1, 2J= 5 ) :

 3.00E+00   .00E+00   .00E+00   .00E+00   .00E+00   .00E+00
  .00E+00  1.80E+00   .00E+00   .00E+00   .00E+00   .00E+00
  .00E+00   .00E+00  6.00E-01   .00E+00   .00E+00   .00E+00
  .00E+00   .00E+00   .00E+00 -6.00E-01   .00E+00   .00E+00
  .00E+00   .00E+00   .00E+00   .00E+00 -1.80E+00   .00E+00
  .00E+00   .00E+00   .00E+00   .00E+00   .00E+00 -3.00E+00


eigen energies (in Ry) & vectors for ( 2L= 6, 2S= 1, 2J= 7 ) :

                -4.1E-05 -3.0E-05 -1.9E-05 -2.1E-05 -7.9E-06 -1.2E-05  3.3E-06 -2.3E-06  1.5E-05  6.9E-06
 3.5   4.1E-05     .000     .000     .000     .000     .000     .000     .000     .000     .000     .000
 2.5   2.6E-05     .000     .000     .000     .000     .000     .000     .000     .000     .000     .000
 1.5   1.5E-05     .000     .000     .000     .000     .000     .000     .000     .000     .853     .000
  .5   3.3E-06     .000     .000     .000     .000     .000     .000    -.895     .000     .000    -.446
 -.5  -7.9E-06     .000     .000     .000     .000     .928     .000     .000    -.373     .000     .000
-1.5  -1.9E-05     .000     .000    -.955     .000     .000    -.296     .000     .000     .000     .000
-2.5  -3.0E-05     .000     .979     .000    -.204     .000     .000     .000     .000     .000     .000
-3.5  -4.1E-05    1.000     .000     .000     .000     .000     .000     .000     .000     .000     .000
 2.5   2.5E-05     .000     .000     .000     .000     .000     .000     .000     .000     .000     .000
 1.5   1.6E-05     .000     .000     .000     .000     .000     .000     .000     .000     .522     .000
  .5   6.9E-06     .000     .000     .000     .000     .000     .000    -.446     .000     .000     .895
 -.5  -2.3E-06     .000     .000     .000     .000     .373     .000     .000     .928     .000     .000
-1.5  -1.2E-05     .000     .000    -.296     .000     .000     .955     .000     .000     .000     .000
-2.5  -2.1E-05     .000     .204     .000     .979     .000     .000     .000     .000     .000     .000
```

Table A.3. Output of the Sample Calculation (Continued)

```
                        1.6E-05  2.6E-05  2.5E-05  4.1E-05
  3.5   4.1E-05          .000     .000     .000    1.000
  2.5   2.6E-05          .000    -.788    -.615     .000
  1.5   1.5E-05         -.522     .000     .000     .000
   .5   3.3E-06          .000     .000     .000     .000
  -.5  -7.9E-06          .000     .000     .000     .000
 -1.5  -1.9E-05          .000     .000     .000     .000
 -2.5  -3.0E-05          .000     .000     .000     .000
 -3.5  -4.1E-05          .000     .000     .000     .000
  2.5   2.5E-05          .000    -.615     .788     .000
  1.5   1.6E-05          .853     .000     .000     .000
   .5   6.9E-06          .000     .000     .000     .000
  -.5  -2.3E-06          .000     .000     .000     .000
 -1.5  -1.2E-05          .000     .000     .000     .000
 -2.5  -2.1E-05          .000     .000     .000     .000

 eigen energies (in Ry) & vectors for ( 2L= 4, 2S= 1, 2J= 5 ) :

                       -3.1E-05 -1.8E-05 -6.1E-06  6.1E-06  1.8E-05  3.1E-05
  2.5   3.1E-05          .000     .000     .000     .000     .000    1.000
  1.5   1.8E-05          .000     .000     .000     .000    1.000     .000
   .5   6.1E-06          .000     .000     .000    1.000     .000     .000
  -.5  -6.1E-06          .000     .000    1.000     .000     .000     .000
 -1.5  -1.8E-05          .000    1.000     .000     .000     .000     .000
 -2.5  -3.1E-05         1.000     .000     .000     .000     .000     .000

 **** component line positions center at:   19303.99731 A
 **** component line strength in the unit of 1.0e10 1/s

 !!!! Pi transitions q=M-Mp=0
       -.46765  1.9956E-04
       -.40741  7.9764E-04
       -.30932  1.3469E-03
       -.19149  1.6525E-03
       -.06099  1.5903E-03
        .07851  1.0657E-03
        .34343  9.4928E-04
        .73288  7.9924E-04
       1.08448  4.7398E-04
       1.41633  1.6840E-04
       1.73553  6.5490E-06
       2.04571  8.3177E-05


 !!!! Sigma transitions q=M-Mp=-1
       1.12162  3.1691E-03
        .87882  1.8990E-03
        .93905  1.5719E-03
       1.03714  1.0782E-03
       1.15498  5.9521E-04
       1.28547  2.1475E-04
       1.68989  4.6223E-04
       2.07934  9.3130E-05
       2.43094  2.4808E-06
       2.76280  1.3262E-05
       3.08199  3.3481E-05


 !!!! Sigma transitions q=M-Mp=1
      -1.75387  2.8353E-05
      -1.65578  1.8175E-04
      -1.53795  5.2839E-04
      -1.40746  1.1167E-03
      -1.26796  1.9858E-03
      -1.12162  3.1691E-03
       -.61359  2.1988E-04
       -.26199  4.2673E-04
        .06987  5.5234E-04
        .38906  5.4831E-04
        .69925  3.7544E-04


 **** comparison of different broadening mechanisms
      T(eV),          B(G),          D(zeeman)/D(doppler)
 !!!! Pi transitions q=M-Mp=0
      15.0          24025.0           -1.3816
      15.0          24025.0           -1.2036
      15.0          24025.0            -.9138
      15.0          24025.0            -.5657
      15.0          24025.0            -.1802
      15.0          24025.0             .2319
      15.0          24025.0            1.0146
      15.0          24025.0            2.1650
```

Table A.3. Output of the Sample Calculation (Continued)

```
      15.0          24025.0            3.2037
      15.0          24025.0            4.1839
      15.0          24025.0            5.1268
      15.0          24025.0            6.0430

!!!! Sigma transitions q=M-Mp=-1
      15.0          24025.0            3.3134
      15.0          24025.0            2.5961
      15.0          24025.0            2.7741
      15.0          24025.0            3.0638
      15.0          24025.0            3.4119
      15.0          24025.0            3.7974
      15.0          24025.0            4.9920
      15.0          24025.0            6.1423
      15.0          24025.0            7.1808
      15.0          24025.0            8.1609
      15.0          24025.0            9.1036

!!!! Sigma transitions q=M-Mp=1
      15.0          24025.0           -5.1819
      15.0          24025.0           -4.8921
      15.0          24025.0           -4.5439
      15.0          24025.0           -4.1583
      15.0          24025.0           -3.7461
      15.0          24025.0           -3.3138
      15.0          24025.0           -1.8128
      15.0          24025.0            -.7740
      15.0          24025.0             .2064
      15.0          24025.0            1.1494
      15.0          24025.0            2.0657
```

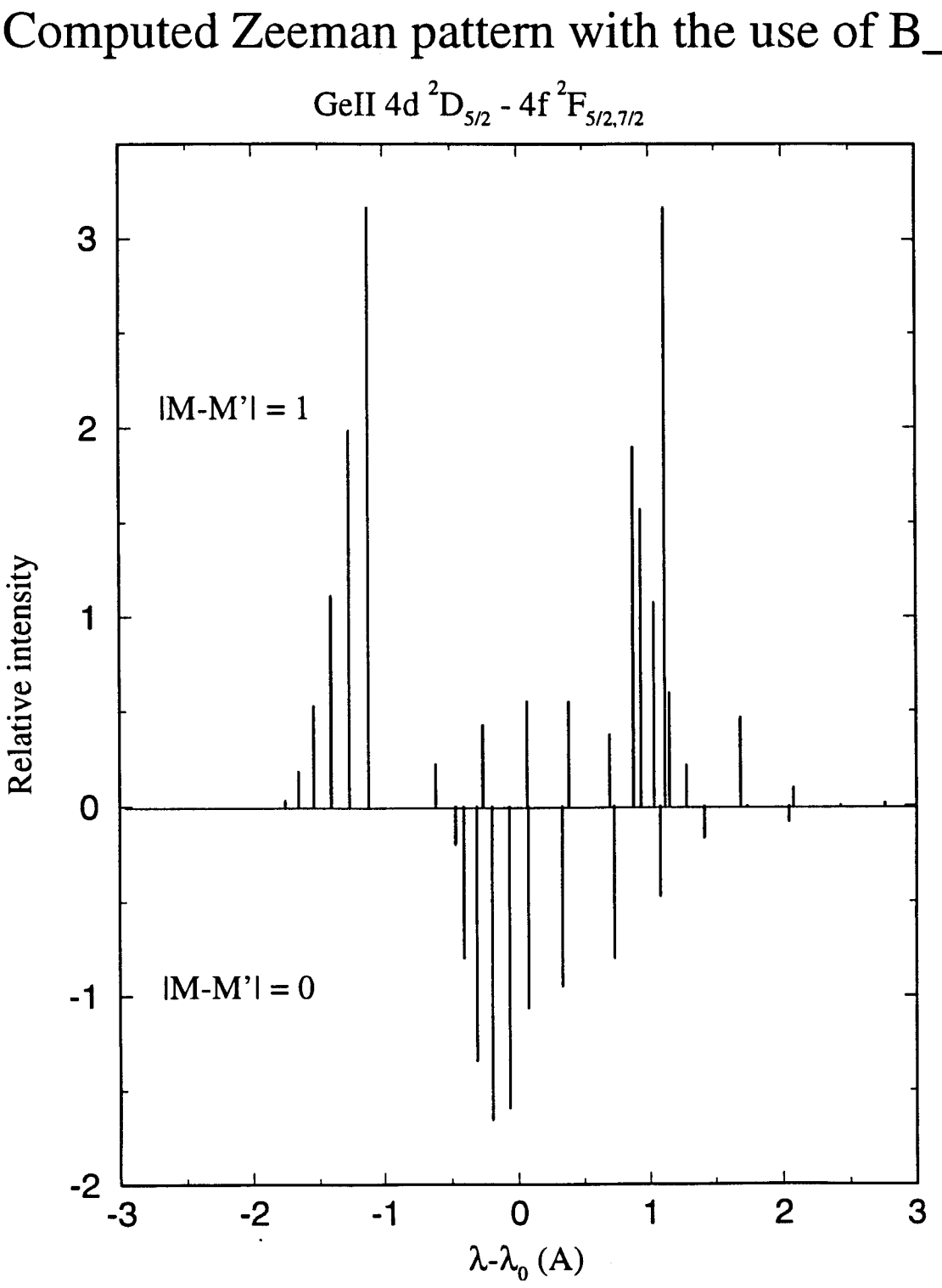

Figure A.2. Zeeman pattern spectrum of the sample problem.